Dissertation zur Erlangung des Doktorgrades

der Fakultät für Chemie und Pharmazie

der Ludwig-Maximilians-Universität München

# Electronic structure variation in the calcium niobate perovskite:

# A comparison between bulk and nanosheets

von

Kulpreet Singh Virdi

aus

Jalandhar, Indien

2012

## Erklärung

Diese Dissertation wurde im Sinne von § 7 der Promotionsordnung vom 28. November 2011 von Frau Prof. Dr. Christina Scheu von der Fakultät für Chemie und Pharmazie betreut.

## Eidesstattliche Versicherung

Diese Dissertation wurde eigenständig und ohne unerlaubte Hilfe erarbeitet.

München, den 17. Dezember 2012.

(Unterschrift des Autors)

Dissertation eingereicht am 20. Dezember 2012.

1. Gutachterin: Prof. Dr. Christina Scheu

2. Gutachterin: Prof. Dr. Bettina Valeska Lotsch

Mündliche Prüfung am 29. Januar 2013.

*This work is dedicated to three teachers of mine*

*Ashwini Goel for teaching that it does not matter what others think, you follow your own path,*

*Ramesh Kumar Bhanot for teaching that you follow the right path even if the world doesn't,*

*Arvind Chauhan for teaching that it is more important to know yourself than knowing the world.*

# Acknowledgements

It would be stupid to say this work would have seen the light of day had my mother not single handedly, through her devotion, turned my foundering schooling around. *Ma* I owe all that I am today to you, for being there for me, for showing me the right path despite the countless obstacles.

It takes quite a lot of empathy to think about your students. One doesn't often come across a boss who is worried about the fact that the students might get back ache working long hours on uncomfortable chairs. I am glad to have spent three years working for one. Thanks a lot Tina for being such a great boss. Questioning oneself is a central tenet of scientific thought. I thank you for teaching the importance of it to me.

In a profession ensnared in grant moneys and impact factors, it is a pleasure to have worked with three scientists whose sole motive is learning. Prof. Blaha I am deeply indebted to you for the support you offered and the guidance you provided. Your inquisitiveness for knowledge marvels me and shows me the way to go.

Operating the electron microscope is an art. It requires insight, knowledge, imagination and patience. I am glad to have worked closely with you Yaron. I do not think I will come across a better artist. Thanks a lot for all you taught me about the microscope.

The motivations of graduate students are supposedly thought to be a degree, a job and money to name a few. Not often do you come across a person who knows that the student also wants to learn, to do things with his/her own hands, and for that he/she needs support. Wayne, I am thankful to you for all the support you gave me. You run the group in such a marvelous way. To conclude, let me say I am so glad to have learnt from you that the desire to learn does not fade away with years if science is what you love.

My study would never have been possible and I would have been writing my dissertation on the other side of the Atlantic had it not been for the effort of Marilena. Marilena, thanks a lot for helping me out at such an important juncture of my life. Thanks also to Marie and Prof.

lot for being the best *Bhai* ever. Thanks to Ramona and Jonathan for being so nice and caring. Special thanks to the members of Bein and Wagner groups. You guys have been awesome.

Priyank, thank you for being such an understanding friend for more than a decade. I do not think your words of wisdom are replaceable. Akshay, I owe a lot of character I possess to you. I would not have had the guts to follow my path had you not become my friend. Thanks a lot for being a mountain of support. Ranjit, thank a lot for taking up my duties when I left for study, I might have quit studies if it wasn't for your support. I am glad you were always there to give me the encouragement I needed. Mehtab, you are a lot bigger influence on me than you might know. I am thankful to you for all the wonderful times we had. Mayank, I thought ten years ago that you jabbered non-stop. I think today that you jabber non-stop. I do not know why, but it is great to have you jabber. Thanks for being such a great friend. Aman, I thank you for being the steadying influence on me. I can look back to more than two decades of joys shared with an immense satisfaction whether it was playing cricket in school or discussing philosophy late in the evenings. I thank my brothers Vicky and Nanu for being there for me. I do not look back at anything with more fondness than going to the river with you. Prineet, thanks a lot for being the shining star in my life for more than two decades. It is priceless to have a friend for life you can talk about everything from existentialism to Bob Dylan.

# Contents

# List of Acronyms

2D                 two-dimensional

AC                 alternating current

AFM                atomic force microscopy

APW+lo             augmented plane wave + local orbitals

DFT                density functional theory

DOS                density of states

EELS               electron energy loss spectroscopy

EF-TEM             energy filtered - transmission electron microscopy

FEG                field emission gun

FFT                fast fourier transform

FWHM               full width at half maximum

GGA                generalized gradient approximation

HAADF-STEM         high angular annual dark field - scanning transmission electron microscopy

HR-TEM             high resolution - transmission electron microscopy

ICP-AES            inductively coupled plasma - atomic emission spectroscopy

ITO                indium doped tin oxide

LDA                local density approximation

PBE-GGA            Perdew Burke Ernzerhof - generalized gradient approximation

| | |
|---|---|
| RHS | right hand side |
| SEM | scanning electron microscopy |
| SNR | signal-to-noise ratio |
| STEM | scanning transmission electron microscopy |
| TBA | tetra-$n$-butylammonium |
| TB-mBJ | Tran Blaha modified Becke Johnson potential |
| TEM | transmission electron microscopy |
| VEELS | valence electron energy loss spectroscopy |
| ZLP | zero loss peak |

# List of Symbols

$a_0$          first Bohr's radius

$A_{lm}^{\alpha,lo}$          first constant of normalization in the core-shell local orbital

$B_{lm}^{\alpha,lo}$          second constant of normalization in the core-shell local orbital

$c$          velocity of light in free space

$C_{lm}^{\alpha,LO}$          constant of normalization for semi-core local orbitals

$c_n$          coefficient of $\psi_n(x)$ in describing the state of particle

$C_s$          coefficient of spherical aberration

$\boldsymbol{D}$          electric displacement vector

$d_{50}$          extent of delocalization such that 50% of the excitations occur within this diameter

$e$          electron charge

$E$          energy

$\vec{E}$          electric field vector

$\bar{E}$          mean energy of scattering

$E_0$          energy of incident beam electron

$\Delta E$          energy shift for correctly modeling the semi-core states

$E_{1,l}^{\alpha}$          energy level in muffin tin region

$E_F$          Fermi energy

$E_g$          band gap

| | |
|---|---|
| $E_{IP}$ | energy loss of first inflection point |
| $E_{pi}$ | $i$th plasmon as defined by conditions $\varepsilon_1 = 0$ and $\frac{d\varepsilon_1}{dE} > 0$ |
| $\varepsilon$ | dielectric function |
| $\varepsilon_\infty$ | high frequency dielectric constant |
| $\varepsilon_0$ | low frequency dielectric constant |
| $\varepsilon_1$ | real part of the dielectric function |
| $\varepsilon_2$ | imaginary part of the dielectric function |
| $\epsilon_0$ | permittivity of free space |
| $f$ | generalized oscillator strength |
| $\gamma$ | relativistic correction factor |
| $\varphi_i(\vec{r})$ | single particle wave function |
| $\varphi_p$ | azimuthal angle in polar coordinate system |
| $\hbar$ | Planck's constant divided by $2\pi$ |
| $\widehat{H}$ | Hamiltonian operator |
| $\widehat{H}_{KS}$ | Kohn-Sham Hamiltonian |
| $i$ | square root of -1 |
| $In$ | interstitial region between muffin tin spheres |
| $I$ | intensity |
| $\boldsymbol{k}$ | momentum vector |
| $\boldsymbol{k_0}$ | momentum vector of the incident electron |
| $\boldsymbol{k_1}$ | momentum vector of the scattered electron |
| $k_x$ | extinction coefficient |
| $K_{max}$ | magnitude of largest plane wave used in the interstitial region |

| | |
|---|---|
| $l$ | angular momentum |
| $L_{FWHM}$ | FWHM of Lorentzian fit to the first derivative of the VEEL spectrum |
| $\lambda$ | mean free path length |
| $\lambda_e$ | wavelength of electron |
| $m$ | mass |
| $m_0$ | rest mass of electron |
| $m_e$ | mass of electron |
| $M_i$ | mass of $i$th nucleus |
| $n$ | refractive index |
| $n_a$ | number of atoms per unit volume |
| N | number of atoms |
| $p_x$ | momentum operator along the X-axis |
| $p_y$ | momentum operator along the Y-axis |
| $p_z$ | momentum operator along the Z-axis |
| $P_{a-b,t}$ | probability of finding a particle between positions a and b at time t |
| $\Psi$ | wave function of a particle |
| $\psi_n(x)$ | an eigenfunction of the Hamiltonian |
| $\psi_0$ | wave function describing the initial state of electron |
| $\psi_f$ | wave function describing the final state of electron after scattering |
| $\psi_k$ | single particle wave function at a point in a crystal |
| $\boldsymbol{q}$ | momentum transfer vector |
| $\boldsymbol{r}$ | position vector |
| $\vec{r_j}$ | position vector of $j$th electron |

| | |
|---|---|
| $\boldsymbol{R}$ | a vector integral multiple of a unit cell vector in a crystalline lattice |
| $R(r)$ | radial component of wave function $\psi(r, \theta_p, \varphi_p)$ |
| $R$ | Rydberg's energy |
| $\vec{R_i}$ | radius vector of $i$th nucleus |
| $R_{MT}$ | muffin-tin radius for an atom |
| $\rho$ | electron density |
| $S$ | loss function |
| $S_\alpha$ | region belonging to muffin-tin spheres |
| $d\sigma/d\Omega$ | differential scattering cross section |
| $\Omega$ | solid angle |
| $t$ | time |
| $d\tau$ | infinitesimally small volume element inside the atom |
| $\theta$ | scattering angle |
| $\bar{\theta}_E$ | characteristic angle of a scattering |
| $\theta_p$ | polar angle in polar coordinate system |
| $u_l^\alpha$ | radial function of normalization |
| $v$ | velocity of electron |
| $V$ | potential energy function |
| $V_{ext}$ | external potential |
| $V_H$ | Hartree operator |
| $V^{sp}$ | single particle potential |
| $V_{xc}$ | exchange correlation potential |
| $x$ | position along X-axis |

$\Delta x_{max}$       extent of maximum delocalization of an electron excitation

$Y(\theta_p, \varphi_p)$       angular component of wave function $\psi(r, \theta_p, \varphi_p)$

$Z$       atomic number

$Z_i$       atomic number of $i$th nucleus

# List of Tables

# 1    Introduction and motivation

The Dion-Jacobson phase perovskite $KCa_2Nb_3O_{10}$ and the two-dimensional (2D) nanosheets derived from it $[TBA_xH_{1-x}]^+[Ca_2Nb_3O_{10}]^-$, where $TBA^+$ is the bulky organic cation tetra-*n*-butlyammonium, constitute an important dielectric system [1]. The bulk $KCa_2Nb_3O_{10}$ is a perovskite where the Nb ions occupy the B-sites whereas the A-sites in the perovskite structure are taken by K and Ca ions in a layered fashion such that a layer of K ions on A-sites is followed by two layers of Ca ions. Chemical substitution in $KCa_2Nb_3O_{10}$ allows for replacement of K ions with bulk organic cation tetra-*n*-butlyammonium and protons. On replacement with the $TBA^+$ ions, the interlayer distance increases to a level such that the 2D-layers become independent of each other thereby leading to exfoliation into a 2D-nanostructure [2].

The crystal structure of $KCa_2Nb_3O_{10}$ was first proposed by Dion *et al.* [3] to be tetragonal. A subsequent X-ray powder diffraction study by Fukuoka *et al.* suggested [4] it to crystallize in orthorhombic symmetry. A rather recent study by Tokumitsu *et al.* [5] used single crystal neutron diffraction and refined the crystal structure to a monoclinic system. Computationally this structure model has not yet been optimized, doing so would lead to better understanding of octahedral distortions in the crystal structure.

$KCa_2Nb_3O_{10}$ has been suggested by various researchers for a wide array of potential applications [6-8]. Thangadurai *et al.* [6] have shown the utility of using $KCa_2Nb_3O_{10}$ as an ionic conductor. Domen *et al.* [7] have demonstrated the photocatalytic capability of $KCa_2Nb_3O_{10}$. Upon doping with $Eu^{3+}$ or $La^{3+}$ Bizeto *et al.* reported [8] $KCa_2Nb_3O_{10}$ to turn photoluminescent.

Valence electron energy loss spectroscopy (VEELS) in a transmission electron microscope (TEM) analyses the energy lost by electrons which pass through the probe materials, concentrating on the energies lost due to interaction of the beam electrons with the valence electrons. Typically the energy resolution of the VEELS experiments is among other things limited by the energy spread of the beam electrons [9]. Recent advances in instrumentation [10] have helped to improve the energy resolution with the use of commercially available

monochromators attached to TEMs. Scientists have successfully demonstrated the applicability of VEELS for determining the band gaps of various sorts of materials [9,11-14] using commercially available monochromators. In addition VEELS has also been demonstrated to be reliable method for experimentally determining the dielectric function [15-17].

Another technique [18] which has recently gained the attention of the scientific community in studying the band gap of materials is the Tran-Blaha modified Becke Johnson (TB-mBJ) potential within density functional theory (DFT). DFT has been well known to predict lower band gap values [19,20] than experimentally determined. This new technique (TB-mBJ) has performed well on a number of systems ranging from semiconductors to insulators [18]. From a point of view of pertinence, it is interesting to understand the possible applicability of these two methods (monochromated VEELS and TB-mBJ based DFT) for a dielectric material $KCa_2Nb_3O_{10}$.

With the synthesis of graphene in 2004 [21], the idea of 2D-materials has caught attention of scientific the community. Scientists have successfully been able to exfoliate 2D-nanostructures based on oxides [22], hydroxides [22], boron nitride [23] and metal disulphides [24]. These developments have thrust the advancements in potential applications of $KCa_2Nb_3O_{10}$ based 2D-nanosheets to forefront [25-29].

In the last decade $KCa_2Nb_3O_{10}$ has been used extensively to synthesize 2D nanosheets [2,30-33]. These 2D-nanosheets of $[TBA_xH_{1-x}]^+[Ca_2Nb_3O_{10}]^-$ have been reported to have potential applications in a number of technologies [25-29]. Compton *et al.* [25] showed the applicability of $[TBA_xH_{1-x}]^+[Ca_2Nb_3O_{10}]^-$ nanosheets for photochemical water splitting. Okamoto *et al.* showed [26] that such sheets upon Rh-doping could be used for $H_2$ production from water/methanol without catalyst loading. Sasaki and co-workers have reported the use of such nanosheets as potential nano dielectric materials [27,28]. In a recent report, Chang *et al.* showed the utility of $[TBA_xH_{1-x}]^+[Ca_2Nb_3O_{10}]^-$ nanosheets for building multi-junction polymer solar cells [29].

Two studies have already been published on the electronic structure of systems based on $[TBA_xH_{1-x}]^+[Ca_2Nb_3O_{10}]^-$ nanosheets. Compton *et al.* determined [25] the band gap of $[TBA_xH_{1-x}]^+[Ca_2Nb_3O_{10}]^-$ nanosheets after drying the suspension containing the nanosheets and performing diffuse reflectance measurements. Akatsuka *et al.* [34] determined the band gap of $[TBA_xH_{1-x}]^+[Ca_2Nb_3O_{10}]^-$ nanosheets of varying thickness upon deposition on indium-

doped tin oxide (ITO) substrate by performing photochemical measurements. Both these reports provide insights into the electronic structure of $[TBA_xH_{1-x}]^+[Ca_2Nb_3O_{10}]^-$ nanosheets however suffer from one common problem. These studies investigate the electronic structure of $[TBA_xH_{1-x}]^+[Ca_2Nb_3O_{10}]^-$ nanosheets which have been deposited on a surface and as such do not probe free standing nanosheets. In addition both the studies provide an average picture whereby the signal obtained from many sheets is analyzed in the evaluation of the band gap. Majority of the optical methods (like the ones used in the above mentioned studies [25,34]), fail to individually probe nanostructure because the light waves, by virtue of their wavelengths (wavelengths of the order of few hundred nm) are not able to locally probe individual nanosheets. As such, the electronic structure of individual freely suspended nanosheets is not well understood.

In this work DFT based *ab initio* calculations were performed on $KCa_2Nb_3O_{10}$ which should help in better understanding the octahedral distortions in the crystal structure. Moreover, in light of the possible applications of $KCa_2Nb_3O_{10}$ [6-8] these calculations shall allow for elucidation of the electronic properties of $KCa_2Nb_3O_{10}$ which are critical to these potential applications.

In this study, electronic structure of bulk $KCa_2Nb_3O_{10}$ is studied using DFT and VEELS. This shall test the correlation between these two techniques, i.e. monochromated VEELS and TB-mBJ potentials [18] in determining the band gap of $KCa_2Nb_3O_{10}$. A further comparison with photocatalysis measurement of Domen *et al.* [30] would allow for evaluating the success of these two approaches. Moreover from the calculations light could be shed upon the dielectric behavior of $KCa_2Nb_3O_{10}$.

Given the intense interest of the scientific community in the $[TBA_xH_{1-x}]^+[Ca_2Nb_3O_{10}]^-$ nanosheets, it is interesting to determine their electronic structure. The central objective of this study is to understand the electronic structure (band gap in particular) of individual $[TBA_xH_{1-x}]^+[Ca_2Nb_3O_{10}]^-$ nanosheets and its relation to the electronic structure of $KCa_2Nb_3O_{10}$. It is hoped that this work shall augment the understanding of this material family consisting of bulk $KCa_2Nb_3O_{10}$ and $[TBA_xH_{1-x}]^+[Ca_2Nb_3O_{10}]^-$ nanosheets.

## 1.1 Chapter references

[1]  B.-W. Li, M. Osada, Y. Ebina, T. C. Ozawa, R. Ma, and T. Sasaki. Impact of perovskite layer stacking on dielectric responses in $KCa_2Na_{n-3}Nb_nO_{3n+1}$ (n=3-6) Dion Jacobson homologous series. *Appl. Phys. Lett.* 96, 182903 (2010)

[2]  Y. Ebina, T. Sasaki, and M. Watanabe. Study on exfoliation of layered perovskite-type niobates. *Solid State Ionics* 151, 177 (2002)

[3]  M. Dion, M. Ganne, and M. Tournoux. Nouvelle familles de phases $M^IM^{II}_2Nb_3O_{10}$ a feuillets "perosvkite". *Mat. Res. Bull.* 16, 1429 (1981)

[4]  H. Fukuoka, T. Isami, and S. Yamanaka. Crystal structure of a layered perovskite niobate $KCa_2Nb_3O_{10}$. *J. Sol. State Chem.* 151, 40 (2000)

[5]  T. Tokumitsu, K. Toda, T. Aoyagi, D. Sakuraba, K. Uematsu, and M. Sato. Powder neutron diffraction study of layered perovskite $KCa_2Nb_3O_{10}$. *J. Cer. Soc. Jap.* 114, 795 (2006)

[6]  V. Thangadurai and W. Weppner. $AA'_2M_3O_{10}$ (A=K, Rb, Cs; A'=Ca ; M=Nb) layered perovskites: low temperature proton conductors in hydrogen atmospheres. *J. Mat. Chem.* 11, 636 (2001)

[7]  K. Domen, J. Yoshimura, T. Sekine, A. Tanaka, and T. Onishi. A novel series of photocatalysis with ion-exchangeable layered structure of niobate. *Cat. Lett.* 4, 339 (1990)

[8]  M. A. Bizeto, V. R. L. Constantino, and H. F. Brito. Luminescence properties of layered niobate $KCa_2Nb_3O_{10}$ doped with $Eu^{3+}$ and $La^{3+}$ ions. *J. Alloys Comp.* 311, 159 (2000)

[9]  L. Gu, V. Srot, W. Sigle, C. Koch, P. van Aken, F. Scholz, S. B. Thapa, C. Kirchner, M. Jetter, and M. Rühle. Band-gap measurements of direct and indirect semiconductors using monochromated electrons. *Phys. Rev. B.*, 75, 195214 (2007)

[10] R. F. Egerton. *Electron Energy-Loss Spectroscopy in the Electron Microscope.* Springer Science + Business Media Inc. (2011)

[11] J. Park, S. Heo, J. Chung, H. Kim, H. Lee, K. Kim, and G. Park. Bandgap measurements on thin dielectric films using monochromated STEM-EELS. *Ultramicroscopy* 109, 1183 (2009)

[12] R. Erni, and N. D. Browning. Quantification of size-dependent energy gap of individual CdSe quantum dots by valence electron energy-loss spectroscopy. *Ultramicroscopy*, 107, 267 (2007)

[13] S. Lazar, G. A. Botton, M. -Y. Wu, F. D. Tichelaar, and H. W. Zandbergen. Materials science applications of HREELS in near edge structure analysis and low-energy loss spectroscopy. *Ultramicroscopy* 96, 535 (2003)

[14] T. Kuykendall, P. Ulrich, S. Aloni, and P. Yang. Complete composition tunability of InGaN nanowires using a combinatorial approach. *Nat. Mat.* 6, 951 (2007)

[15] K. van Benthem, C. Elsässer, and R. H. French. Bulk electronic structure of $SrTiO_3$: Experiment and theory. *J. Appl. Phys.* 90, 6156 (2001)

[16] A. D. Dorneich, R. H. French, H. Müllejans, S. Loughin, and M. Rühle. Quantitative analysis of valence electron energy-loss spectra of aluminium nitride. *J. Microsc.* 191, 286 (1998)

[17] R. H. French, H. Müllejans, D. Jones. Optical properties of aluminum oxide: Determined from vacuum ultraviolet and electron energy-loss spectroscopies. *J. Am. Cer. Soc.* 81, 2549 (1998)

[18] F. Tran and P. Blaha. Accurate band gaps of semiconductors and insulators with a semilocal exchange correlation potential. *Phys. Rev. Lett.* 102, 226401 (2009)

[19] A. Seidl, A. Görling, P. Vogl, J. A. Majewski, and M. Levy. Generalized Kohn-Sham schemes and the band-gap problem. *Phys. Rev. B.* 53, 3764 (1996)

[20] W. Ku and A. G. Eguiluz. Band-gap problem in semiconductors revisited: effects of core states and many-body self-consistency. *Phys. Rev. Lett.* 89, 126401 (2002)

[21] K. S. Novoselov, A. K. Geim, S. V. Morozov, D. Jiang, Y. Zhang, S. V. Dubonos, I. V. Grigorieva, A. A. Frisov. Electric field effect in atomically thin carbon films. *Science* 306, 666 (2004).

[22] R. Ma and T. Sasaki. Nanosheets of oxides and hydroxides: Ultimate 2D charge-bearing functional crystallites. *Adv. Mater.* 22, 5082 (2010)

[23] J. Coleman *et al.* Two-dimensional nanosheets produced by liquid exfoliation of layered materials. *Science* 331, 568 (2011)

[24] K. S. Novoselov, D. Jiang, F. Schedin, T. J. Booth, V. V. Khotkevich, S. V. Morozov, and A. K. Geim. Two-dimensional atomic crystals. *PNAS* 102, 10451 (2005)

[25] O. C. Compton, E. C. Carroll, J. N. Kim, D. S. Larsen, and F. E. Osterloh. Calcium niobate semiconductor nanosheets as catalysts for photochemical hydrogen evolution from water. *J. Phys. Chem. Lett. C.* 111, 14589 (2007)

[26] Y. Okamoto, S. Ida, J. Hyodo, H. Hagiwara, and T. Ishihara. Synthesis and photocatalytic activity of Rhodium-doped calcium niobate nanosheets for hydrogen production from water/methanol system without cocatalyst loading. *JACS.* 133, 18034 (2011)

[27] M. Osada and T. Sasaki. Two-dimensional dielectric nanosheets: novel nanoelectronics from nanocrystal building blocks. *Adv. Mater.* 24, 210 (2012)

[28] B. Li, M. Osada, T. C. Ozawa, Y. Ebina, K. Akatsuka, R. Ma, H. Funakubo, and T. Sasaki. Engineered interfaces of artificial perovskite superlattices via nanosheet deposition process. *ACS Nano* 4, 6673 (2010)

[29] L. Chang, M. A. Holmes, M. Waller, F. E. Osterloh, and A. J. Moule. Calcium niobate nanosheets as novel electron transport material for solution-processed multi-junction polymer solar cells. *J. Mater. Chem.* 22, 20443 (2012)

[30] K. Domen, J. Yoshimura, T. Sekine, A. Tanaka, and T. Onishi. A novel series of photocatalysts with ion-exchangeable layered structure of niobates. *Catalysis Lett.* 4, 339 (1990)

[31] R. E. Schaak and Thomas E. Mallouk. Self-assembly of tiled perovskite monolayer and multilayer thin films. *Chem. Mater.* 12, 2513 (2000)

[32] M. Osada and T. Sasaki. Two-dimensional dielectric nanosheets: novel nanoelectronics from nanocrystal building blocks. *Adv. Mater.* 24, 210 (2012)

[33] B. Li, M. Osada, T. C. Ozawa, Y. Ebina, K. Akatsuka, R. Ma, H. Funakubo, and T. Sasaki. Engineered interfaces of artificial perovskite superlattices via nanosheet deposition process. *ACS Nano* 4, 6673 (2010)

[34] K. Akatsuka, G. Takanashi, Y. Ebina, M. Haga, and T. Sasaki. Electronic band structure of exfoliated titatium – and/or niobium based oxide nanosheets probed by electrochemical and photoelectrochemical measurements. *J. Phys. Chem. C* 116, 12426 (2012)

# 2    Methods and Materials

The understanding of structure and properties of calcium niobate perovskite family requires a basic understanding of some central concepts, terminology, details and techniques. This chapter is devoted to fostering the comprehension of these indispensible motifs. To begin with salient features of quantum mechanics are discussed. Using these concepts the band theory of solids is built upon and described about it are ways to understand semiconductors and dielectrics. Theory of dielectrics and its application for understanding the optical properties is discussed.

Perovskites, in general, and the properties of Dion-Jacobson phase $KCa_2Nb_3O_{10}$, in particular, are described. The principles of synthesis of two dimensional nanostructures are discussed along with their applicability for synthesizing perovskite nanosheets. Finally the structure and properties of calcium niobate perovskite nanosheets are detailed.

To understand the above mentioned material family, two methods of investigations are described. As the first method, transmission electron microscopy and electron energy loss spectroscopy were utilized. The interaction of electrons with matter and further the various techniques in transmission electron microscopy are explained. The energy loss suffered by electrons transmitted through a sample is summarized and is used to explain the excitations of valence and core-shell electrons. Density functional theory is described as a theoretical method for understanding the properties of solids. The terminology, approximations and methods employed in density functional theory are described.

## 2.1    Concepts in Solid State Physics

### 2.1.1    Formalism in Quantum Mechanics

This section is primarily based on the text *Introduction to Quantum Mechanics* by D. J. Griffiths [1].

Quantum mechanics approaches the problems of physics in a different manner than classical Newtonian mechanics. As most of the important theories ranging from band theory for

semiconductors to dielectric theory are based on the formalism of quantum mechanics, it is worthwhile describing the formalism. In quantum mechanics, Schrödinger's equation plays a role analogous to Newton's second law in Newtonian mechanics. The state of the particle is described in terms of its wave function $\Psi(x,t)$ which is obtainable solving the time-dependent Schrödinger's equation (Equation 2.1)

$$i\hbar\frac{\partial\Psi}{\partial t} = -\frac{\hbar^2}{2m}\frac{\partial^2\Psi}{\partial x^2} + V\Psi \tag{2.1}$$

where $\hbar$ is the Planck's constant divided by $2\pi$, $i$ square root of -1, $t$ time, $m$ mass and $V$ the potential energy function. An important corollary of Equation 2.1 being that knowledge of $\Psi(x,0)$ i.e. the initial conditions, solving the Schrödinger's equation allows for determining $\Psi(x,t)$ for later times. The dichotomous point between the two theories (classical and quantum mechanics) is the description of the state of a particle with the help of wave function. The wave function can be described with the help of Born's statistical interpretation which states that the probability $P_{a-b,t}$ of finding the particle at a point between positions $a$ and $b$ at time $t$ is described in Equation 2.2

$$\int_a^b |\Psi(x,t)|^2\, dx = P_{a-b,t} \tag{2.2}$$

where a and b are points in space.

Theories in solid state physics, like the density functional theory and band theory concern a steady state situation, i.e. the potential $V$ is independent of $t$, more specifically, the expectation value of all states is constant in time. For the case of steady state situations, the Schrödinger's equation takes the form (better known as time independent Schrödinger's equation) described in Equation 2.3

$$-\frac{\hbar^2}{2m}\frac{\partial^2\psi}{\partial x^2} + V\psi = E\psi \tag{2.3}$$

where $E$ is the expectation value of total energy. A more common way of representing the time independent Schrödinger's equation is in terms of Hamiltonian operator $\hat{H}$ as given in Equation 2.4.

$$\hat{H}\psi = E\psi \tag{2.4}$$

An infinite number of solutions $\psi_n(x)$ exist. The wave function can be expressed as a linear combination of these solutions (Equation 2.5) where $c_n$ is coefficient for $\psi_n$.

$$\psi(x,t) = \sum_{n=1}^{\infty} c_n \psi_n(x,t) \tag{2.5}$$

The formalism described until now can be expanded into three dimensions. The Hamiltonian obtained from classical mechanics can be written as shown in Equation 2.6

$$\hat{H} = \frac{1}{2}mv^2 + V = \frac{1}{2}m\left(p_x^2 + p_y^2 + p_z^2\right) + V \tag{2.6}$$

where the momentum operators can be described as $p_x = \frac{\hbar}{i}\frac{\partial}{\partial x}$ ; $p_y = \frac{\hbar}{i}\frac{\partial}{\partial y}$ ; $p_z = \frac{\hbar}{i}\frac{\partial}{\partial z}$.

For a potential with radial symmetry the wave function can be separated into radial and angular components as given in Equation 2.7

$$\psi\left(r, \theta_p, \varphi_p\right) = R(r)Y\left(\theta_p, \varphi_p\right) \tag{2.7}$$

where $R(r)$ and $Y(\theta_p, \varphi_p)$ are the radial and angular components of the wavefunction, $\theta_p$ and $\varphi_p$ being the polar and azimuthal angles respectively in the polar coordinates.

The solution of the time independent Schrödinger's equation is labyrinthine and requires a number of approximations for calculating it for crystals. Usage of density functional theory to solve it shall be described subsequently in Section 2.4.

2.1.2   Electrons in periodic potential

This section is based on the texts *Introduction to Quantum Mechanics* by D. J. Griffiths [1] and *Solid State Physics* by Ashcroft and Mermin [2].

In a crystal, the positions of atoms are well defined and possess translational and rotational symmetry. Felix Bloch formulated this fact into a mathematical theorem stating that when the potential in the single-particle Hamiltonian has the translation periodicity of the Bravais lattice, then $V^{sp}(\mathbf{r} + \mathbf{R}) = V^{sp}(\mathbf{r})$, where $V^{sp}$ is the single-particle potential and $\mathbf{R}$ a translation vector comprising of integral multiples of unit cell vectors. From this, one can deduce that the single-particle wave functions also follow translational symmetry as given in Equation 2.8.

$$\psi_k(\mathbf{r} + \mathbf{R}) = e^{i\mathbf{k}\cdot\mathbf{R}}\psi_k(\mathbf{r}) \tag{2.8}$$

The equation 2.8 relates the wave function at any given point in space from a known point. In the case that the two points are separated by an integral value of lattice constants, the wave functions at the two points are equivalent.

The periodicity of the crystal can be formulated in the reciprocal space which helps in the analysis using plane waves. The unit cell of the crystal in reciprocal space is defined as the Brillouin zone.

At zero Kelvin, the electrons fill up the energy levels till Fermi energy $E_F$. The band structure depicts the span of energy states (also sometimes referred to as bands) in the reciprocal space along specific directions. In a semiconductor there exist forbidden states, just above the Fermi energy, such that no states exist in those regions. Depending on the span of the states in the conduction and valence bands the semiconductor can be classified as direct or indirect. A schematic depicting the band structure of direct and indirect semiconductors is shown in Figure 2.1. In a direct band gap semi conductor, the top of the valence band and the bottom of the conduction band occur at the same coordinate along the momentum space. In the case of indirect semiconductors the top of the valence band and the bottom of the conduction band exist at different values of momentum in the momentum space. Therefore, for a transition of an electron from the valence into conduction bands only energy is required in the case of direct band gap semiconductor whereas both energy and momentum are required for the case of indirect semiconductor. The energy difference between the conduction band minimum and valence band maximum is known as the band gap. A semiconductor can allow passage of current through it by the movement of electrons or holes. A hole is the absence of an electron in an energy level which should be otherwise filled.
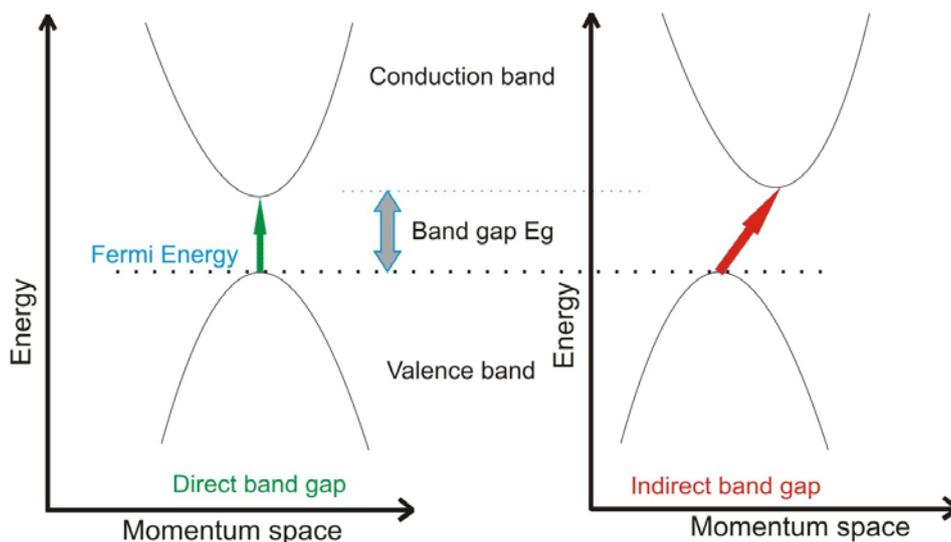


Figure 2.1: On the left, schematic of the bandstructure of a direct band gap semiconductor and on right of an indirect semiconductor are shown.

Semiconductors in addition can be classified into two categories, intrinsic and extrinsic. In an intrinsic semiconductor the carriers (electrons or holes), are contributed negligibly by any impurities (dopants) present. Extrinsic semiconductors on the contrary contain small amounts of dopant atoms, which contribute dominantly to the charge carriers, thereby accounting for most of the charge transfer.

### 2.1.3 Optical properties of solids and dielectric formalism

This section is based on the text *Optical properties of solids* by Mark Fox [3].

Optical properties of solids represent the response of the solid to applied electromagnetic fields. The electromagnetic fields inside a material differ from that in vacuum. The displacement $D$ is the electric field that would have been generated if instead of the solid, vacuum was present in the space being investigated. In the presence of a medium (solid), the electric field strength decreases by a factor of $\varepsilon$ where $\varepsilon$ is the dielectric function of the material. $\varepsilon$ is a complex tensor of the order 3x3 and it relates the components of electric displacement vector $D$ and the electric field $\vec{E}$ as given in Equation 2.9

$$D_\alpha = \sum_\beta \varepsilon_{\alpha\beta} \vec{E}_\beta \tag{2.9}$$

where $\alpha, \beta \in 1,2,3$.

The complex dielectric function contains two parts real and imaginary, related in Equation 2.10.

$$\varepsilon = \varepsilon_1 + i\varepsilon_2 \tag{2.10}$$

The optical properties like the refractive index $n$ and the extinction coefficient $k_x$ can be computed from $\varepsilon$ as shown in Equations 2.11 and 2.12.

$$n = \frac{1}{\sqrt{2}} \left( \varepsilon_1 + (\varepsilon_1^2 + \varepsilon_2^2)^{1/2} \right)^{1/2} \tag{2.11}$$

$$k_x = \frac{1}{\sqrt{2}} \left( -\varepsilon_1 + (\varepsilon_1^2 + \varepsilon_2^2)^{1/2} \right)^{1/2} \tag{2.12}$$

The real and imaginary parts of the dielectric function are not independent of each other. On applying Kramers Kronig transformation, one can be obtained from the other.

The loss function describes the energy loss suffered by an electron as it passes through a solid. The loss function $S$ can be described using the dielectric function as given in Equation 2.13.

$$S = Im\left(-\frac{1}{\varepsilon}\right) = \frac{\varepsilon_2}{[\varepsilon_1^2 + \varepsilon_2^2]} \tag{2.13}$$

As fast moving electrons pass through a solid, a predominant excitation that is induced in the material is that of plasmons. Plasmon is a collective oscillation mode of the valence or conduction band electrons of the solid, whereby, in addition to their random thermal motion, the electrons obtain a small collective motion component induced by the electromagnetic field changes due to the electron passing by. From the real part of the dielectric function the plasmon can be identified as the position where $\varepsilon_1$ crosses the energy axis with a positive slope.

An important approximation used in the study of collective excitations is the random-phase approximation. This was first proposed by Bohm and Pines [4] in 1951 and has since been constantly used in the study of collective excitations. The electrons of the material respond to the electromagnetic wave in two types of responses, occurring simultaneously. The first one is in-phase with the wave such that the phase difference between the electron response and the wave causing it is independent of the position. This response contributes to the collective organized excitations. The other response has a phase difference with the wave producing it and depends on the positions of the electrons. Given that the positions of the electrons are random, this second response tends to average out to zero when a large number of electrons are considered. Neglecting the contributions due to this second response in the analysis is called the random phase approximation [4].

## 2.2 Dion-Jacobson phase perovskite $KCa_2Nb_3O_{10}$ and nanosheets

2.2.1 Perovskites and their structure

Perovskites are inorganic compounds with the general formula $ABX_3$. The main feature of the perovskite structure is the octahedral coordinated polyhedron around the B-cations [5]. These octahedrons consist of anions X located at the corners of the octahedra with the cations B located at the center [5]. The octahedra share corners to form octahedral chains. In the cavities of these octahedra the cations A are located [5]. Generally the anion X is oxygen or fluorine [6], B a small transition metal cation like Ti, Nb [7] and A is a larger s-, d- or f-block cation like K, Sr [7].

Ideal arrangement of atoms in the perovskite structure generates a crystal structure within cubic system and space group *Pm3m* [5]. $SrTiO_3$ possesses the ideal perovskite structure with

cubic symmetry as shown in Figure 2.2. The Ti ions occupying the B sites at the center of octahedra with oxygen ions at X sites (corners of the octahedra). The Sr ions occupy the A sites in between the octahedra. Clearly as is evident from Fig. 2.2a, the perovskite structures contains multiple layers of A ions and $BX_3$ octahedra.
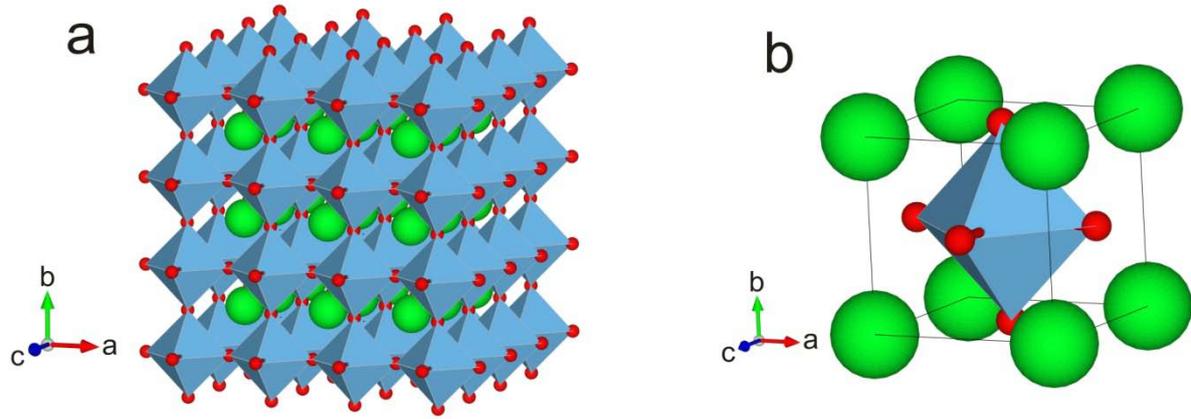


Figure 2.2: The structure of $SrTiO_3$ (a) showing the bluish grey octahedra consisting of Ti ions at the center and O atoms (in red) at the corners of the octahedra. The space between the octahedra is occupied by A site cation Sr (shown in green). On right (b) unit cell of $SrTiO_3$. Figures based on structure model proposed by Jauch and Palmer [8].

A large number of perovskites however deviate from the ideal perovskite structure. The divergence from the ideal structure is predominantly caused by the tilting of octahedra from ideal positions although they maintain their connectivity [5]. In addition, a common feature of the perovskite structure is that the A-site cations can be of different types, like the perovskites of Dion-Jacobson family [9,10] with a chemical formula $A'A_{k-1}B_kO_{3k+1}$, with $A'$ being a monovalent cation [11] generally Li, K, Na, Rb, Cs.

The structure of the Dion-Jacobson phase $A'Ca_2Nb_3O_{10}$ where $A'$ is Li, K, Na, Cs and Rb is shown in Figure 2.3. Depending on the size of cation $A'$ the layered structure containing three layers of $NbO_6$ octahedra modifies accordingly by rotation of the octahedra and the position of $A'$ cations. The significant point of difference between the different Dion-Jacobson phases is the local coordination of the alkaline cation. The local coordination number of the alkaline cation varies from 4 in $NaCa_2Nb_3O_{10}$ and 6 in $KCa_2Nb_3O_{10}$ to 8 in $RbCa_2Nb_3O_{10}$ and $CsCa_2Nb_3O_{10}$ [12].
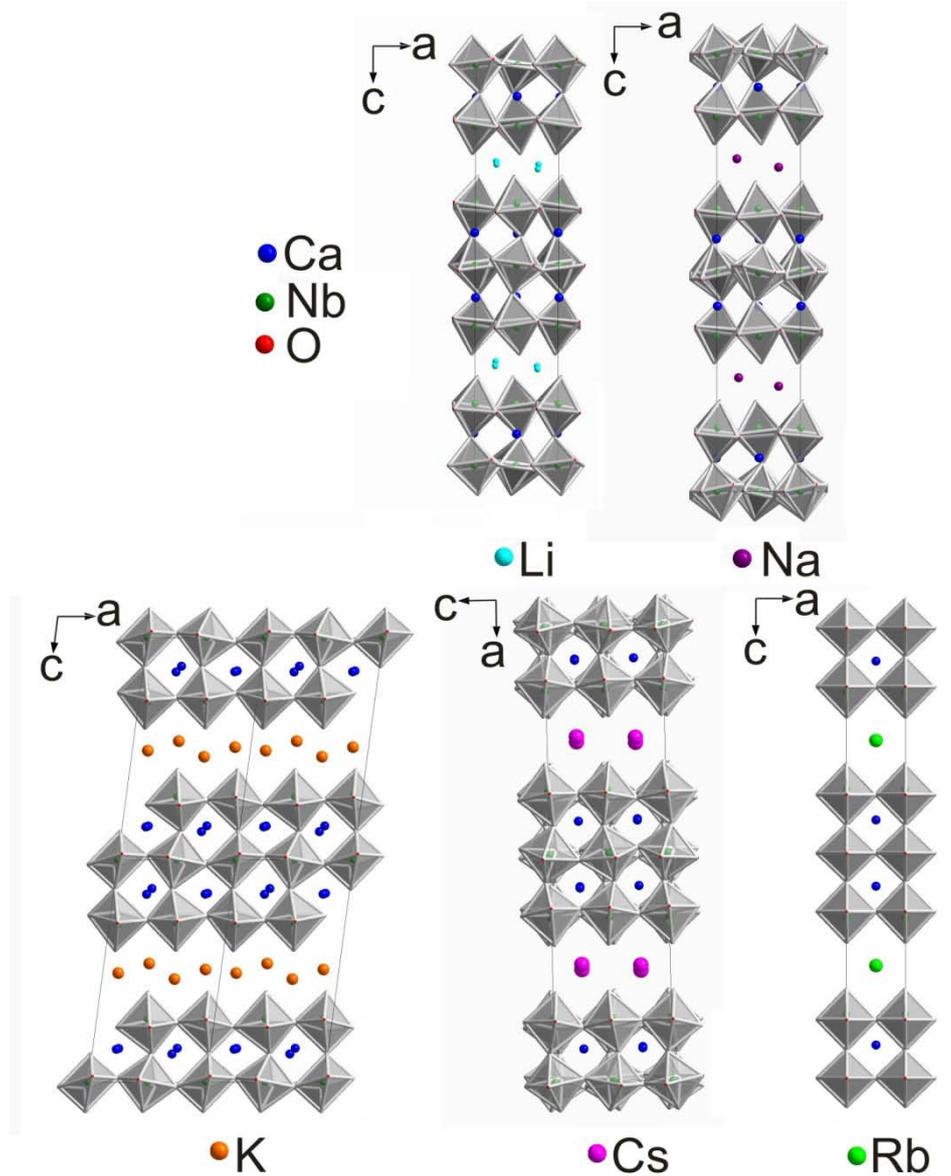
Figure 2.3: Structure of Dion-Jacobson phase $A'Ca_2Nb_3O_{10}$ where $A'$ is Li, K, Na, Cs and Rb. Figure based on structure models published in Refs. 13-17.

2.2.2 Dion-Jacobson phase $KCa_2Nb_3O_{10}$

The Dion-Jacobson phase $KCa_2Nb_3O_{10}$ has been an interesting material from various perspectives since it was first synthesized by Dion *et al.* in 1981 [9]. Dion *et al.* proposed, on the basis of X-ray measurements $KCa_2Nb_3O_{10}$ to have a tetragonal crystal structure [9]. Subsequently Fukuoka *et al.* [12] investigated the structure with the help of single crystal X-ray diffraction. They determined [12] $KCa_2Nb_3O_{10}$ to be orthorhombic with space group *Cmcm* (space group number 63), lattice parameters *a, b* and *c* to be 3.8802, 29.508 and 7.714 Å. Their structure model [12] however suffered from partial occupancies of O atoms on two

sites as is shown in Figure 2.4. Interestingly, they observed [12] stacking faults and twins in some of the crystals synthesized.
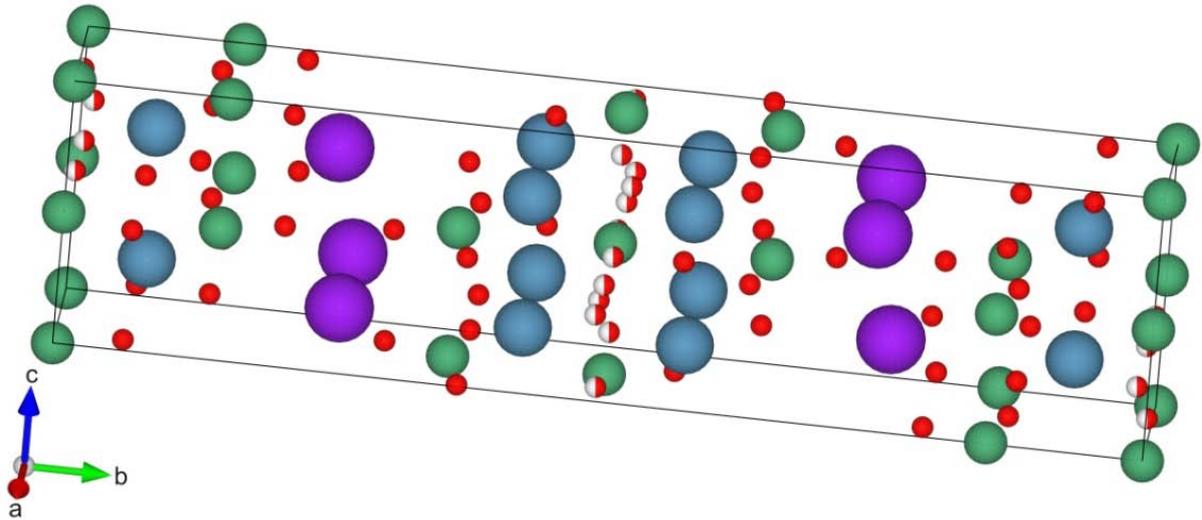


Figure 2.4: The orthorhombic crystal structure of $KCa_2Nb_3O_{10}$ as proposed by Fukuoka *et al.* [12] with atoms shown in the following coding, potassium (magenta), calcium (blue), oxygen (red) and niobium (green). The atoms depicted half-red have partial O occupancy of 0.5 on that site.

Subsequently, Tokumitsu *et al.* studied the crystal structure of $KCa_2Nb_3O_{10}$ using powder neutron diffraction [13] suggesting it to have a monoclinic structure of space group *P2$_1$/m* (space group number 11) and lattice parameters *a, b, c* and γ to be 7.7418, 7.7073, 14.859 Å and 97.51° respectively. They argued [13] the preponderance of their model against that of Fukuoka *et al.* [12] on the basis of the fact that neutron beams interact with the nuclei more strongly as compared to X-rays. In addition they took into account some weak reflections [13] which had been left out for the refinement of Fukuoka *et al.* [12]. The crystal structure of $KCa_2Nb_3O_{10}$ determined by Tokumitsu *et al.* is shown in Figure 2.5. The rotation of the $NbO_6$ is clearly apparent. This structure model [13] does not suffer from partial occupancies. The crystal structure highlights the layered perovskite structure with layers of K, Ca, and Nb cations.
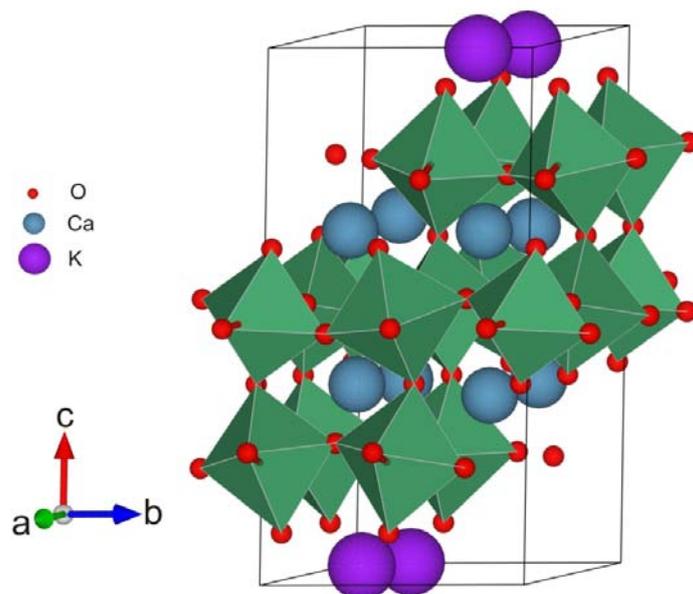
Figure 2.5: The crystal structure of $KCa_2Nb_3O_{10}$ as determined by Tokumitsu *et al.* [13] with the oxygen, calcium and potassium atoms shown in red, blue and magenta. The Nb atoms are located at the center of the green octahedra with oxygen atoms at the extremities.

$KCa_2Nb_3O_{10}$ is an interesting material with wide variety of potential applications in sight. Thangadurai and Weppner demonstrated the use of $KCa_2Nb_3O_{10}$ as an ionic conductor [18]. Domen *et al.* showed its applicability as a photocatalyst [19]. Fukuoka *et al.* observed superconductivity upon Li intercalation [20]. Bizeto *et al.* found $Eu^{3+}$ and $La^{3+}$ doped $KCa_2Nb_3O_{10}$ to be luminescent [21]. Recently Akatsuka *et al.* evinced the applicability of $KCa_2Nb_3O_{10}$ as a dielectric [22]. Despite a number of potential application, the electronic structure of $KCa_2Nb_3O_{10}$ is not well understood.

For the measurements performed on $KCa_2Nb_3O_{10}$ discussed in this work, $KCa_2Nb_3O_{10}$ was synthesized in a manner akin to that proposed by Jacobson *et al.* [10]. The synthesis was carried out by Pirmin Ganter and Christian Ziegler; the details of synthesis have been previously reported [23]. Commercially available powders of $K_2CO_3$, $CaCO_3$ and $Nb_2O_5$ were mixed in a molar ratio 1.1:4:3 and ground. Mixture was pre-heated at 900°C and then fired up to 1200°C for 60 hours. The purity of as-synthesized $KCa_2Nb_3O_{10}$ was confirmed by powder X-ray diffraction.

## 2.2.3 $[TBA_xH_{1-x}]^+[Ca_2Nb_3O_{10}]^-$ nanosheets

The discovery of graphene in 2004 [24] accentuated the possibility of synthesizing two-dimensional (2D) structures. This caught the attention of scientists worldwide who tried to

synthesize 2D structures by delaminating other materials. Success has been achieved in synthesizing 2D structures based on oxides [25], boron nitride [26], metal dichalcongenides [27] and metal disulphides [26-28]. Scientists have been able to successfully exfoliate the $KCa_2Nb_3O_{10}$ structure by replacing the $K^+$ with bulky organic ligands [29-30]. Delamination of $KCa_2Nb_3O_{10}$ was first successfully performed about two decades ago by Treacy and co-workers [31]. The recent interest [22,29,30,32,33] in this exfoliated 2D-nanostructure comes from the possibility of making complex hetero-nanostructures from it [25]. Sasaki and co-workers have demonstrated its potential use as a nano-dielectric [32,33]. Compton and co-workers demonstrated the utility of these nanosheets for photochemical water-splitting [34]. Recently Chang and co-workers [35] have demonstrated the utility of these nanosheets as electron transport material in polymer organic solar cells. With such a wide number of possible electronic applications in sight, it becomes worthwhile investigating the electronic properties of these nanosheets, especially the band gap.

These $[TBA_xH_{1-x}]^+[Ca_2Nb_3O_{10}]^-$ nanosheets have a structure similar to that of $KCa_2Nb_3O_{10}$ a fact highlighted in Figure 2.6. The $K^+$ ions get chemically replaced by protons and tetra-*n*-butylammonium ions ($TBA^+$). This layer of bulky cations and protons increases the distance between the $[Ca_2Nb_3O_{10}]^-$ layers to such an extent that they become independent of one another, thereby leading to the formation of independently existing 2D-nanosheets. The $TBA^+$ ions do not take any particular crystallographic positions, unlike $K^+$, partly due to their huge size.
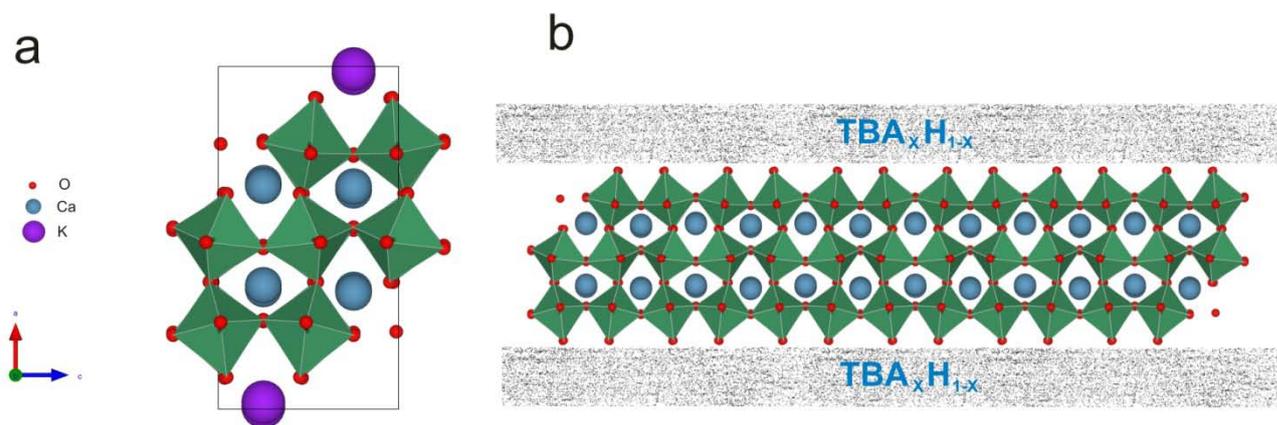


Figure 2.6: Schematic of $KCa_2Nb_3O_{10}$ unit cell (a) and $[TBA_xH_{1-x}]^+[Ca_2Nb_3O_{10}]^-$ nanosheet (b).

The measurement shown in this work were performed on $[TBA_xH_{1-x}]^+[Ca_2Nb_3O_{10}]^-$ nanosheet synthesized by Pirmin Ganter and Christian Ziegler; details have been detailed elsewhere

[23]. Synthesis was carried out using a method similar to the one of Ebina *et al.* [30]. 1g $KCa_2Nb_3O_{10}$ was treated with 5M $HNO_3$ (40 $cm^3$) for four days with daily renewal of acid that culminated in the conversion to protonic oxide $HCa_2Nb_3O_{10} \cdot 1.5H_2O$, the product being recovered with filtration, washing with water and air-drying. 0.2 g of product was dispersed in 50 $cm^3$ of tetra-*n*-butlyammonium hydroxide 30-hydrate aqueous solution mixed in the molar ration 1:1 and subsequently shaken for four weeks at a rotational speed of 200 rpm. The composition of the synthesized $[TBA_xH_{1-x}]^+[Ca_2Nb_3O_{10}]^-$ nanosheets was determined by inductively coupled plasma-atomic emission spectroscopy (ICP-AES) suggesting *x ≈ 0.8*.

# 2.3 Transmission electron microscopy and electron energy loss spectroscopy

To experimentally study the properties of $KCa_2Nb_3O_{10}$ and $[TBA_xH_{1-x}]^+[Ca_2Nb_3O_{10}]^-$ nanosheets the transmission electron microscope can be used in a number of possible ways. As such, it is apt that a discussion of such experiments should be preceded by a description of the transmission electron microscopy and the electron energy loss spectroscopy. This section and its constituent subsection detail the physical principles, instrumentations and the various modes involved with these two techniques.

2.3.1 Electron interactions with matter

This section is based on the texts *Transmission electron microscopy, A textbook for Materials Science* by D. B. Williams, C. B. Carter [36] and *Electron energy-loss spectroscopy in the electron microscope* by R. F. Egerton [37].

Despite the multitude of varieties in which the electron microscopes are used worldwide today, similarities exist in the manner in which the electrons interact with the matter. When a fast moving electron, like in a transmission electron microscope enters the sample, it interacts with the nuclei and the electrons of the material. These interactions induce change in the path, energy and phase of the electrons. Each, or a combination of these changes to the electrons allow for getting information about the sample. The principle interactions are depicted in Figure 2.7. Typically, the samples used in the electron microscope are very thin ~100nm or thinner [36]. As a consequence, majority of the electrons go through the sample. Some however do get backscattered due to the interactions with the nuclei. The transmitted electrons that pass through the sample could have lost some energy (inelastically scattered) or lost no energy (elastically scattered electrons). The majority of imaging techniques used in a

TEM primarily utilize an admixture of the unscattered and the elastically scattered electrons. The electron energy loss spectroscopy and consequentially the energy filtered - transmission electron microscopy (EF-TEM) uses the inelastically scattered electrons for analysis. The secondary (electrons of the sample ejected due to inelastic collisions with the probing electrons) and the backscattered electrons are used in the scanning electron microscopes; these signals are generally not analyzed in the TEM. As the probing electrons have high energies, typically between 60 and 300 keV in a commercial TEM, X-rays and Auger electrons are also generated; analyzing them offers insights into the chemical nature of the material. Auger electron detectors are generally not available with commercial TEMs but X-ray spectroscopes are.
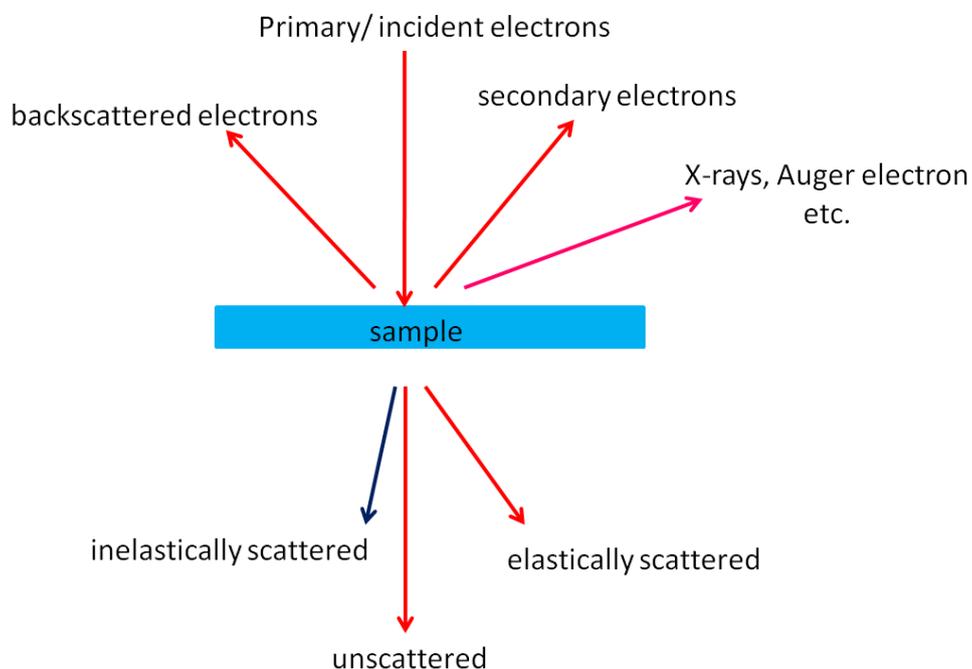


Figure 2.7: Schematic showing the various types of signals generated due to interactions of probing electrons with the sample.

2.3.2 Instrumentation in a TEM

This section is based on the text *Transmission electron microscopy, A textbook for Materials Science* by D. B. Williams and C. B. Carter [36].

The TEM was first developed by Ruska and Knoll [38] and inherent features of their design have stood the test of time. The modern TEM consists of a number of intricate pumps, lenses and detectors to name a few, which ultimately allow for the utility of the microscope. A schematic of a TEM is shown in Figure 2.8. At the top is the electron source (also known as

the electron gun) from which electrons are emitted. The electron gun can be of three types, thermal, field or Schottky. The thermal gun ejects electrons when the source is heated beyond a particular temperature (therefore thermal sources are made of tungsten filament) while the field emitter ejects electrons when a very high electric field is applied to it and electrons tunnel out. Consequentially the field emission guns have a sharp needle like geometry so as to intensify the effective electric field at the tip of the needle as governed by the Fowler-Nordheim Theory [39]. The Schottky source functions on the basis of a mixture of the thermal and field emission processes whereby both heat and electric field are applied to eject the electrons. Schottky emitters often have a $ZrO_2$ coating which further reduces the potential barrier that electrons need to overcome.

Right below the electron gun, the electrostatic terminals connected to the high-tension tank are located which accelerate the ejected electrons to the required energy. These are succeeded by a number of lenses and apertures, primarily the condenser and objective aperture-lens systems. The condenser lens system controls the intensity of the beam used for illuminating the sample and the electron beam size whereas the objective lens system accounts for the focus conditions for imaging. Adjacent to the objective lens system (in some configurations of the microscope inside the objective lens) lies the position for the specimen. Typically, the specimen is placed on a holder which is inserted into the column. The goniometer positions the sample at this location 'inside' or adjacent to the objective lens. The goniometer is used for moving or tilting the sample. The apertures of the objective lens allow for choosing the forward scattered beam or specific diffracted beams. This subsequently helps in choosing the bright field, the dark field or the high resolution transmission electron microscopy (HR-TEM) modes.

The objective lens system is followed by the intermediate lens and the projector lens system which magnifies the image made by the objective lens system. When changing the strength of the intermediate lens, a diffraction pattern can be obtained on the screen. In the diffraction mode, a selected area aperture governs the area of the sample exposed to the radiation. In the diffraction mode, the intermediate lens selects the back focal plane of the objective lens as the object. In the imaging mode, the first image obtained by the objective lens is used as object and further magnified. Finally a fluorescent screen / detector is positioned at the bottom of the column to obtain the images or diffraction pattern. In the case of electron energy loss spectroscopy, the EELS detector is positioned below the fluorescent screen, which is lifted and the electrons go through the entrance aperture to the EELS detector.
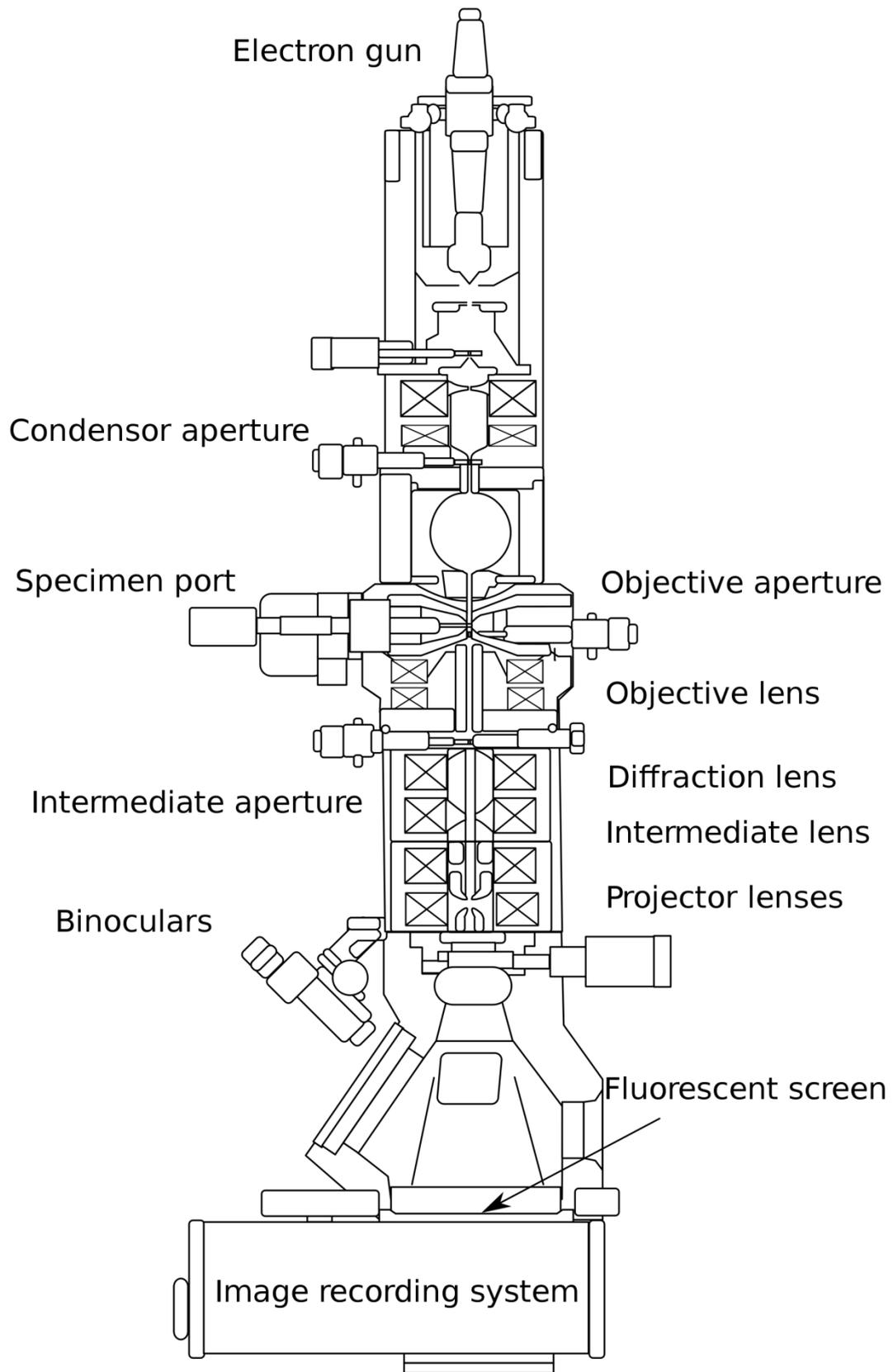
Figure 2.8: Assembly of a TEM (Image accessed from Wikimedia Commons, used under GNU Free Documentation License, Version 1.2).

2.3.3 High resolution transmission electron microscopy

This section is based on the text *Transmission electron microscopy, A textbook for Materials Science* by D. B. Williams, C. B. Carter [36].

High resolution transmission electron microscopy (HR-TEM) is a phase contrast imaging mode whereby the waves interact with each other and on the bases of their phase difference generate the image. In modern TEMs acquiring HR-TEM images is becoming a routine affair, however their interpretation could be tricky especially in the cases of nano-structures. The biggest success of HR-TEM lies in its ability to provide atomic resolution as is shown in Figure 2.9 for the case of a silicon crystal oriented in the $[1\bar{1}0]$ zone axis, showing the (110) and (111) planes. The fast fourier transform (FFT) of the HR-TEM image entails the details embedded in the image as a function of the spatial frequencies chosen (which are governed by the focusing conditions). The FFT of an HR-TEM image is analogous to the selected area diffraction pattern observed from the region imaged.
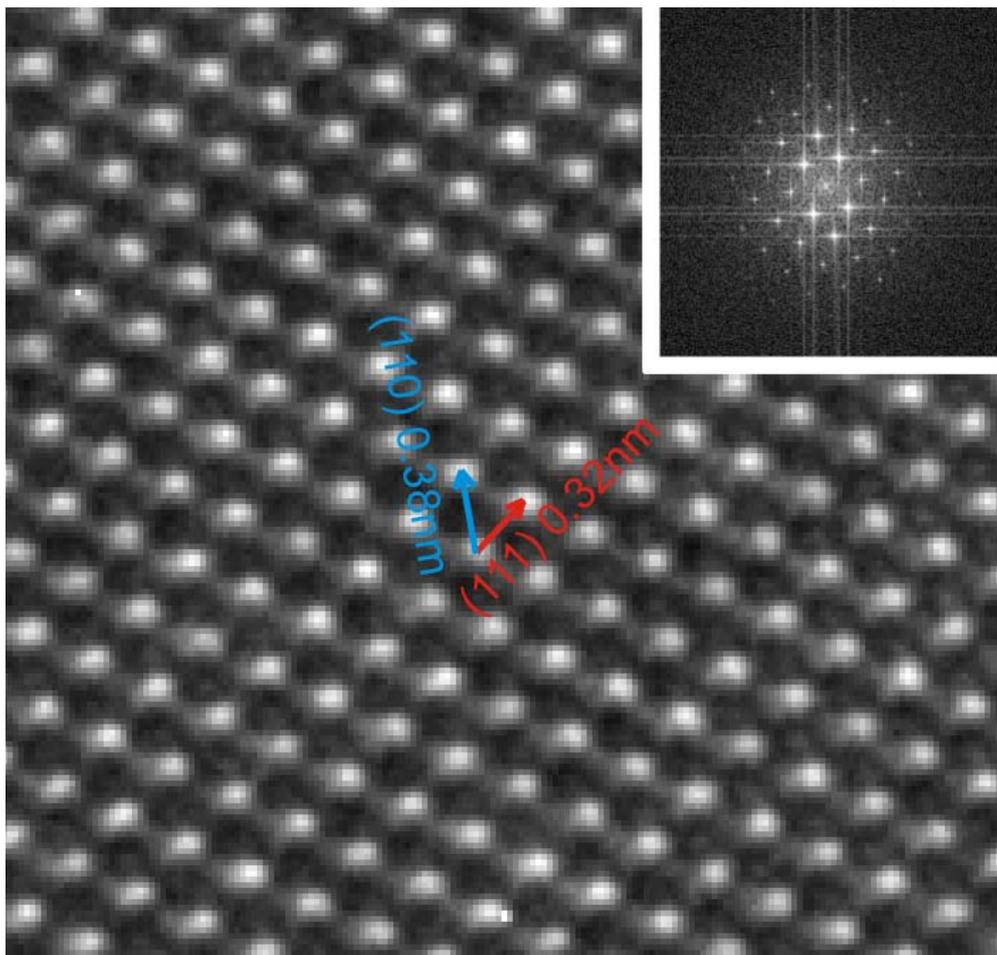


Figure 2.9: HR-TEM image of silicon showing the (110) and (111) planes when oriented in the $[1\bar{1}0]$ zone-axis along with the FFT (inset).

2.3.4 High angular annular dark field scanning transmission electron microscopy

This section is based on the text *Transmission electron microscopy, A textbook for Materials Science* by D. B. Williams, C. B. Carter [36].

The HR-TEM images despite the plethora of information that they provide in terms of resolution, lack a certain feature. These images are *per se* phase contrast images, i.e. changing the phase with the help of the objective lens excitation changes the way particular positions are visualized in the image. High angular annular dark field scanning transmission electron microscopy (HAADF-STEM) offers a way out as in the HAADF-STEM mode the contrast is due to the Rutherford scattering and is linked to the atomic column positions.

In the HAADF-STEM mode, a convergent beam is scanned across the sample and the annular detectors measure the signal emanating from the points being scanned. The intensity in HAADF-STEM mode images is related to the mass-thickness of the material, i.e. thicker areas, or areas with higher average atomic number appear brighter. Typically at high resolutions (atomic scales) the intensity in HAADF-STEM mode is related to $Z^2$ whereby $Z$ is the average atomic number of the material. The resolution is governed by the electron probe size.

2.3.5 Physics of electron energy loss spectroscopy

This section is based on the text *Electron energy-loss spectroscopy in the electron microscope* by R. F. Egerton [37].

Electron energy loss spectroscopy is based on the analysis of the energy lost by transmitted electrons as they pass through a given material. The energy lost by the electrons is indicative of the excitations induced in the material.

As a fast moving electron moves through a sample, it interacts with the electrons and the nuclei of the material. In scattering theory, such interactions are studied in terms of differential cross section $d\sigma/d\Omega$ which represents the probability of an incident electron being scattered (per unit solid angle $\Omega$) [37]. The situation can be visualized according to the following schematic (Figure 2.10). The incident electron with momentum vector $\boldsymbol{k_0}$ scatters through an angle $\theta$ and a scattering vector (also referred to as momentum transfer vector) $\boldsymbol{q}$ to attain a momentum $\boldsymbol{k_1}$.

The momentum transfer vector can be calculated as given in Equation 2.15

$$q^2 = k_0^2(\theta^2 + \bar{\theta}_E^2) \tag{2.15}$$

where $\bar{\theta}_E$ is the characteristic angle corresponding to the mean energy loss $\bar{E}$. $\bar{\theta}_E$ can be calculated as given in Equation 2.16

$$\bar{\theta}_E = \bar{E}/(\gamma m_0 v^2) \tag{2.16}$$

where $\gamma^2 = (1 - v^2/c^2)^{-1}$, $v$ the velocity of the incident electron, $c$ the velocity of light in free space and $m_0$ the rest mass of electron.
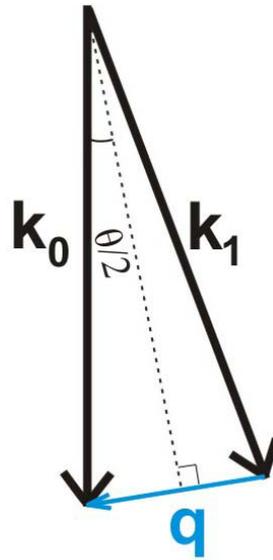


Figure 2.10: Schematic illustrating the initial and final momentum vector of the probing electron $\boldsymbol{k_0}$ and $\boldsymbol{k_1}$ respectively along with scattering vector $\boldsymbol{q}$ and scattering angle $\theta$.

In order to describe the scattering more precisely, the behavior of the electrons in the solid must be specified in terms of transition from an initial state wavefunction $\psi_0$ to a final state $\psi_f$. This was incorporated in the Bethe Theory as related in Equation 2.17, where $V(r)$ is the potential responsible for the scattering and $d\tau$ infinitesimally small volume element.

$$\frac{d\sigma_f}{d\Omega} = \left(\frac{m_0}{2\pi\hbar^2}\right)^2 \frac{k_1}{k_0} \left|\int V(r)\psi_0\psi_f^*\exp(i\boldsymbol{q}\cdot\boldsymbol{r})d\tau\right|^2 \tag{2.17}$$

Given that inelastic scattering is an important phenomenon for consideration, it is worth considering the double differential scattering cross section $d^2\sigma/d\Omega dE$ (the probability of an

electron getting scattered through a solid angle $\Omega$ and losing energy $E$) which can be described as given by Equation 2.18

$$\frac{d^2\sigma}{d\Omega dE} \approx \frac{4\gamma^2 R}{Ek_0^2}\left(\frac{1}{\theta^2+\overline{\theta}_E^2}\right)\frac{df}{dE} \tag{2.18}$$

where $f$ is the generalized oscillator strength and $R$ is the Rydberg's energy.

Another method of describing the double differential scattering cross section is with the help of the dielectric formulation of energy loss. It has been shown that the double differential scattering cross section can be described as given in Equation 2.19 where $a_0$ is the first Bohr's radius, $n_a$ is the number of atoms per unit volume and $\varepsilon$ the dielectric function.

$$\frac{d^2\sigma}{d\Omega dE} \approx \frac{Im\left[-1/\varepsilon(\boldsymbol{q},E)\right]}{\pi^2 a_0 m_0 v^2 n_a}\left(\frac{1}{\theta^2+\overline{\theta}_E^2}\right) \tag{2.19}$$

Clearly, the double differential cross section is proportional to the loss function $S = Im\left[-1/\varepsilon(\boldsymbol{q},E)\right]$.

The relativistic motion of electrons is accounted for in the above equations, however, under certain cases another energy loss process, namely the Cerenkov radiation can occur, which is not accounted for in the equations given above. When the speed of electrons travelling in a medium exceeds the phase velocity of light in that medium, light waves are generated, and the phenomenon called as Cerenkov radiation. When the criterion given in Equation 2.20 is satisfied, Cerenkov radiation is generated.

$$\varepsilon_1(E) > \frac{c^2}{v^2} \tag{2.20}$$

Cerenkov radiation is strongly dependent on two factors, the angular range of collection and the thickness of the sample being investigated. von Festenberg showed [40,41] that Cerenkov radiations contribute significantly to the energy loss spectrum acquired only at very low angles < 0.01 mrad. In addition, Cerenkov radiations contribute negligible scattering cross section when the thickness of the sample probed is less than 0.5 times the inelastic mean free path length of the material investigated [42].

A typical EEL spectrum has three main parts, as is shown in Figure 2.11. The most intense feature is the zero loss peak (ZLP), which basically represents all the electron which have lost no perceptible energy. As the ZLP primarily shows the energy spread of electrons which have lost no perceptible energy interacting with the specimen, it offers insight into the electron

source and spectrometer resolution. Typically for a thermal source, the full-width at half the maximum (FWHM) of the ZLP could be as less as 1 eV, for a Schottky source 0.6 eV and for a cold field emission gun 0.3 eV. Using a monochromator the resolution can be further improved to a FWHM of about 0.1 eV.

At greater energy loss values , the valence loss excitations are envisaged, typically up to 50 eV. These energy losses occur when the primary beam interacts with the valence band electrons, which in turn respond to the changing electromagnetic field by jumping to higher energy levels or by collective excitation modes like the plasmon.

At higher energy loss values, the excitation of core shell electrons are envisaged in the loss spectrum as the core-loss edges. The classification system used for these excitations is such that excitations from 1s states to higher unoccupied levels are known as K-edges, from 2s as $L_1$-edges, from $2p_{1/2}$ and $2p_{3/2}$ as $L_{2,3}$-edges, from 3s as $M_1$-edges, from $3p_{1/2}$ and $3p_{3/2}$ as $M_{2,3}$-edges, from $3d_{3/2}$ and $3d_{5/2}$ as $M_{4,5}$-edges and so on for higher levels.
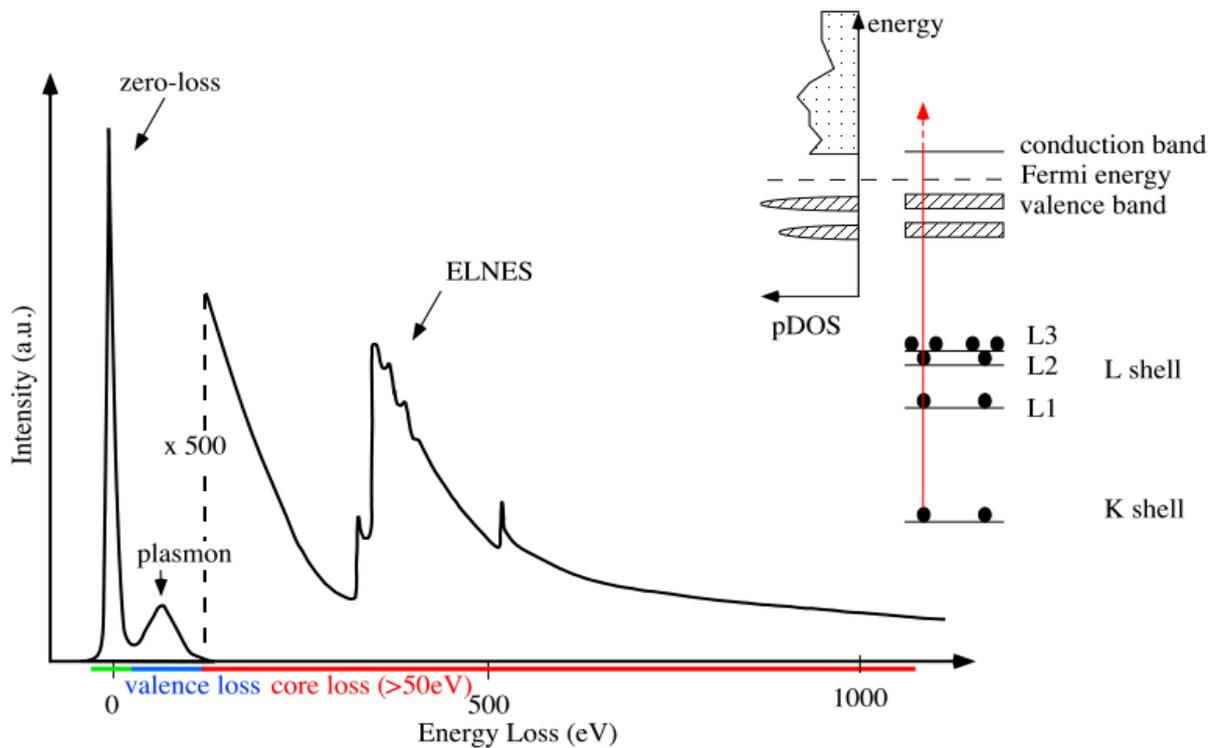


Figure 2.11: A typical EEL spectrum showing the zero loss peak, the valence excitations and the core-loss excitations. On right is a schematic of the energy levels in the solid. Adapted from Ref. 43. Image © C. Scheu, reproduced with permission.

27

2.3.6 Electron energy loss spectroscopy Instrumentation

This section is based on the text *Electron energy-loss spectroscopy in the electron microscope* by R. F. Egerton [37].

The acquisition of the loss spectrum requires an array of intricate technologies. One common feature which improves the energy resolution, and hence expands the amounts of information extractable in modern TEMs is the monochromator. The monochromator typically tightens the energy width of the electron source, at the cost of reducing the beam intensity. A schematic of Wien-type monochromator is shown in Figure 2.12. The operating principle of this type of monochromator is based on classical electrodynamics and similar to an EELS spectrometer described below. The beam of electrons is perpendicularly subjected to orthogonal electric and magnetic fields, their magnitudes being chosen such that electrons of a particular velocity experience no net force, thereby passing through undeviated. A slit is positioned right below to separate these electrons from those with differing energies. A side effect of using a Wien-type monochromator is that the beam current decreases. This setback can however been rectified by using a higher acquisition time, if the material under investigation in not beam sensitive.
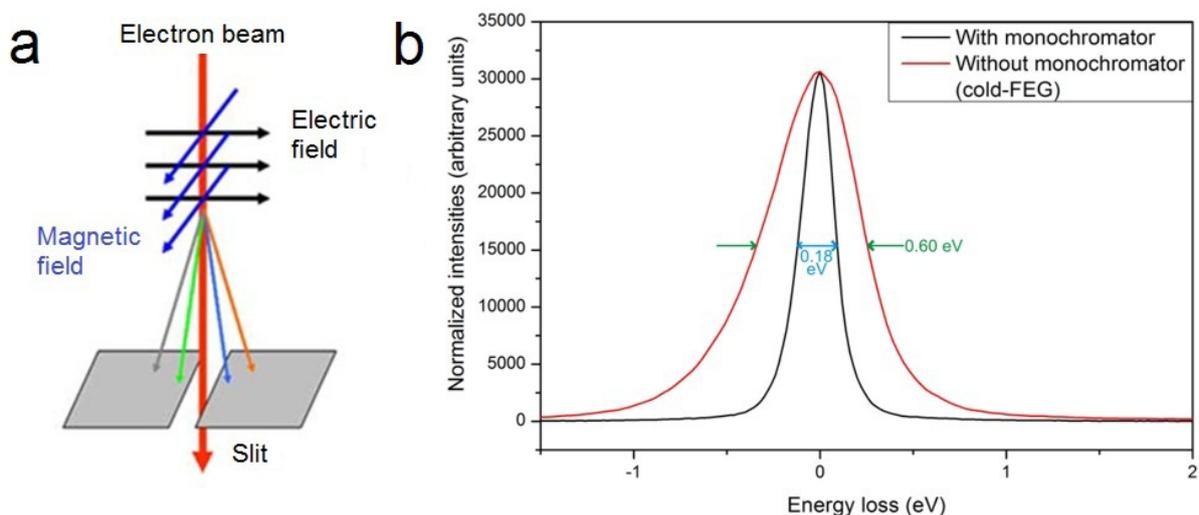


Figure 2.12: On the left (a) a schematic of a Wien-type monochromator which operates by inducing on to the electron beam orthogonal electric and magnetic fields. Improvement in the energy resolution due to the narrowing of the ZLP from a FWHM of 0.60 eV to 0.18 eV (b). Image © Yaron Kauffmann, Technion-Israel Institute of Technology, reproduced with permission.

The energy loss spectrum is acquired by the energy loss spectrometer which is located beneath the fluorescent screen. A schematic of the EEL spectrometer is shown in Figure 2.13. The entry of the electron beam into the spectrometer is governed by the spectrometer entrance aperture. The size and position of the spectrometer entrance aperture governs the momentum transfer $q$.

Below the entrance aperture a magnetic prism is located which applies magnetic field on the beam such that electrons get separated on the basis of their energy. After the prism several lenses follow which determine the magnification of the spectrometer. A detector can be placed to determine the energy spread of the electrons in the spectrum mode, whereby the EEL spectrum is obtained. Another possible feature is using electrons with a particular energy loss (selected with the help of an energy selecting slit) to subsequently make an image of the area probed using these electrons. This technique is commonly referred to as energy filtered transmission electron microscopy (EF-TEM).

Typically, the EELS can be operated in three modes. The first, namely the image mode whereby paraxial illumination is used, second the diffraction mode, whereby the TEM is operated in diffraction mode, or the STEM mode whereby a convergent beam scans the probe.
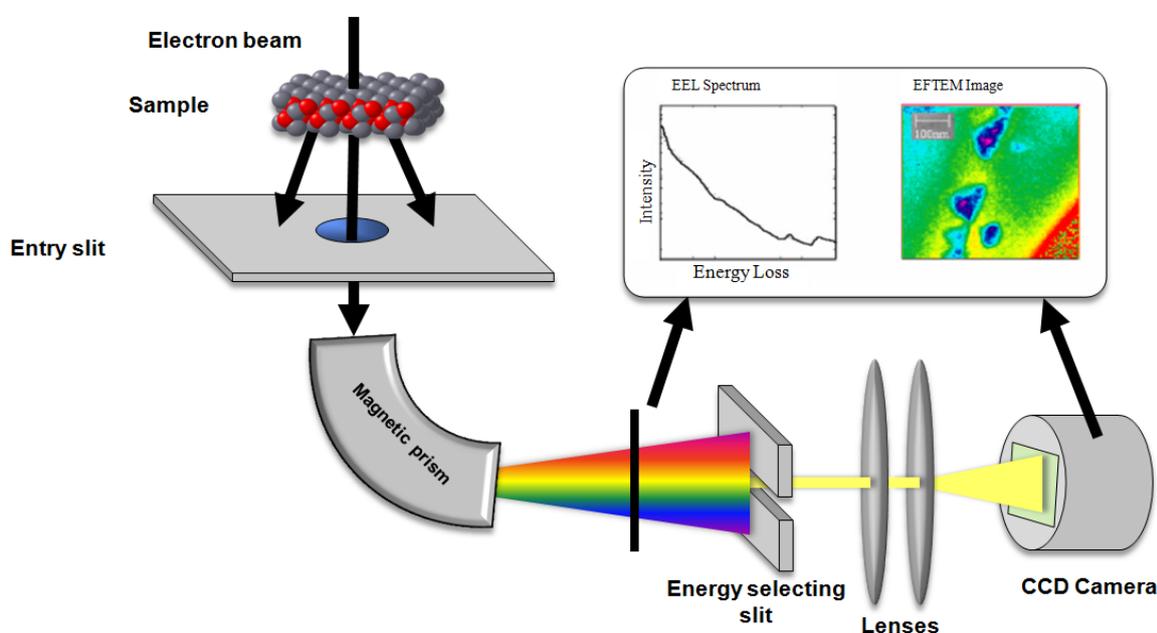


Figure 2.13: A schematic of the EEL spectrometer. Image © Yaron Kauffmann, Technion-Israel Institute of Technology, reproduced with permission.

2.3.7 Applications of electron energy loss spectroscopy

This section is based on the text *Electron energy-loss spectroscopy in the electron microscope* by R. F. Egerton [37].

Electron energy loss spectroscopy offers a plethora of information about the material investigated. Different sets of information require specific analysis and as such are dealt with differently. The excitations up to about 50 eV are predominantly caused by the excitations of the valence electrons and the spectrum spanning this energy range is referred to as valence electron energy loss spectrum (VEELS).

In a semiconducting material, the smallest possible valence electron excitation possible is the excitation of an electron from the top of the valence band to the bottom of the conduction band. Extracting the band gap from VEELS is challenging because the ZLP typically has tails which extend to higher energies. Therefore, the scattering cross section due to this excitation of electrons from valence to conduction bands can get overshadowed by the tail of the ZLP. Usage of a monochromator decreases the span of the tails of ZLP and as such it enhances the chances of, though not assures, the determination of band gap. Since the availability of monochromators attached to commercial TEMs, determining band gaps in a TEM has become an interesting experimental option, especially for nanostructures which can be individually probed using STEM mode.

In addition to the band gap, the VEELS contains information about the dielectric function. When the VEEL spectrum is acquired with collection angles of the order of a few μrad, it is possible to obtain the dielectric function from the VEEL spectrum by employing Kramers Kronig analysis. The most dominant feature in the VEEL spectrum is the plasmon excitation. The scattering cross section for plasmon excitation can be used to find out the thickness of the area investigated or determine the chemical phase present.

The second important type of EELS signal studied is the core-loss EELS. The core-loss EELS provides information about the composition of the material. The core loss EELS contains the core-loss edges, which upon comparison with literature allow for determining the elements present. In addition, the scattering cross section of particular edges in the core-loss EELS can be analyzed to determine the approximate chemical composition of the material.

When a particular core-loss edge is studied in detail, with low spectrometer dispersion, it is possible to ascertain the fine-structure of the particular core-loss edge. This fine structure

helps in identifying the bonding type. For example, on the basis of the C-K edge analysis, it is possible to determine the % sp$^2$ versus % sp$^3$ character in a sample. In addition, it is possible to study the coordination chemistry of transition metals with the help of core-loss EELS.

## 2.4 Density Functional Theory

For calculating the properties of materials, DFT has over past few decades developed as a reliable computational tool. Progress in the field was pioneered by Hohenberg, Kohn and Sham whose theorems [44,45] illustrated the possibilities and advantages of dealing with electron densities instead of many-body wave functions and their applicability for solving the Schrödinger's equation. This section describes the central tenets of DFT and the various approximations involved.

This section is primarily based on the introductory text to the subject of DFT by Stefaan Cottenier [46].

2.4.1 Schrödinger's equation for a solid

A solid is constituted by heavy positively charged nuclei and relatively lighter negatively charged electrons. If the solid consists of N nuclei, it implies that the number of particles to be taken into consideration is N+ZN, where Z is the average atomic number of the solid. The Hamiltonian of the solid is described in Equation 2.21 where $M_i$ is the mass of the $i$th nuclei, $\vec{R_i}$ the radius vector of the $i$th nuclei, $m_e$ mass of electrons, $\vec{r_i}$ position vector of $i$th the electron, $Z_i$ atomic number of the $i$th nucleus and $\epsilon_0$ the permittivity of free space.

$$\hat{H} = -\frac{\hbar^2}{2}\sum_i \frac{\nabla^2_{\vec{R_i}}}{M_i} - \frac{\hbar^2}{2}\sum_i \frac{\nabla^2_{\vec{r_i}}}{m_e} - \frac{1}{4\pi\epsilon_0}\sum_{i,j} \frac{e^2 Z_i}{|\vec{R_i} - \vec{r_j}|} + \frac{1}{8\pi\epsilon_0}\sum_{i\neq j} \frac{e^2}{|\vec{r_i} - \vec{r_j}|} + \frac{1}{8\pi\epsilon_0}\sum_{i\neq j} \frac{e^2 Z_i Z_j}{|\vec{R_i} - \vec{R_j}|}$$

(2.21)

The first term on the right hand side (RHS) of Equation 2.21 is the kinetic energy of the nuclei, the second term the kinetic energy of the electrons. The third term represents the potential energy due to the electron nuclei interactions. The fourth term represents potential energy due to the electron-electron interactions while the fifth term lists the potential energy due to the nucleus-nucleus interactions.

In a solid, as the nuclei are effectively fixed to their positions (and possess only limited vibrational motion) the fifth term would be a constant. The nuclei are a lot heavier than the

electrons. When the nuclei move, the electrons due to the huge mass difference involved effectively adjust accordingly instantaneously; hence the nuclei can for practical purposes be assumed to be fixed and the first term in Equation 2.21 can be neglected. This approximation is known as the Born-Oppenheimer approximation and was first proposed by Born and Oppenheimer in 1927 [47]. The electrons being the preponderating player in the Equation 2.21, the potential due to the interaction of the electrons with the nuclei is referred to as external potential $V_{ext}$. This potential is treated as an external feature for the many-electron system.

2.4.2 Theorems of Hohenberg and Kohn

In their seminal paper published in 1964 [44] Hohenberg and Kohn laid the foundation of the density functional theory. They showed [44] that there exists a one-to-one correspondence between the ground state density of a many electron system and the external potential $V_{ext}$ [46]. A direct corollary of the above theorem is that the ground state expectation value of any observable is a unique functional of the ground state electron density [46]. This showed that the electron density contains as much information as the many body wavefunctions [46]; hence instead of dealing with many body wavefunctions, it is possible to rather deal with the electron density. In their second theorem Hohenberg and Kohn showed [44] that the ground-state total energy functional $H[\rho] \equiv E_{V_{ext}}[\rho]$ is of the form given by Equation 2.22 [46] where $\rho$ is the electron density.

$$E_{V_{ext}}[\rho] = F_{HK}[\rho] + \int \rho(\vec{r}) V_{ext}(\vec{r}) d\vec{r}$$
(2.22)

In Equation 1.22 $F_{HK}[\rho]$ is the universal Hohenberg-Kohn density functional for any many electron system. Kohn and Sham further built upon this knowledge by creating a mathematically feasible framework for solving the Hamiltonian [45]. They showed that using the Hohenberg-Kohn Theorem for finding the electron density, the Hamiltonian can be interpreted as the energy functional of a non-interacting classical electron gas subject to two potentials, one due to nuclei and the other due to the exchange and correlation effects [46]. The Kohn-Sham Hamiltonian is described in Equation 2.23.

$$\hat{H}_{KS} = -\frac{\hbar^2}{2m_e} \vec{\nabla}_i^2 + \frac{e^2}{4\pi\epsilon_0} \int \frac{\rho(\vec{r}')}{|\vec{r}-\vec{r}'|} + V_{xc} + V_{ext}$$
(2.23)

The third term in Equation 2.23 $V_{xc}$ contains the potential due to exchange correlation effects. The second term in Equation 2.23 is known as the Hartree operator $V_H$. The ground state

density $\rho(\vec{r})$ of the $N$ electron system can be described as given in Equation 2.24 where $\varphi_i(\vec{r})$ is the single particle wave function.

$$\rho(\vec{r}) = \sum_{i=1}^{N} \varphi_i^*(\vec{r}) \, \varphi_i(\vec{r}) \tag{2.24}$$

The single particle picture used above is based on the approximation that the system can be described as a collection of classical ions and essentially single quantum mechanical particles that reproduce the behavior of the electrons [48].

The Hartree operator $V_H$ and the exchange correlation operator $V_{xc}$ are dependent on the density $\rho(\vec{r})$ which is dependent on the $\varphi_i$ which are being searched [46]. This implies the nature of the problem is that of self-consistency. The way to go around it is to assume an initial density, solve the Kohn-Sham Hamiltonian and from the eigenvalues generated a new density is obtained. When this iteration process leads to a difference between the two densities before and after an iteration below a particular level, the calculation is assumed converged.

A particularly tricky part in this calculation is the incorporation of exchange correlation effects. A number of approximate methods exist. Generalized gradient approximation (GGA) has been successfully demonstrated to be an effective method for calculating the ground state properties [49].

2.4.3 APW+lo method

For solving the Kohn-Sham Hamiltonian an essential part is defining the electron density. The electron density can be defined in terms of various sets of basis vectors. The choice of basis vectors is critical as it should be small, such that less computational power is required, at the same time it should not be biased, such that it is not inclined to favor particular sort of solutions. A number of methods exist for defining the basis vectors, one of the most important being the augmented plane waves + local orbitals (APW+lo) approach.

In the APW+lo approach the space is divided into muffin-tin radii located concentric with the atomic nuclei. The electrons inside these muffin-tin radii are described by atomic wavefunctions. In the interstitial region a plane wave basis set is used to describe the electron density [46].

The basis function in the APW+lo method has two types of functions. The first kind are augmented plane waves linked to fixed energy levels $E_{1,l}^{\alpha}$ [46] as described in Equation 2.25

where $In$ represents the interstitial region, $u_l^\alpha$ solution to the radial part of Schrödinger's equation for atom $\alpha$, $Y_m^l$ the spherical harmonics, $V$ the volume and $S_\alpha$ the muffin-tin region.

$$\varphi_{\vec{K}}^{\vec{k}}(\vec{r}) = \begin{cases} \frac{1}{\sqrt{V}}\, e^{i(\vec{k}+\vec{K}).\vec{r}} & \vec{r} \in In \\ \sum_{l,m} A_{lm}^{\alpha,\vec{k}+\vec{K}} u_l^\alpha(r', E_{1,l}^\alpha) Y_m^l(\hat{r}') & \vec{r} \in S_\alpha \end{cases} \qquad (2.25)$$

The second type of function used is the local orbitals as described in Equation 2.26.

$$\varphi_{\alpha,lo}^{lm}(\vec{r}) = \begin{cases} 0 & \vec{r} \notin S_\alpha \\ [A_{lm}^{\alpha,lo} u_l^\alpha(r', E_{1,l}^\alpha) + B_{lm}^{\alpha,lo} u_l^\alpha(r', E_{1,l}^\alpha)] Y_m^l(\hat{r}') & \vec{r} \in S_\alpha \end{cases} \qquad (2.26)$$

The constants $A_{lm}^{\alpha,lo}$ and $B_{lm}^{\alpha,lo}$ are determined by normalization and applying boundary conditions requiring continuity at the boundaries of the muffin-tin sphere. A further improvement to this method is the usage of another set of local orbitals to describe the electrons from semi-core states. These local orbitals are described as shown in equation 2.27 where $u_l^\alpha$ is a radial function of normalization.

$$\varphi_{\alpha,LO}^{lm}(\vec{r}) = \begin{cases} 0 & \vec{r} \notin S_\alpha \\ [A_{lm}^{\alpha,LO} u_l^\alpha(r', E_{1,l}^\alpha) + C_{lm}^{\alpha,LO} u_l^\alpha(r', E_{2,l}^\alpha)] Y_m^l(\hat{r}') & \vec{r} \in S_\alpha \end{cases} \qquad (2.27)$$

### 2.4.4 Treatment of exchange correlation effects

The Kohn-Sham Hamiltonian (Equation 2.23) is exact barring the Born-Oppenheimer approximation [46]. Solving it however requires knowledge of the contribution of exchange-correlation effects [46]. The exchange energy is contributed in the single particle picture by the virtue of the property that if two electrons of same spin interchange positions, the sign of the many-body wave function should be inverted [48]. The correlation property relates to the fact that each electron is affected by the motion of every other electron [48].

The exchange correlation energy as a functional of the electron spin densities must be approximated for solving the Kohn-Sham Hamiltonian [49]. Two popular methods exist for this. The first being the local density approximation (LDA) and the second being generalized gradient approximation.

The LDA methodology calculates the exchange correlation energy by dividing the space into infinitesimally small volumes with constant density [46]. The plus point of this methodology is that it is unambiguous and requires no selection of parameters [46]. On the contrary it does not perform well for highly variant electron densities [46].

The second method (GGA) improves upon by calculating the exchange correlation energy due to an infinitesimally small element by making it dependent on not only the local density in that volume but also the density in the neighboring volumes [46]. There is no universal GGA and as such these contributions can be calculated in a number of ways. The most popular GGA methodology is that proposed by Perdew, Burke and Ernzerhof (PBE-GGA)[49].

2.4.5 Band gap problem

DFT based methods perform exceedingly well in describing the ground state properties, for example crystal structures, bulk moduli and phase diagrams to name a few [48,50]. However, DFT fails to correctly predict properties relating to the excited states, for example band gap [51,52]. The theorems of Hohenberg and Kohn [32] are mathematically valid only for ground states [53] thereby handling of excited states, like the conduction band states, within the framework is not accurate.

Tran and Blaha [54] have proposed an alternate methodology (TB-mBJ) by modifying the methodology proposed by Becke and Johnson [55] which has turned out to be very helpful in determining band gaps of semiconductors [54,56-58]. Becke and Johnson had proposed "exact-exchange" optimized effective potential in atoms [55]. TB-mBJ methodology modifies this potential [55] by adding a weighing element determined by the ratio of the gradient of density with the density ($\nabla\rho/\rho$) and has been used with much success [54,56-58].

# 2.5 Chapter references

[1]     D. J. Griffiths. *Introduction to quantum mechanics.* Pearson Education Inc. NJ (2005)

[2]     N. W. Ashcroft and N. D. Mermin. *Solid state physics.* Brooks Cole, KY (1976)

[3]     Mark Fox. *Optical properties of solids.* Oxford University Press, Oxford UK (2010)

[4]     D. Bohm and D. Pines. A collective description of electron interactions. I Magnetic interactions. *Phys. Rev.* 82, 625 (1951)

[5]     I. Kuzmanovski, S. Dimitrova-Lazova, and S. Aleksovska. Classification of perovskites with self-organizing maps. *Analytica Chemica Acta* 595, 182 (2007)

[6]     A. M. Glazer. The classification of tilted octahedra in perovskites. *Acta Cryst.* B28, 3384 (1972)

[7] F. S. Galasso. *Properties and preparation of perovskite-type compounds*. Pergamon Press, Oxford (1969)

[8] W. Jauch and A. Palmer. Anamolous zero-point motion in $SrTiO_3$: results from $\gamma$-ray diffraction. *Phys. Rev. B.* 60, 2961 (1999)

[9] M. Dion, M. Ganne, and M. Tournoux. Nouvelle familles de phases $M^I M^{II}_2 Nb_3 O_{10}$ a feuillets "perosvkite". *Mat. Res. Bull.* 16, 1429 (1981)

[10] A. J. Jacobson, J. W. Johnson, and J. T. Lewandowski. Interlayer chemistry between thick transition-metal oxide layers: Synthesis and intercalation reactions of $K[Ca_2 Na_{n-3} Nb_n O_{3n+1}]$ ($3 \leq n \leq 7$). *Inorg. Chem.* 24, 3727 (1985)

[11] F. Lichtenberg, A. Herrenberg, and K. Wiedenmann. Synthesis, structural, magnetic and transport properties of layered perovskite-related titanates, niobates and tantalates of the type $A_n B_n O_{3n+2}$, $A' A_{k-1} B_k O_{3k+1}$ and $A_m B_{m-1} O_{3m}$. *Prog. Sol. State Chem.* 36, 253 (2008)

[12] H. Fukuoka, T. Isami, and S. Yamanaka. Crystal structure of a layered perovskite niobate $KCa_2 Nb_3 O_{10}$. *J. Sol. State Chem.* 151, 40 (2000)

[13] T. Tokumitsu, K. Toda, T. Aoyagi, D. Sakuraba, K. Uematsu, and M. Sato. Powder neutron diffraction study of layered perovskite $KCa_2 Nb_3 O_{10}$. *J. Cer. Soc. Jap.* 114, 795 (2006)

[14] N. Ishizawa, R. Yamashita, S. Oishi, J. R. Hester, S. Kishimoto. Synchrotron x-ray study of triclinic $LiCa_2 Nb_3 O_{10}$ with perovskite type slabs. *Acta Cryst. C.* 57, 1006 (2001)

[15] S.-H. Byeon, H. J. Kim, D.-K. Kim, N. H. Hur. Synthesis, structure, magnetic properties and XANES spectra of reduced niobate $RbNa_x Ca_2 Nb_3 O_{10}$. *Chem. Mater.* 15, 383 (2003)

[16] M. Dion, M. Ganne, and M. Tournoux. Structure cristalline de la perovskite feuilletee ferroelastique $CsCa_2 Nb_3 O_{10}$. *Rev. Chimie Minerale* 21, 92 (1984)

[17] Z. Liang, K. Tang, Q. Chen, H. Zheng. $RbCa_2 Nb_3 O_{10}$ from X-ray powder data. *Acta Cryst. E.* 65, 44 (2009)

[18] V. Thangadurai and W. Weppner. AÁ$_2$M$_3$O$_{10}$ (A=K, Rb, Cs; A'=Ca; M=Nb) layered perovskites: low temperature proton conductors in hydrogen atmospheres. *J. Mat. Chem.* 11, 636 (2001)

[19] K. Domen, J. Yoshimura, T. Sekine, A. Tanaka, and T. Onishi. A novel series of photocatalysts with ion-exchangeable layered structure of niobate. *Cat. Lett.* 4, 339 (1990)

[20] H. Fukuoka, T. Isami, and S. Yamanaka. Superconductivity of alkali metal intercalated niobate with perovskite structure. *Chem. Lett.* 26, 703 (1997)

[21] M. A. Bizeto, V. R. L. Constantino, and H. F. Brito. Luminescence properties of layered niobate KCa$_2$Nb$_3$O$_{10}$ doped with Eu$^{3+}$ and La$^{3+}$ ions. *J. Alloys Comp.* 311, 159 (2000)

[22] K. Akatsuka, G. Takanashi, Y. Ebina, M. Haga, and T. Sasaki. Electronic band structure of exfoliated titanium and/or niobium based oxide nanosheets probed by electrochemical and photoelectrochemical measurements. *J. Phys. Chem. C.* 116, 12426 (2012)

[23] P. Ganter. Synthesis and Characterization of Ca$_2$Nb$_3$O$_{10}^-$ nanosheets and their assembly with layered double hydroxides. *Bachelors Thesis, Department of Chemistry, Ludwig-Maximilians-Universität München* (2012)

[24] K. S. Novoselov, A. K. Geim, S. V. Morozov, D. Jiang, Y. Zhang, S. V. Dubonos, I. V. Grigorieva, and A. A. Firsov. Electric field effect in atomically thin carbon films. *Science* 306, 666 (2004)

[25] R. Ma and T. Sasaki. Nanosheets of oxides and hydroxides: Ultimate 2D charge bearing crystallites. *Adv. Mat.* 22, 5082 (2010)

[26] J. N. Coleman, M. Lotaya, A. O'Neill, S. D. Bergin, P. J. King, U. Khan, K. Young, A. Gaucher, S. De, R. J. Smith, I. V. Shvets, S. K. Arora, G. Stanton, H-Y. Kim, K. Lee, G. T. Kim, G. S. Duesberg, T. Hallam, J. J. Boland, J. J. Wang, J. F. Donegan, J. C. Grunlan, G. Moriarty, A. Shmeliob, R. J. Nicholls, J. M. Perkins, E. M. Grieveson, K. Theuwissen, D. W. McComb, P. D. Nellhist, and V. Nicolosi. Two-dimensional nanosheets produced by liquid exfoliation of layered materials. *Science* 331, 568 (2011)

[27] K. S. Novoselov, D. Jiang, F. Schedin, T. J. Booth, V. V. Khotkevich, S. V. Morozov, and A. K. Geim. Two-dimensional atomic crystals. *PNAS* 102, 10451 (2005)

[28] R. J. Smith, P. J. King, M. Lotaya, C. Wirtz, U. Khan, S. De, A. O'Neill, G. S. Duesberg, J. C. Grunlan, G. Moriaty, J. Chen, J. Wang, A. I. Minett, V. Nicolosi, and J. N. Coleman. Large-scale exfoliation of inorganic layered compounds in aqueous surfactant solutions. *Adv. Mater.* 23, 3944 (2011)

[29] R. E. Schaak and T. E. Mallouk. Self-assembly of tiled perovskite monolayer and multilayer films. *Chem. Mater.* 12, 2513 (2000)

[30] Y. Ebina, T. Sasaki, and M. Watanabe. Study on exfoliation of layered perovskite-type niobates. *Solid State Ionics* 151, 177 (2002)

[31] M. M. J. Treacy, S. B. Rice, A. J. Jacobson, and J. T. Lewandowski. Electron microscopy study of delamination in dispersions of perovskite-related phases $K[Ca_2Na_{n-3}Nb_nO_{3n+1}]$: Evidence for single layer formation. *Chem. Mater.* 2, 279 (1990)

[32] B.-W. Li, M. Osada, T. C. Ozawa, Y. Ebina, K. Akatsuka, R. Ma, H. Funakubo, and T. Sasaki. Engineered interfaces of artificial perovskite oxide superlattices via nanosheet deposition process. *ACS Nano* 4, 6673 (2010)

[33] M. Osada and T. Sasaki. Two-dimensional dielectric nanosheets: Novel nanoelectronics from nanocrystal building blocks. *Adv. Mater.* 24, 210 (2012)

[34] O. C. Compton, E. C. Carroll, J. Y. Kim, D. S. Larsen, F. E. Osterloh. Calcium niobate semiconductor nanosheets as catalyst for photochemical hydrogen evolution from water. *J. Phys. Chem. Lett. C.* 111, 14589 (2007)

[35] L. Chang, M. A. Holmes, M. Waller, F. E. Osterloh, and A. J. Moule. Calcium niobate nanosheets as novel electron transport material for solution-processed multi-junction polymer solar cells. *J. Mat. Chem.* 22, 20443 (2012)

[36] D. B. Williams, C. B. Carter. *Transmission electron microscopy, A textbook for Materials Science, Third edition*. Springer Science + Business Media LLC (2009)

[37] R. F. Egerton. *Electron Energy-Loss Spectroscopy in the Electron Microscope*. Springer Science + Business Media Inc. (2011)

[38]    M. Knoll and E. Ruska. Das Elektronenmikroskop. *Z. Phys.* 78, 318 (1932)

[39]    R. H. Fowler and L. Nordheim. Electron emission in intense electric fields. *Proc. R. Soc. Lond. A* 119, 173 (1928)

[40]    C. von Festenberg. Retardierungseffekte in Energieverlustspektrum von GaP. *Z. Phys.* 214, 464 (1968)

[41]    C. von Festenberg. Energieverlustmessungen an III-V-Verbindungen. *Z. Phys.* 227, 453 (1969)

[42]    L. Gu, V. Srot, W. Sigle, C. Koch, P. van Aken, F. Scholz, S. B. Thapa, C. Kirchner, M. Jetter, and M. Rühle. Band-gap measurements of direct and indirect semiconductors using monochromated electrons. *Phys. Rev. B.*, 75, 195214 (2007)

[43]    C. Scheu. Analytische Untersuchungen an $Cu/Al_2O_3$- und $Cu/Ti/Al_2O_3$- Grenzflächen. Doctoral Dissertation, *University of Stuttgart* (1996).

[44]    P. Hohenberg and W. Kohn. Inhomogenous electron gas. *Phys. Rev.* 136, B864 (1964)

[45]    W. Kohn and L. J. Sham. Self-consistent equations including exchange and correlation effects. *Phys. Rev.* 140, A1133 (1965)

[46]    S. Cottenier. *Density functional theory and the family of (L)APW-methods: a step by step introduction.* Katholieke Universiteit Leuven (2002) ISBN 90-807215-1-4

[47]    M. Born and R. Oppenheimer. Zur Quantentheorie der Molekeln. *Annal. Phys.* 84, 457 (1927)

[48]    E. Kaxiras. *Atomic and electronic structure of solids.* Cambridge University Press, Cambridge UK (2003)

[49]    J. P. Perdew, K. Burke, and M. Ernzerhof. Generealized Gradient Approximation made simple. *Phys. Rev. Lett.*, 77, 3865 (1996)

[50]    J. Hafner. Atomic-scale computational material science. *Acta. Mater.* 48, 71 (2000)

[51]    A. Seidl, A. Görling, P. Vogl, J. A. Majewski, and M. Levy. Generalized Kohn-Sham schemes and the band-gap problem. *Phys. Rev. B.* 53, 3764 (1996)

[52]   W. Ku and A. G. Eguiluz. Band-gap problem in semiconductors revisited: effects of core states and many-body self-consistency. *Phys. Rev. Lett.* 89, 126401 (2002)

[53]   A. S. Bamzai and B. M. Deb. The role of single particle densities in chemistry. *Rev. Mod. Phys.* 53, 95 (1981)

[54]   F. Tran and P. Blaha. Accurate band gaps of semiconductors and insulators with a semilocal exchange correlation potential. *Phys. Rev. Lett.* 102, 226401 (2009)

[55]   A. D. Becke and E. R. Johnson. A simple effective potential for exchange. *J. Chem. Phys.* 124, 221101 (2006)

[56]   D. J. Singh, S. S. A. Seo, and H. N. Lee. Optical properties of ferroelectric $Bi_4Ti_3O_{12}$. *Phys. Rev. B.* 82, 180103R (2010)

[57]   W. Feng, D. Xiao, J. Ding, and Y. Yao. Three dimensional topological insulators in I-III-$VI_2$ and II-IV-$V_2$ chalcopyrite semiconductors. *Phys. Rev. Lett.* 106, 016402 (2011)

[58]   D. Koller, F. Tran, and P. Blaha. Merits and limits of the modified Becke-Johnson exchange potential. *Phys. Rev. B.* 83, 195134 (2011)

# 3 Density functional theory based calculations on bulk KCa$_2$Nb$_3$O$_{10}$

DFT has proved to be an extremely useful tool for understanding the properties of solids [1,2]. This section entails the DFT calculations performed on KCa$_2$Nb$_3$O$_{10}$. An augmented plane wave and local orbital (APW+lo) approach, as incorporated in the commercial WIEN2k software code [3] was used. The results presented in this chapter are based on a manuscript, "Electronic structure of KCa$_2$Nb$_3$O$_{10}$ as envisaged by density functional theory and valence electron energy loss spectroscopy" currently under review at the Physical Review B.

## 3.1 Computational details

The crystal structure as proposed by Tokumitsu and co-workers was used for performing the calculations [4]. The crystal axes were reoriented to define crystal parameters $a$, $b$, $c$ and $\gamma$ as 14.859 Å, 7.7418 Å, 7.7073 Å, and 97.51° respectively. The corresponding crystal structure is illustrated in Figure 3.1. The structure has overall 23 inequivalent atoms and the unit cell contains 4 formula units. The Nb atoms in the median (200) crystallographic plane shall be referred to as Nb1, Nb2 whereas the Nb atoms in between Ca and K layers as Nb3, Nb4.
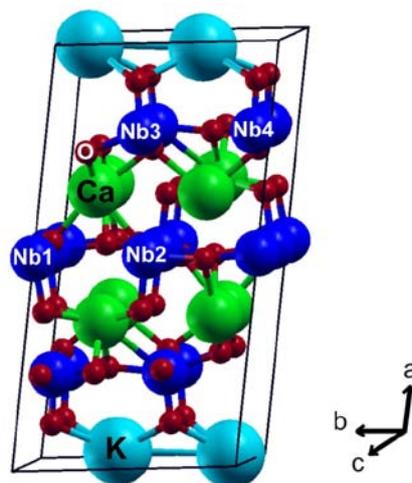


Figure 3.1: The crystal structure of KCa$_2$Nb$_3$O$_{10}$ contains parallel planes of K, Ca and Nb in addition to oxygen atoms.

The atomic spheres (muffin-tin radii) sizes used for K, Ca, Nb, and O were 2.42, 2.03, 1.69 and 1.50 atomic units (a.u.) respectively. Atomic wavefunctions in the muffin-tin spheres were expanded up to angular momentum $l=10$. Semi-core states (Ca - 3s, 3p; K - 3s, 3p; Nb - 4s, 4p; O - 2s) were expanded using local orbitals. The size of the basis set for the plane wave expansion used in the interstitial region was governed by fixing the parameter $R_{MT}K_{max} = 7$ where $R_{MT}$ is the smallest *muffin-tin* radius and $K_{max}$ is largest plane wave used in expansion. To cross-check the adequacy of the plane wave basis used calculations were performed on the geometry optimized structure. The individual force components on all atoms were within 5 mRy/a.u. thereby justifying the choice of parameters used. For geometry optimization of the structure, exchange-correlation effects were treated according to the generalized gradient approximation as proposed by Perdew, Burke and Ernzerhof (PBE-GGA) [5]. To determine the electronic properties, namely the density of states (DOS), bandstructure, dielectric function and the loss function, Tran-Blaha modified Becke Johnson Potential [6] was used for treating the exchange correlation effects. The irreducible Brillouin zone was sampled with a [4x4x2] *k*-mesh for performing self-consistency cycles. The self-consistency cycle was assumed to be finished when the force components on the individual atoms fell below 5.0 mRy/a.u. Subsequently for obtaining the DOS and the bandstructure a denser *k*-mesh of [8x8x4] *k*-points was used for sampling the irreducible Brillouin zone. Optical properties (dielectric function) were calculated using the OPTIC program [7] of the WIEN2k package which was executed by computing the momentum transfer matrix elements in the energy range -5 and 5 Ry. Two different methodologies were used for ascertaining the dielectric function. For the low energy region $E<25$ eV no scissor operator was applied for computing the dielectric function. However for determining the dielectric function in higher energy range (*25* eV$<E<50$ eV) the transitions were shifted by an amount $\Delta E=2.5$ eV towards higher energies.

## 3.2 Structure optimization

Experimentally determined structures are generally very accurate with regards to unit cell parameters and symmetry of the structure. Despite that, in crystals with complex unit cells relative positions could be further refined using *ab-initio* methods. DFT has been widely used for optimizing the crystal structures. A number of ways exist to optimize the crystal structure [3], for example relaxing the unit cell parameters; allowing structure to relax along a particular axis; minimizing the total energy; minimizing the forces on individual atoms. Given the fact that this study, concerns the electronic structure and not with mechanical properties

like bulk modulus (for whose determination unit cell parameters need to be relaxed), we optimize the structure by minimizing the overall force components. Using PBE-GGA potentials for describing the exchange correlation effects, the structure of $KCa_2Nb_3O_{10}$ was optimized such that overall the force components on individual atoms converged to values below 5 mRy/a.u. The structures before (labeled initial) and after (labeled final) geometry optimization, when viewed parallel to the crystallographic *b* axis are shown in Figure 3.2.
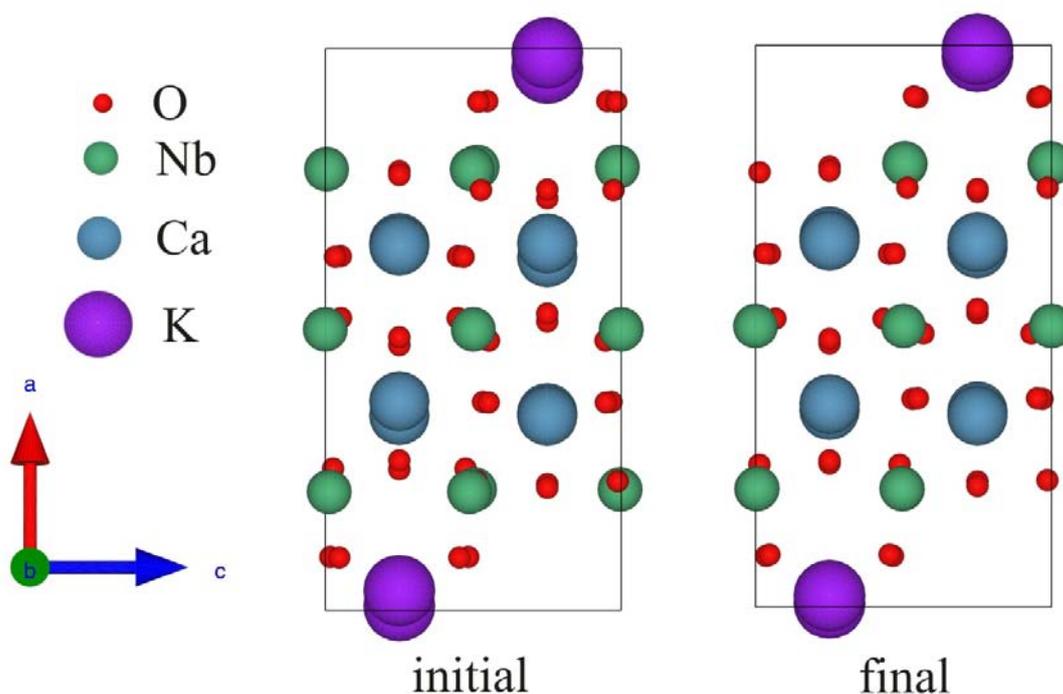


Figure 3.2: The crystal structure of $KCa_2Nb_3O_{10}$ before and after geometry optimization labeled as initial and final respectively.

Geometry optimization of the $KCa_2Nb_3O_{10}$ structure changed the fractional atomic positions (Table 3.1) by 0.033 Å for Ca3 as compared to the experimental structure [4]. The Nb-O distances varied less than 0.02 Å for Nb1 and Nb2 thereby leading to minimal changes to the Nb1(2)-O octahedra. On the other hand the Nb-O distances of Nb3 and Nb4 changed up to 0.07 Å for the Nb3(4)-O octahedra which rotate slightly. These rotations and the large movements of the Ca ions lead to changes in some Ca-O bond lengths by up to 0.3 Å. Overall these large changes around Ca lead to change in the bond valence sums from 2.44-1.90-1.65-2.34 to 2.33-2.16-1.81-2.02 (Ca1-Ca2-Ca3-Ca4) thereby making them much closer to the formal valence of Ca (+2). K1-O2-K2 distances become much more similar as some K-O distances change up to 0.2 Å. Overall the structure becomes flatter along the *bc* plane.

Table 3.1: Theoretically optimized (top) and experimental (bottom) fractional atomic positions in $KCa_2Nb_3O_{10}$.

| | | | |
|---|---|---|---|
| Ca 1 | 0.6495 | 0.7855 | 0.75 |
| | 0.653 | 0.78 | 0.75 |
| Ca 2 | 0.3405 | 0.7023 | 0.75 |
| | 0.346 | 0.717 | 0.75 |
| Ca 3 | 0.6384 | 0.2893 | 0.75 |
| | 0.628 | 0.322 | 0.75 |
| Ca 4 | 0.3480 | 0.1969 | 0.75 |
| | 0.351 | 0.201 | 0.75 |
| K 1 | 0.0203 | 0.6302 | 0.25 |
| | 0.035 | 0.616 | 0.25 |
| K 2 | 0.0071 | 0.1226 | 0.25 |
| | 0.008 | 0.132 | 0.25 |
| Nb 1 | 0.5 | 0 | 0 |
| | 0.5 | 0 | 0 |
| Nb 2 | 0.5 | 0.5 | 0 |
| | 0.5 | 0.5 | 0 |
| Nb 3 | 0.7900 | 0.5778 | 0.9960 |
| | 0.7848 | 0.571 | 0.004 |
| Nb 4 | 0.7889 | 0.0733 | 0.9943 |
| | 0.789 | 0.075 | 0.987 |
| O 1 | 0.6293 | 0.4998 | 0.0304 |
| | 0.629 | 0.495 | 0.033 |
| O 2 | 0.9091 | 0.6220 | 0.9644 |
| | 0.905 | 0.594 | 0.983 |
| O 3 | 0.7741 | 0.3211 | 0.0136 |
| | 0.77 | 0.316 | 0.012 |
| O 4 | 0.7444 | 0.5503 | 0.75 |
| | 0.749 | 0.541 | 0.75 |
| O 5 | 0.7764 | 0.5923 | 0.25 |
| | 0.775 | 0.574 | 0.25 |
| O 6 | 0.5226 | 0.5660 | 0.75 |
| | 0.514 | 0.576 | 0.75 |
| O 7 | 0.5131 | 0.7536 | 0.0673 |
| | 0.520 | 0.755 | 0.053 |
| O 8 | 0.6286 | 0.0635 | 0.0486 |
| | 0.630 | 0.006 | 0.052 |
| O 9 | 0.9067 | 0.0879 | 0.9530 |
| | 0.906 | 0.081 | 0.953 |
| O 10 | 0.7464 | 0.8139 | 0.9869 |
| | 0.748 | 0.818 | 0.974 |
| O 11 | 0.7389 | 0.0757 | 0.75 |
| | 0.733 | 0.065 | 0.75 |
| O 12 | 0.7842 | 0.0504 | 0.25 |
| | 0.782 | 0.069 | 0.25 |
| O 13 | 0.5309 | 0.9570 | 0.75 |
| | 0.528 | 0.973 | 0.75 |

## 3.3 Bandstructure

The bandstructure of a material represents the electron eigenstates in the reciprocal space. Conventional DFT based methods, PBE-GGA for example underestimate the band gaps [8,9]. This is because of the fact that the theorems of Kohn and Hohenberg are mathematically valid only for ground states (electron eigenstates below the Fermi energy) [10]. TB-mBJ potential [6] have been demonstrated to accurately determine the band gap values (and hence the positions of conduction band states) for various semiconductors and insulators [6]. Therefore, once the geometry was optimized using the PBE-GGA, electronic structure was calculated using the TB-mBJ potential. For bandstructure calculations a denser $k$-mesh of [8x8x4] $k$-points was used to sample the irreducible Brillouin zone. The calculated bandstructure along with the Brillouin zone is shown in Figure 3.3.
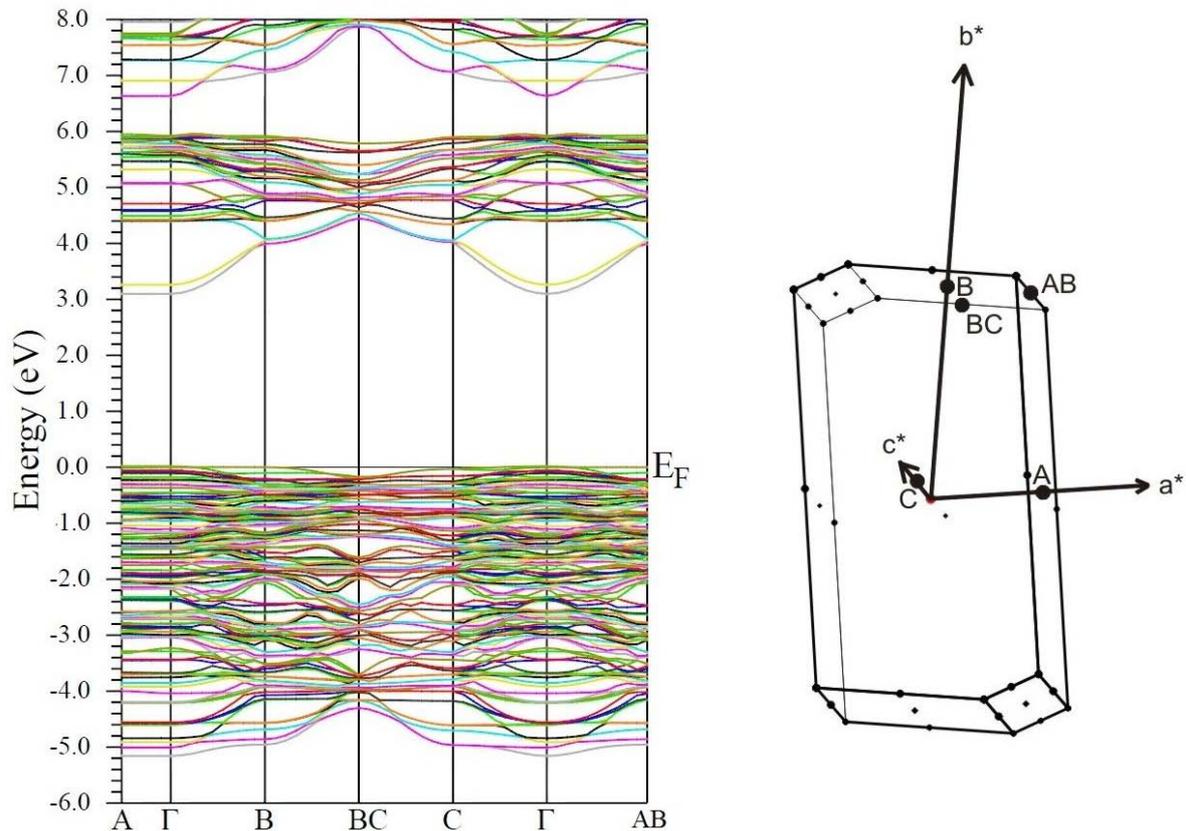


Figure 3.3: The bandstructure (left) and the Brillouin zone (right) of $KCa_2Nb_3O_{10}$. The Fermi energy (top of the valence band) is defined to be zero energy.

The bandstructure of $KCa_2Nb_3O_{10}$ illustrates it to be a direct band gap semiconductor with the top of the valence band and the bottom of conduction band lying at the $\Gamma$ point in the Brillouin

zone. The band gap of the $KCa_2Nb_3O_{10}$ is 3.1 eV. The valence band states have a high density close to the Fermi energy (-5 eV to 0 eV). The conduction band on the other hand has a very limited number of states close to the conduction band onset of 3.1 eV. In contrast, from 4 eV to 6 eV there exists a dense bunch of conduction band eigenstates. Moreover, the valence band states close to the Fermi energy are particularly flat whereas the conduction band states close to the band onset (3.1 eV to 4.0 eV) are energetically dispersed. Interestingly, all the states close to the Fermi energy, in valence and conduction bands, are particularly flat along the Γ-A direction in the reciprocal space (Fig 3.3).

## 3.4 Density of States

The density of states was determined using the TB-mBJ potentials [6]. The total and partial DOS are depicted in Figure 3.4. The total DOS reveals $KCa_2Nb_3O_{10}$ to be a wide band gap semiconductor with a band gap value of 3.1 eV.
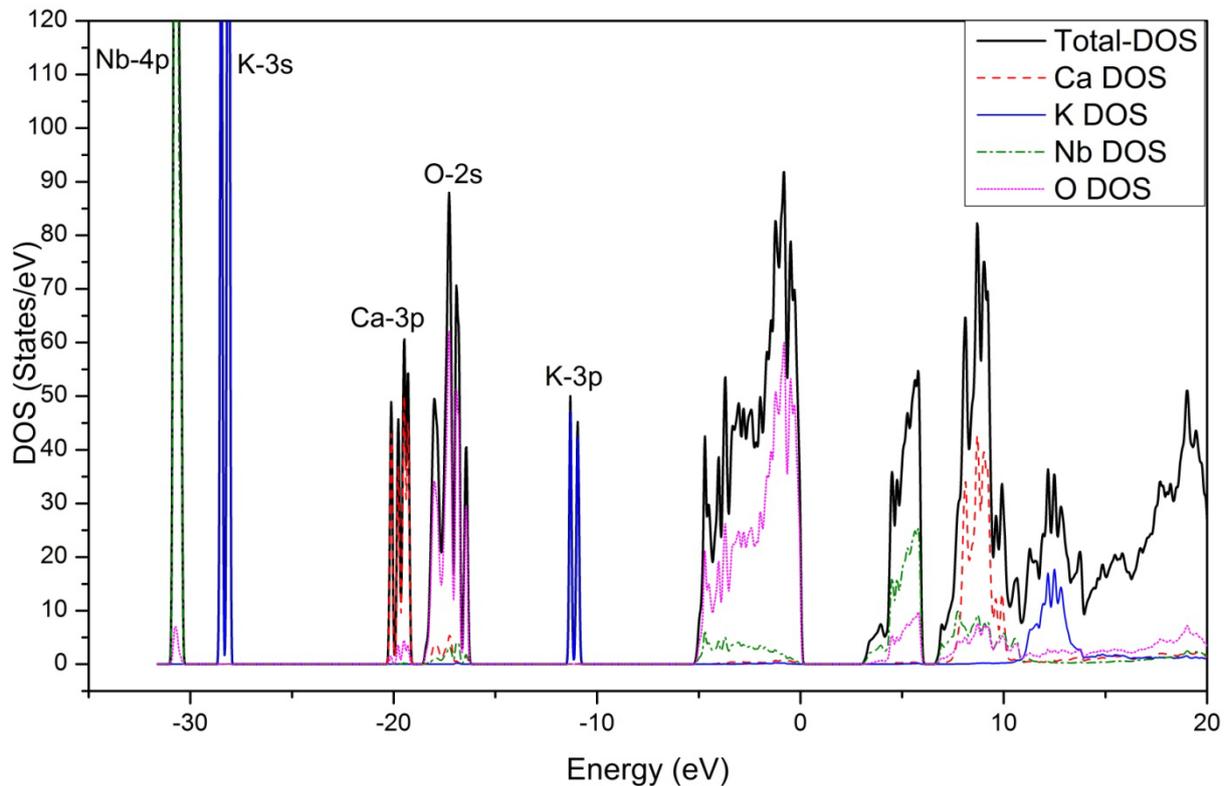


Figure 3.4: The total as well as partial Ca, K, Nb and O densities of states of $KCa_2Nb_3O_{10}$.

The partial DOS reveal semi-core states in the following energy domains Nb-4p -30.9 to -30.3 eV; K-3s -28.6 to -27.9 eV; Ca-3p -20.2 to -19.0 eV; O-2s -18.4 to -16.2 eV; and K-3p -11.3 to -10.8eV. In the valence and conduction bands an effective intermixing between various

46

atomic states is seen. The valence band comprises predominantly of O-2p states, in addition to a small number of Nb-3d states. The first conduction band (3.1 to 6.0 eV) on the contrary comprises of Nb-3d states primarily and to some extent O-2p states.

Given that the crystal structure of $KCa_2Nb_3O_{10}$ consists of two types of Nb positions (Nb1, Nb2 and Nb3, Nb4), it is worth investigating the contribution of these two types of Nb atomic positions to the DOS. The partial DOS contributions of Nb1,2 and Nb3,4 are illustrated in Figure 3.5 in the energy range -6 to 10 eV. It is evident that the two types of Nb atomic positions contribute very differently to the DOS. The conduction band onset at 3.1eV is contributed by the states of Nb1,2 i.e. the Nb atoms in the median plane (200) of the crystal.
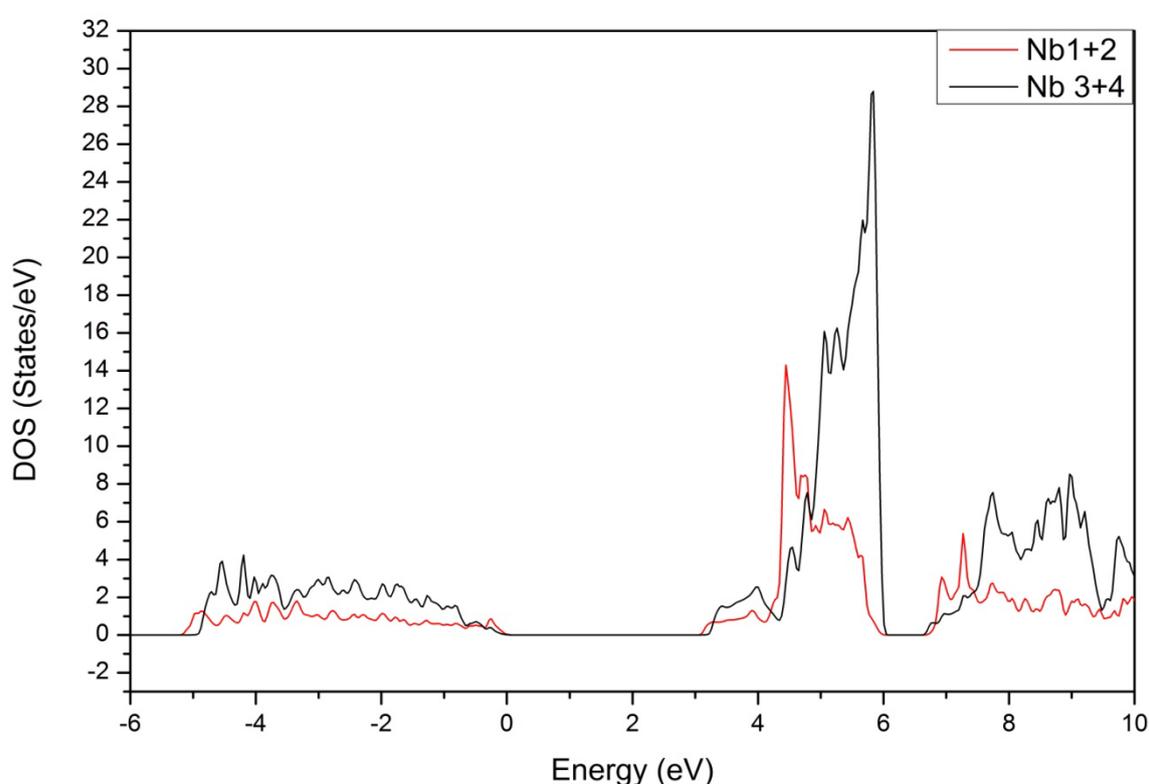


Figure 3.5: The partial DOS contributions of Nb1,2 and Nb3,4 atomic positions in the valence and conduction bands.

Furthermore, the partial DOS contributions of Nb-4d orbitals offer insight into the bonding character. To this end the partial DOS contributions of $t_{2g}$-like and $e_g$-like orbitals were investigated such that in local coordinates centered at each Nb atom the two Nb-4d orbitals pointing towards oxygen atoms were classified as $e_g$-like and the other three Nb-4d orbitals pointing in between the O atoms as $t_{2g}$-like. The partial DOS contributions of $t_{2g}$-like and $e_g$-like orbitals illustrated in Figure 3.6 show the Nb-4d states of $t_{2g}$-like symmetry to be

47

predominantly contributing to the lower conduction band whereas the $e_g$-like states contribute to the upper conduction band.
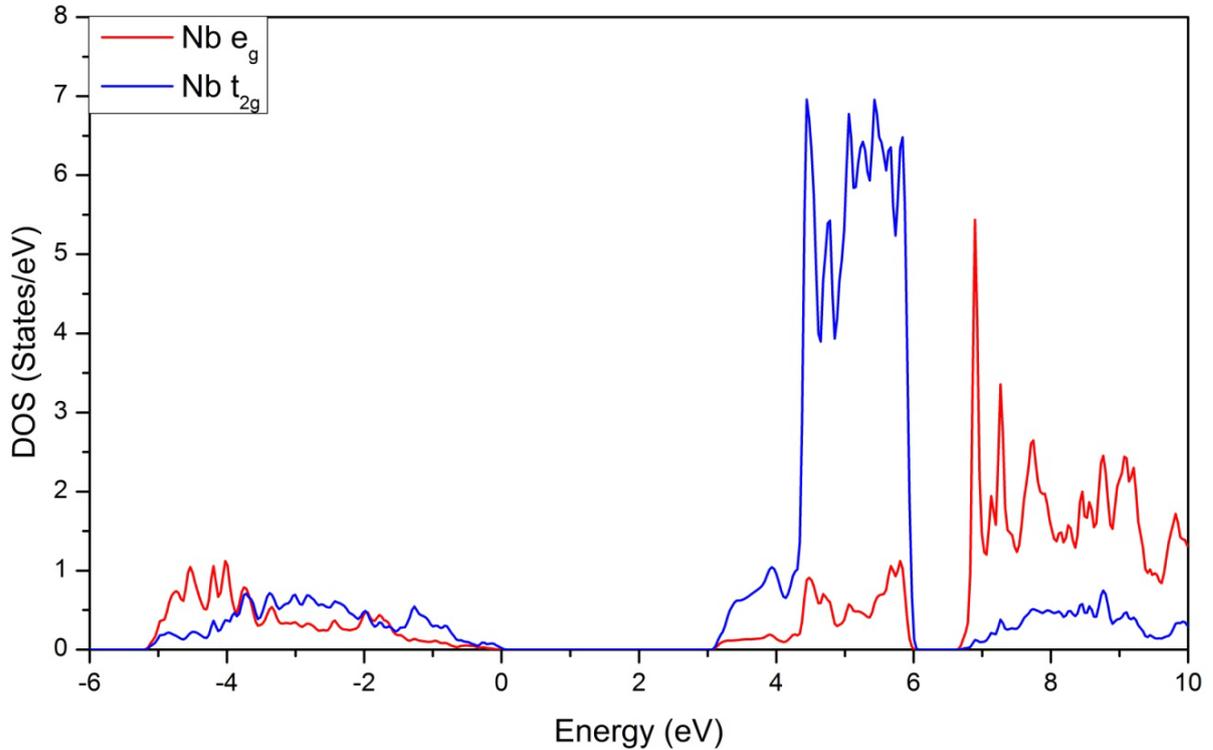


Figure 3.6: Partial DOS contributions of Nb-4d orbitals with $t_{2g}$ and $e_g$ character.

## 3.5 Dielectric function

Dielectric function is a complex tensor function of order 3x3. In the case of monoclinic crystals like $KCa_2Nb_3O_{10}$, it contains non-zero off-diagonal elements [7,11], however such (small) terms have been neglected in analysis. Average dielectric function was computed as the average of the three diagonal elements of the dielectric function tensor. The dielectric function of $KCa_2Nb_3O_{10}$ was computed from the electron densities generated using the OPTIC package [7] in WIEN2k [3]. The execution of this program computes the momentum transfer matrix elements between occupied and empty states which relate to the imaginary part of the dielectric function $\varepsilon_2$. The computed $\varepsilon_2$ , shown in Figure 3.7, indicates two broad transition bands with maxima at 6.1 and 9.0 eV. The first band in the energy range 4.5 and 7.0 eV delineates the transitions from the valence band to the Nb-$t_{2g}$-like bands with the maximum at 6.1 eV. The second band between 7.0 and 11.0 eV represents the transitions of valence electrons into Nb-$e_g$-like states. A comparison between the partial DOS (Figure 3.4) and the $\varepsilon_2$ (Figure 3.7) helps one in identifying the transitions due to semi-core states. The

excitation of K-3p electrons into K-3d states result in excitation shown in $\varepsilon_2$ at 23 eV (labeled in Fig 3.6 with K). Ca-3p electrons being promoted into Ca-3d states lead to a peak in $\varepsilon_2$ at 28 eV (labeled with Ca). Excitation of Nb-4p electrons are responsible for the transitions beginning at 35 eV (labeled with Nb).
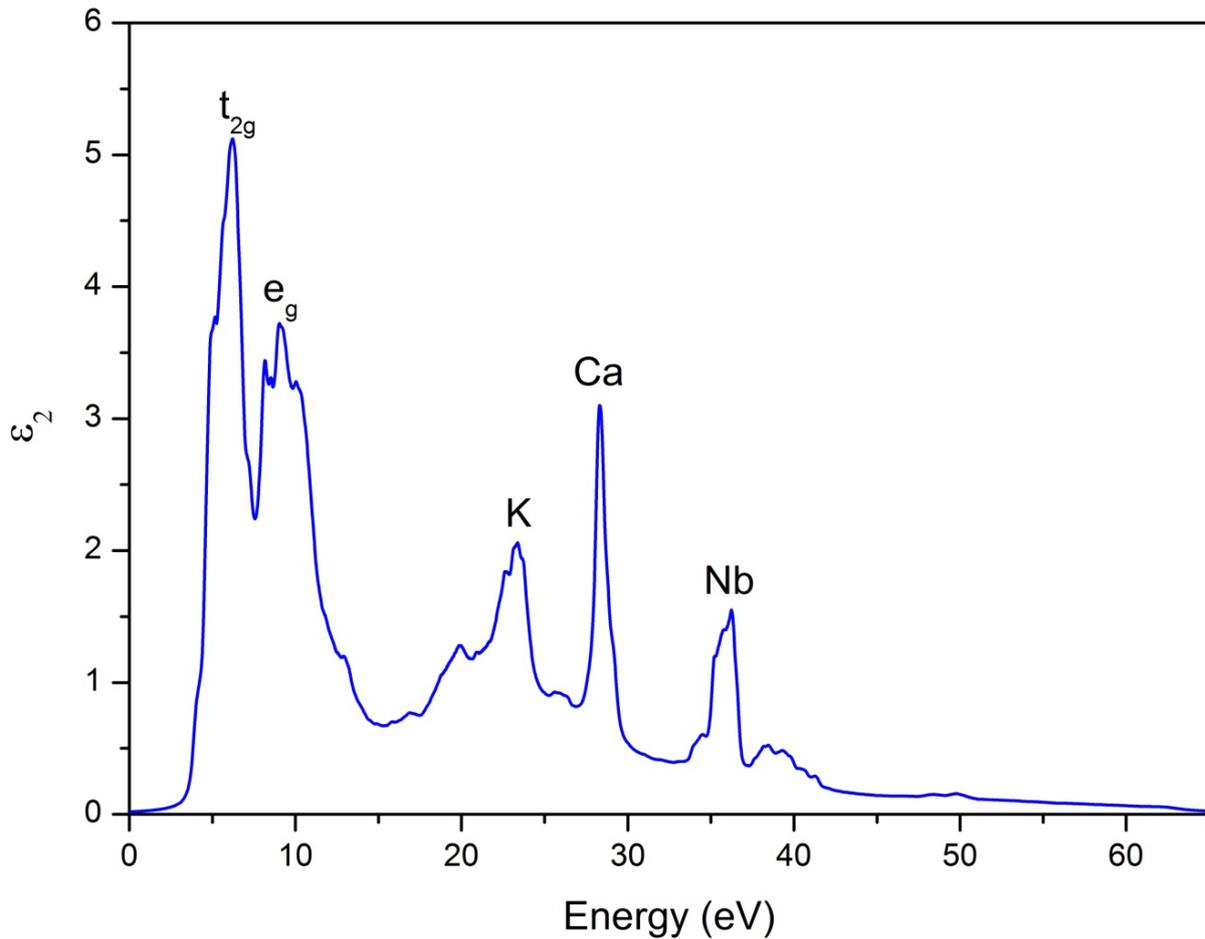


Figure 3.7: Computed $\varepsilon_2$ indicating the various electronic transitions in $KCa_2Nb_3O_{10}$.

The real part of the dielectric function $\varepsilon_1$ was computed from the imaginary part $\varepsilon_2$ by applying the Kramers Kronig transformation. The computed $\varepsilon_1$ is shown in Figure 3.8. The plasmon excitations can be identified as the points where $\varepsilon_1$ is zero and has a positive slope with respect to the energy axis [12,13]. Clearly, at three points $E_{p1}$ 11.3eV, $E_{p2}$ 30.0eV and $E_{p3}$ 37.0eV these conditions are satisfied indicating the existence of plasmon excitations at these energies. In addition, the value of $\varepsilon_1$ at high energies (frequencies) $\varepsilon_\infty$, also known as the high-frequency dielectric function, describes the dielectric response of the material under electromagnetic fields varying so fast that the material is not able to adjust the electron

densities in response, and hence responds by an overall temporally invariant dielectric response [14]. From Figure 3.8 the $\varepsilon_\infty$ for $KCa_2Nb_3O_{10}$ is determined to be 0.77.
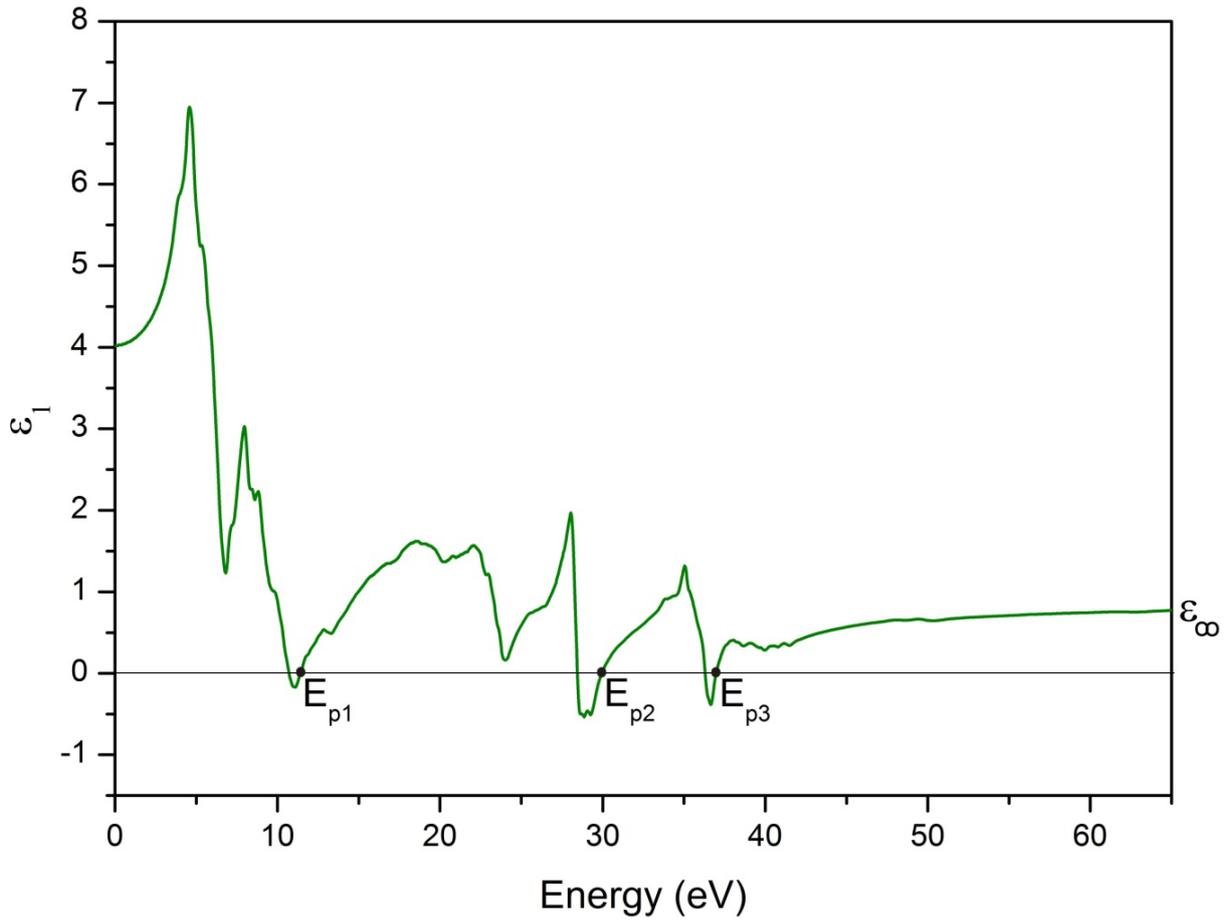


Figure 3.8: The real part of dielectric function $\varepsilon_1$ depicting the plasmon excitations $E_{p1}$, $E_{p2}$ and $E_{p3}$ and the high frequency dielectric constant $\varepsilon_\infty$.

The value of $\varepsilon_1$ at low frequencies $\varepsilon_0$ is defined as the dielectric response of the material under very slowly varying electromagnetic fields [12]. However, it would be incorrect to interpret the computed value of $\varepsilon_1$ at *E=0* eV (4.0) as $\varepsilon_0$ because in the computational methodology used, one computes the dielectric response of the material only with electronic transitions as the response mechanism. In general, the dielectric response of a material to an applied dynamic electric field depends upon a number of response mechanisms [15], like displacement polarization, atomic polarization, lattice vibrations, electronic excitations etc. At lower frequencies $<10^{13}$ Hz the polarization is dominated by mechanisms like displacement polarization, phonons etc. Events of such sorts are not taken into account while calculating the dielectric function in this methodology thereby interpreting value of $\varepsilon_1$ at *E=0* eV would be incorrect.

## 3.6 Loss Function

The loss function $S$ relates to the energy lost by a beam of fast electrons as it passes through a material [16]. The loss function is known to clearly depict the plasmon excitations [12]. After applying the Kramers Kronig transformation, the computed loss function $S$ is shown in Figure 3.9. The plasmon excitations $E_{p2}$ and $E_{p3}$ are clearly visible, however $E_{p1}$ is not discernible due to the single electron transitions around *E~11* eV overlapping.
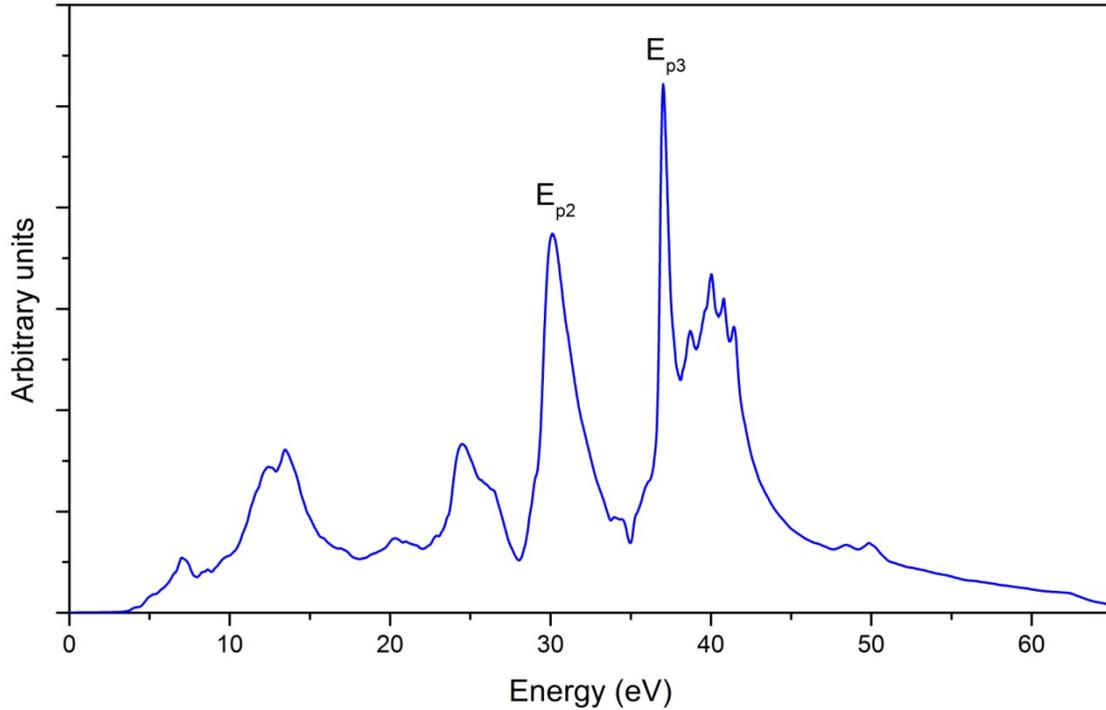


Figure 3.9: The computed loss function $S$ of $KCa_2Nb_3O_{10}$.

A comparison of the computed loss function $S$ (Figure 3.9) with the imaginary part of the dielectric function $\varepsilon_2$ (Figure 3.7) indicates the transitions occurring at energies 28 eV and 40eV to be due to electrons from Ca and Nb.states The local maximum in loss function at about 25 eV is due to the local minima of $\varepsilon_2$ at this energy. The experimentally determined loss function (see Section 4.3) on comparison with literature [17-19] allows one to identify the Ca $M_{2,3}$ and Nb $N_{2,3}$ edges at 35 eV and 46 eV. Clearly, the position of the corresponding excitations determined by the *ab-initio* calculations is inaccurate.

## 3.7 Semi-core states

It has been known that *ab-initio* methods like DFT underestimate the position of semi-core states [20]. This stems from two causes. Firstly, DFT based methods cancel self-interaction

incompletely [21]. Secondly, the excitations due to semi-core effects produce large excitonic effects which cannot be modeled by single particle approaches [22]. We attribute the above to cause the discrepancy in the position of the computed Ca $M_{2,3}$ and Nb $N_{2,3}$ edges.

To better model these semi-core states an empirical method is proposed. The $\varepsilon_2$ relates to excitations of electrons. These excitations are due to the valence and semi-core electrons excited into the unoccupied states. Hence, to better model the excitations due to semi-core states, separate $\varepsilon_2$ were computed due to valence and semi-core states. As, the excitations due to semi-core states occur at energies larger than the ones computed by conventional DFT methods, a mathematical shift to the $\varepsilon_2$ due to semi-core states to a higher energy by a value $\Delta E$ is applied. By varying $\Delta E$ a good convergence between the experimental and computed loss functions with regards to Ca $M_{2,3}$ and Nb $N_{2,3}$ edges for $\Delta E = 2.5$ eV was obtained. The corrected $\varepsilon_1$, $\varepsilon_2$ and loss function are depicted in Figure 3.10. The feature in the corrected loss function at 44.5 eV depicts the Nb $N_{2,3}$ edge. The excitation of K-3p electrons into unoccupied states results in the excitation at 27.8 eV as is seen in the loss function. The peak in $\varepsilon_2$ at 32.8 eV, which is related to the excitation of Ca-3p electrons is indiscernible in the loss function due to the plasmon peak at 34 eV.
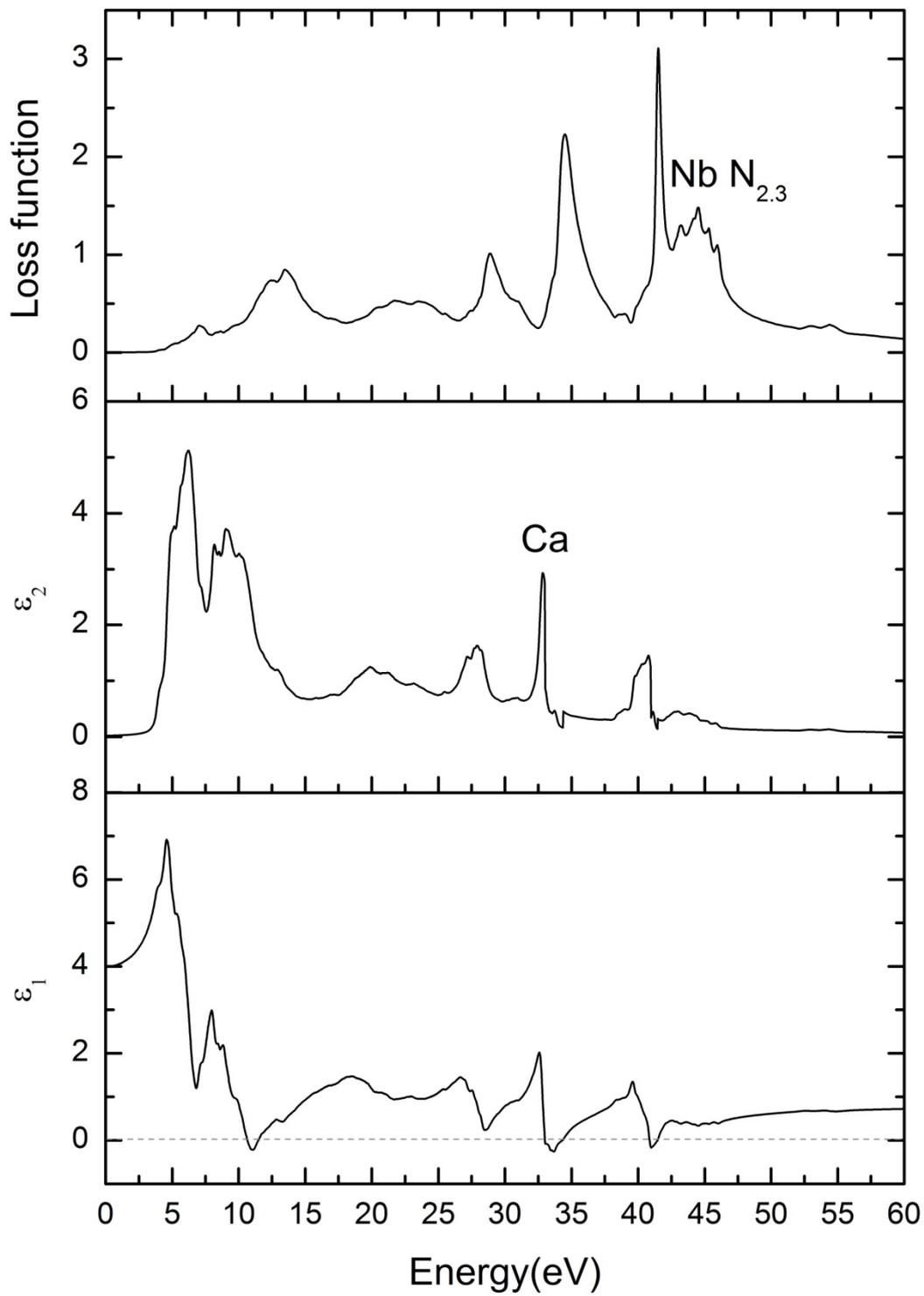
Figure 3.10: The corrected $\varepsilon_1$, $\varepsilon_2$ and loss function of $KCa_2Nb_3O_{10}$.

## 3.8 Comparison with literature

DFT calculations performed in the present work suggest $KCa_2Nb_3O_{10}$ to be a direct band gap semiconductor. Though there does not exist any report about the type of band gap in $KCa_2Nb_3O_{10}$, a recent report [23] suggests that $[TBA_xH_{1-x}]^+[Ca_2Nb_3O_{10}]^-$ nanosheets formed from $KCa_2Nb_3O_{10}$ are indirect-band gap semiconductors. These measurements could still conform with the results shown in this work if $KCa_2Nb_3O_{10}$ turns from direct to indirect type semiconductor upon exfoliation. This however can only be confirmed upon performing calculations on $[TBA_xH_{1-x}]^+[Ca_2Nb_3O_{10}]^-$ nanosheets which are tedious and beyond the scope of this work.

The band gap value (3.1 eV) determined using DFT calculations employing TB-mBJ potential matches well with the experimentally determined value of 3.35 eV by Domen *et al*. [24]. The paltry incongruence could be imputed to the low DOS at the conduction band onset which makes inference of band onset fallacious. TB-mBJ potentials have previously been demonstrated to successfully determine the band gaps of semiconductors (Si, Ge, GaAs etc.), insulators (LiF, Kr etc.) and correlated transition metal oxides (MnO, NiO) [6]. This study further shows the applicability of the TB-mBJ methodology to dielectric material $KCa_2Nb_3O_{10}$ for determining the band gap.

Generally for determining the optical properties of a material, a "scissor shift" is often applied [25-27]. In this scissor shift, the excitations are mathematically shifted to a higher energy because the conduction band Kohn-Sham eigenvalues calculated are generally incorrect. The calculations performed in this work however match well with the experimental loss function (Section 3.3) thereby showing that TB-mBJ methodology allows for determination of optical properties without applying a scissor shift (for energy range < 20 eV).

## 3.9 Summary

Structure optimizations indicate the atomic positions of the individual atoms in $KCa_2Nb_3O_{10}$ to be flatter in the *bc* planes than the structure model proposed by Tokumitsu et al. [4]. This implies the stability of a flatter structure along the *bc* planes. This result is of importance, because this is the only family of planes across which the $KCa_2Nb_3O_{10}$ could be chemically exfoliated into a 2D-nanostructure [28]. The band gap value of 3.1 eV computed using TB-mBJ potential matches well with the value of 3.35 eV experimentally determined by Domen and co-worker's catalysis measurements [24]. The calculated bandstructure reveals that

$KCa_2Nb_3O_{10}$ is a direct-type semiconductor. The DOS shows a low density of conduction band states close to the band onset of 3.1eV. The partial DOS reveals that the onset of conduction band is predominantly due to Nb-3d states. The computed $\varepsilon_1$ suggests the existence of three plasmon excitations in $KCa_2Nb_3O_{10}$. The computed loss function and $\varepsilon_2$ depict the excitations of semi-core electrons from K-3p, K-3s, Ca-3p and Nb-4p orbitals into unoccupied states. A shift of excitations due to the semi-core electrons by 2.5eV to higher energies allows for better modeling of the Ca $M_{2,3}$ and Nb $N_{2,3}$ edges in the loss function.

## 3.10 Chapter references

[1]    J. Hafner. Atomic-scale computational materials science. *Acta Mater*, 48, 71 (2000)

[2]    D. J. Singh and L. Nordstrom. *Planewaves, Pseudopotentials, and the LAPW Method.* Springer Science + Media Inc. (2006)

[3]    P. Blaha, K. Schwarz, G. K. H. Madsen, D. Kvasnicka and J. Luitz, WIEN2k, An Augmented Plane Wave + Local Orbitals Program for Calculating Crystal Properties (Karlheinz Schwarz, Techn. Universität Wien, Austria) (2001) ISBN 3-9501031-1-2

[4]    T. Tokumitsu, K. Toda, T. Aoyagi, D. Sukuraba, K. Uematsu, and M. Sato. Powder neutron diffraction study of layered perovskite $KCa_2Nb_3O_{10}$. *J. Cer. Soc. Jap.*, 114, 795 (2006)

[5]    J. P. Perdew, K. Burke, and M. Ernzerhof. Generalized Gradient Approximation made simple. *Phys. Rev. Lett.*, 77, 3865 (1996)

[6]    F. Tran and P. Blaha. Accurate band gaps of semiconductor and insulators with a Semilocal Exchange-Correlation Potential. *Phys. Rev. Lett.*, 102, 226401 (2009)

[7]    C. Ambrosch-Draxl and J. Sofo. Linear optical properties of solids within full-potential linearized augmented planewave method. *Comp. Phys. Comm.*, 175, 1 (2006)

[8]    A. Seidl, A. Görling, P. Vogl, J. A. Majewski, and M. Levy. Generalized Kohn-Sham schemes and the band gap problem. *Phys. Rev. B*. 53, 3764 (1996)

[9]    W. Ku and A. G. Eguiluz. Band-gap problem in semiconductors revisited: Effects of core states and many-body self-consistency. *Phys. Rev. Lett*. 89, 126401 (2002)

[10]   A. S. Bamzai and B. M. Deb. The role of single-particle density in chemistry. *Rev. Mod. Phys.* 53, 95 (1981)

[11]   Y. Abraham, N. A. W. Holzwarth, and R. T. Williams. Electronic structure and optical properties of $CdMoO_4$ and $CdWO_4$. *Phys. Rev. B.*62, 1733 (2000)

[12]   M. Fox. *Optical Properties of Solids*. Oxford University Press, UK (2010)

[13]   V. Gallegos-Orozco, R. Martinez-Sanchez, and F. Espinosa-Magana. *In situ* characterization of ferroelectric transitions in $BaTiO_3$ by EELS and comparison with *ab initio* methods. *Phys. Rev. B.* 77, 045128 (2008)

[14]   H. Fröhlich. *Theory of Dielectrics*. Oxford University Press, UK (1958)

[15]   K. Kopitzki. *Einführung in Festkörperphysik*. B. G. Teuber Publishers, Stuttgart Germany (1993)

[16]   R. F. Egerton. *Electron Energy-Loss Spectroscopy in the Electron Microscope*. Springer Science + Media LLC. (2011)

[17]   K. S. Katti, M. Qian, D. W. Frech, and M. Sarikaya. Low-loss electron energy-loss spectroscopy and dielectric function of biological and geological polymorphs of $CaCO_3$. *Microsc. Microanal.* 5, 358 (1999)

[18]   C. C. Ahn, A. L. Krivanek, R. P. Burgner, M. M. Disko, and P. R. Swann. *EELS Atlas,* HR-EM Facility, Arizona State University, Tempe, Arizona, US (1983)

[19]   D. Bach, R. Schneider, D. Gerthsen, J. Verbeeck, and W. Sigle. EELS of Niobium and Stoichiometric Niobium-Oxide phases- Part I: Plasmon and near-edges fine structure. *Microsc. Microanal.* 15, 505 (2009)

[20]   M. Arai, S. Kohiki, H. Yoshikawa, S. Fukushima, Y. Waseda, and M. Oku. Photoelectron energy-loss functions of $SrTiO_3$, $BaTiO_3$ and $TiO_2$: Theory and experiment. *Phys. Rev. B.* 65, 085101 (2002)

[21]   T. Miyake, P. Zhang, M. L. Cohen, and S. G. Louie. Quasiparticle energy of semicore *d* electrons in ZnS: Combined LDA+U and GW approach. *Phys. Rev. B.* 74, 245213 (2006)

[22] R. Laskowski and P. Blaha. Understanding the $L_{2,3}$ x-ray absorption spectra of early *3d*-transition elements. *Phys. Rev. B.* 82, 205104 (2010)

[23] K. Akatsuka, G. Takanashi, Y. Ebina, M. Haga, and T. Sasaki. Electronic band structure of exfoliated titatium – and/or niobium based oxide nanosheets probed by electrochemical and photoelectrochemical measurements. *J. Phys. Chem. C* 116, 12426 (2012)

[24] K. Domen, J. Yoshimura, T. Sekine, A. Tanaka, and T. Onishi. A novel series of photocatalysts with an ion-exchangeable layered structure of niobate. *Catalysis Lett.* 4, 339 (1990)

[25] S. Saha, T. P. Sinha, and A. Mookherjee. Electronic structure, chemical bonding and optical properties of paraelectric $BaTiO_3$. *Phys. Rev. B* 62, 8828 (2000)

[26] Y. Abraham, N. A. W. Holzwarth, and R. T. Williams. Electronic structure and optical properties of $CsWO_4$ and $CdMoO_4$. *Phys. Rev. B* 62, 1733 (2000)

[27] S. Z. Karazhanov, P. Ravindran, A. Kjekshus, H. Fjellfag, and B. G. Svensson. Electronic structure and optical properties of ZnX (X=O, S, Se, Te): A density functional study. *Phys. Rev. B* 75, 155104 (2007)

[28] Y. Ebina, T. Sasaki, and M. Watanabe. Study on exfoliation of layered perovskite-type niobates. *Solid State Ionics* 151, 177 (2002)

# 4     Electron energy loss spectroscopy of $KCa_2Nb_3O_{10}$

EELS pertains to analyzing the energies of electrons which have interacted with the specimen material. As the probing electrons interact with the material, they lose energy while they cause excitations in the material [1]. The energy lost in such processes reflects the chemical and electronic structure of the material. The work presented here is based on the analysis of EELS signal in the transmission mode. The low energy (*E<50* eV) region predominantly reflects excitations of the valence electrons and is sometimes referred to as valence electron energy loss spectroscopy (VEELS). These excitations can be single electron in nature or collective (known as plasmon). In the recent years with the advent of commercially available monochromators, determining band gaps using VEELS has become a viable experimental option. This chapter entails VEELS and EELS measurements performed on the bulk $KCa_2Nb_3O_{10}$ to understand its electronic structure. Results presented are currently under review at the Physical Review B as a publication entitled "Electronic structure of $KCa_2Nb_3O_{10}$ as envisaged by density functional theory and valence electron energy loss spectroscopy." All measurements elaborated here were performed with Yaron Kauffmann, Department of Materials Science and Engineering, Technion - Israel Institute of Technology.

## 4.1 VEELS Acquisition

The acquisition of EEL spectra is circuitous. A number of parameters like the collection angle, time of acquisition, spectrometer dispersion and thickness of area chosen are very paramount in acquiring the appropriate spectra for analysis. All measurements were performed using an FEI-TITAN 80-300 scanning transmission electron microscope equipped with a field emission gun, a Wien-type monochromator and Gatan Tridiem 866 energy filter having a 2k-CCD camera. For VEELS measurements, an area of single crystalline $KCa_2Nb_3O_{10}$ was chosen such that its thickness, as determined by an EELS thickness map [1], was approximately equal to 0.3 times the inelastic mean free path length $\lambda$. To offset effects due to anisotropy [2], the sample was oriented into a random orientation such that it was not in zone-axis with any high symmetry direction. STEM mode was used for all VEELS measurements employing convergence and collection angles of 9.5 mrads each. To make sure

the point-spread function of the detector [1] does not limit the resolution of the measurements, a spectrometer dispersion of 0.02 eV/channel was used. A spectrum acquired in the energy range -5 to 36 eV is shown in Figure 4.1. Evidently for a thin sample, the most dominant feature is the ZLP at 0 eV. The ZLP when acquired in vacuum expounds on the energy spectrum of the electrons emitted by the electron source.
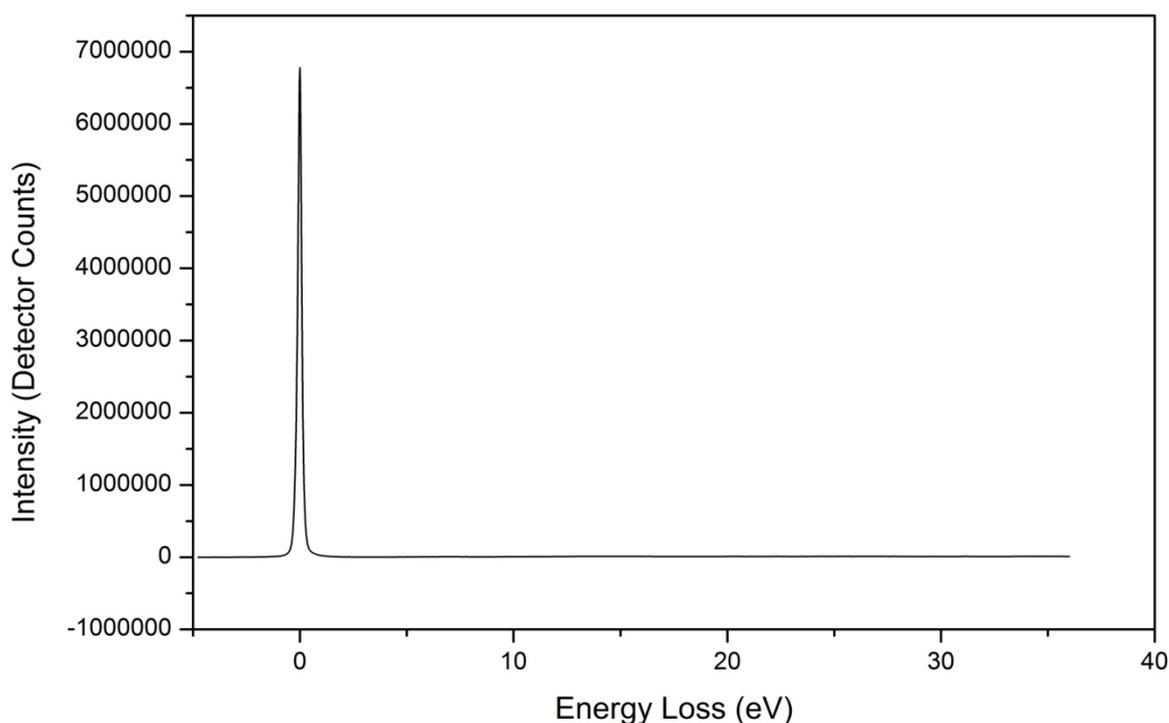


Figure 4.1: VEEL spectrum acquired from a $KCa_2Nb_3O_{10}$ particle ca. 0.3 times the mean free path length ($\lambda$) thick showing the most dominant feature being the ZLP.

A closer look at the acquired VEEL spectrum, illustrates the presence of valence excitations, exemplified in Figure 4.2. For thin samples the intensity of valence loss excitations is more than two orders of magnitude less than that of ZLP. This makes it difficult to improve the signal-to-noise ratio (SNR) due to the limited intensity range the detector is able to record signal in. Acquiring VEELS from a thicker region can decrease the difference between the intensity of ZLP and valence loss excitations, however such data would have limited usability for determining band gaps as has been shown by Gu and co-workers [3]. The acquired VEEL spectrum shown in Figure 4.2 shows the valence loss excitations and allows for determining the loss function $S$ of $KCa_2Nb_3O_{10}$. The low SNR however makes it difficult to determine the band gap with reasonable accuracy.
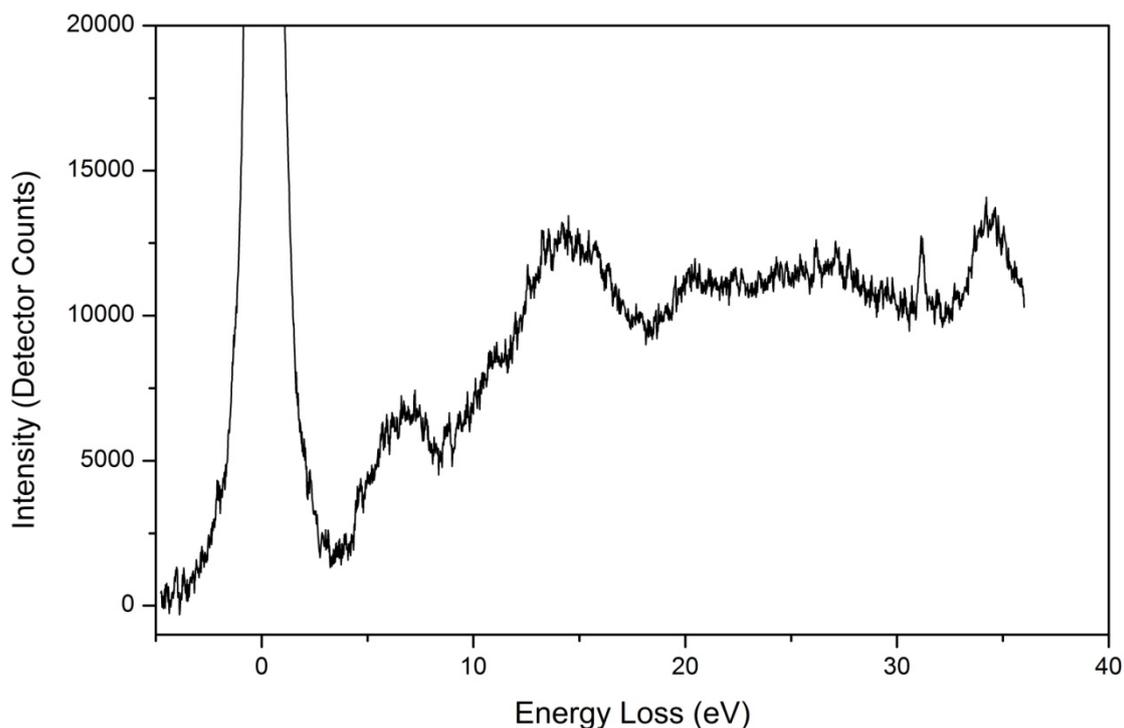
Figure 4.2: A magnified version of VEEL spectrum of $KCa_2Nb_3O_{10}$ illustrating the valence electron excitations.

Therefore for acquiring a better VEEL spectrum with higher SNR from which determination of band gap would be possible, a two-fold method was adopted. Another VEEL spectrum was acquired from the same position, with a different energy loss region probed. The second VEEL spectrum was acquired from approximately 1.5 to 42 eV, such that it encompassed the tail of the ZLP on the positive side and the valence loss excitations. For accurate determination of the band gap the calibration of this spectrum is indispensable. Hence, to calibrate this spectrum both the spectra were juxtaposed and the second spectrum containing the ZLP tail and valence loss features with better SNR moved (along the energy axis) until overlap was achieved between the valence loss features. The error in this calibration procedure can be approximated to $\pm\, 0.1$ eV. The VEEL spectrum after calibration is shown in Figure 4.3 along with the VEEL spectrum containing the complete ZLP which was previously acquired. After calibration, the two spectra were spliced into a single spectrum. This spectrum was used for all subsequent VEELS analysis. The spliced spectrum shown in Figure 4.4 shows significantly better SNR, which is important especially in the region 2-5eV.
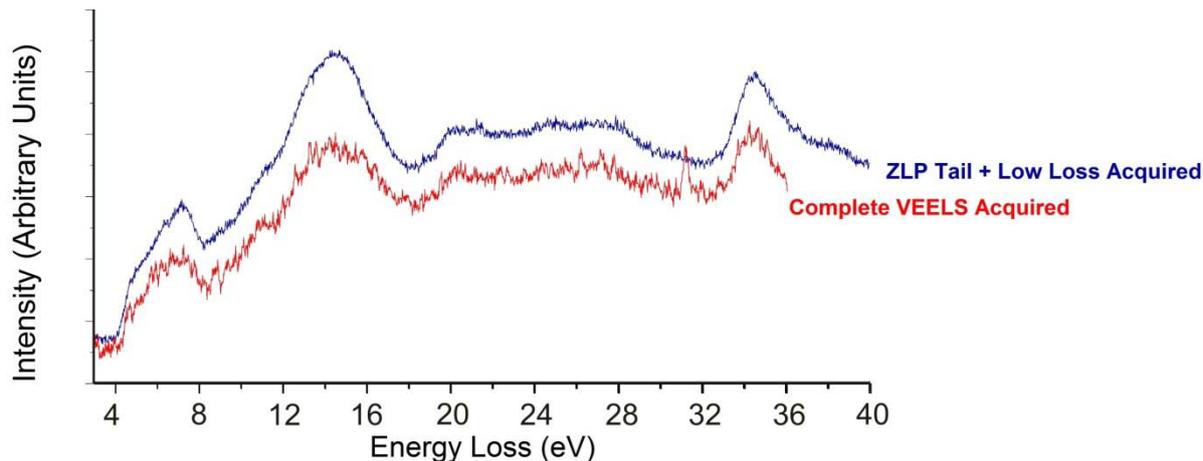
Figure 4.3: The calibrated VEEL spectrum in the region 3-40 eV containing the ZLP tail and valence excitations (blue) and the VEEL spectrum acquired with complete ZLP (red).
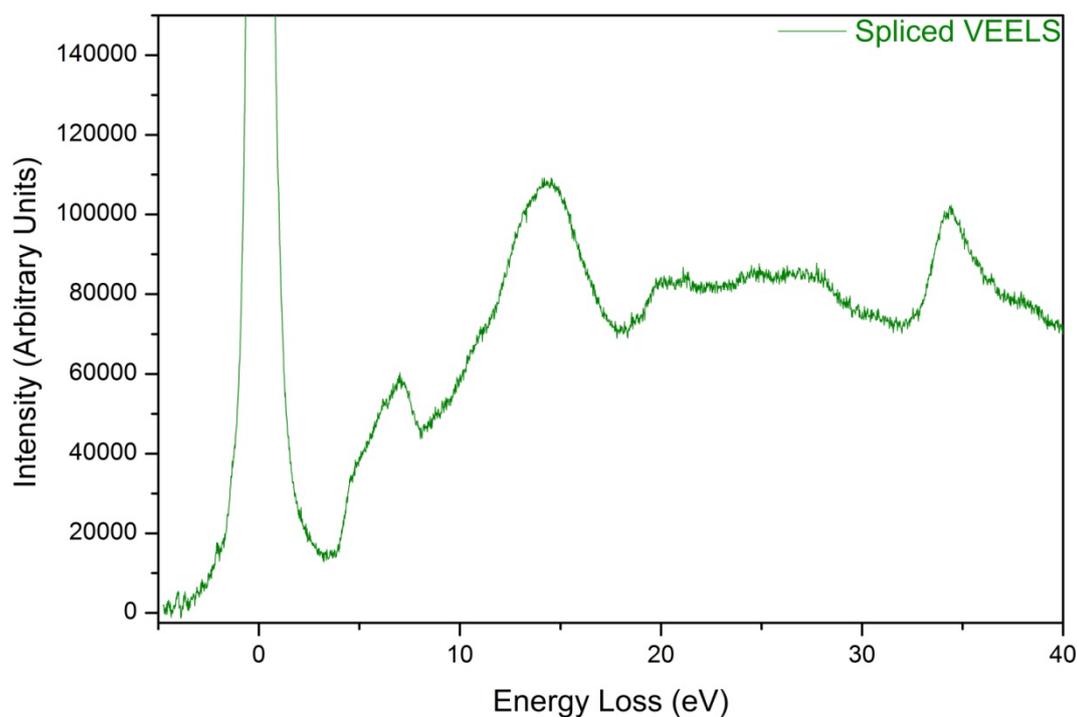


Figure 4.4: The spliced spectrum showing the VEEL spectrum of $KCa_2Nb_3O_{10}$ with better SNR.

## 4.2 Band gap determination using VEELS

The ZLP contains the electrons which have lost no perceptible energy. The electron sources do not eject electrons with a fixed energy. Typically the energy spread of a thermal electron source, as described by its FWHM could be as much as 1-2 eV. Usage of a Schottky source improves it, however a cold field emission gun (FEG) is even better and can have an energy

spread (FWHM) of 0.3 eV. In addition, it is also possible to mathematically deconvolute the acquired loss spectrum obtained with a cold-FEG for determining band gaps [4].

Without the deconvolution, the energy resolution offered by cold-FEG in VEELS experiments is not sufficient for determination of band gaps due to the pronounced tails of the ZLP. Moreover, applying deconvolution on noisy data can generate artifacts. Therefore, determination of band gaps was impeded due to instrumental limitations. Recently, monochromators have become commercially available. Typically, it is possible to achieve an energy resolution up to 0.1 eV with the help of these monochromators. In this study, a Wien-type monochromator was used which allowed for a FWHM up to 0.15 eV.

The energy profile of the source is sometimes also referred to as the instrument function. The acquired VEEL spectrum contains both the ZLP and the valence loss excitations which might superimpose on each other. In cases of insulators or very high band gap semiconductors with band gap energies greater than 6 eV, the two features can be separately identified and hence the onset of the first valence loss excitation (band gap) can be determined. However for the case of semiconducting materials with band gaps in the range 1-4 eV, the ZLP and conduction band onset can overlap, thereby making the determination of band gap non-trivial. Removal of the ZLP would allow for obtaining the loss function. Theoretically for perfectly monochromated electron source, the ZLP would be a delta function, however in reality, it has finite energy spread. A number of ways exist for describing the ZLP. It can be approximately described as a Gaussian, a Gaussian-Lorentzian or other mathematical functions [1]. The most accurate description is acquiring the ZLP in vacuum.

The tail of the ZLP have a high level of noise as shown in Figure 4.5 where the acquired VEELS from $KCa_2Nb_3O_{10}$ and the spectrum acquired from vacuum are shown after normalizing their intensities. Subtracting the ZLP acquired in vacuum from the VEEL spectrum should ideally allow for determination of band gaps, however as is evident from Figure 3.5, the high noise levels on the tails would make it difficult to determine the exact position of conduction band onset in the energy range 2-4eV. As the DFT calculations and the experimental measurements on the band gap of $KCa_2Nb_3O_{10}$ by Domen and co-workers [5] predict the band gap to be in this energy domain, a need for better method to separate the instrument function and the valence excitations cannot be understated.
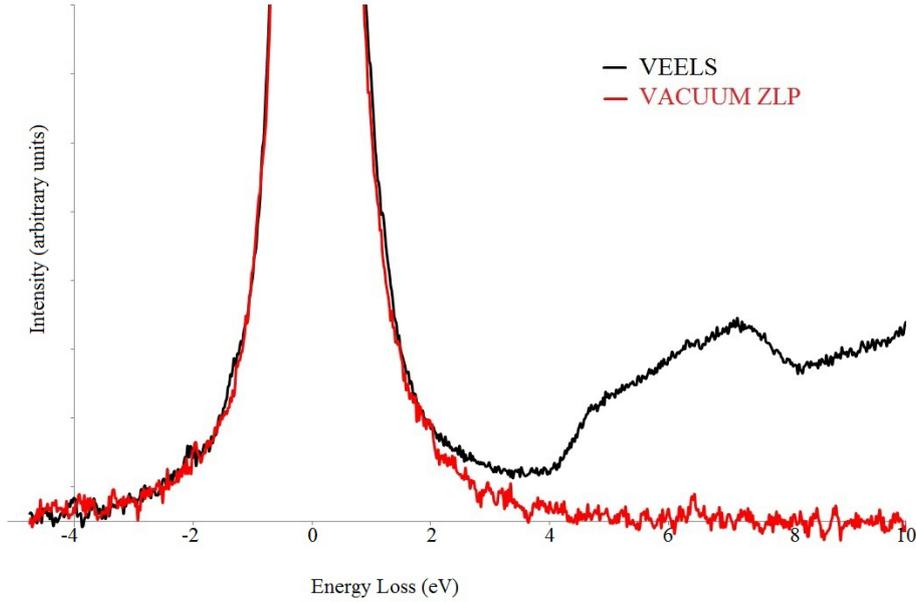
Figure 4.5: The VEEL spectrum acquired from $KCa_2Nb_3O_{10}$ (black) and the ZLP acquired in vacuum (red). The VEEL spectrum acquired in vacuum had a lower exposure time so as to limit detector damage due to the higher intensity of ZLP in vacuum.

Removal of a superimposing feature preceding the energy loss excitation of interest has been an integral part of EELS analysis. For extracting the core-loss signal the most commonly used method is describing the preceding feature with a power-law function and subtracting it to obtain the signal due to the particular excitation. In the recent years, scientists have demonstrated the usage of this technique (power-law subtraction) to remove the ZLP component from the acquired VEEL spectra [3,6,7]. Erni and Browning [7] have determined the value of band gap from the power-law subtracted ZLP using an intricate mathematical operation. They smoothened the ZLP subtracted spectrum using a Savitzky-Golay filter and calculated the first derivative of the smoothened curve. Subsequently they fitted a Lorentzian to the first derivative and calculated the FWHM of the first peak of the Lorentzian. Then they determined the band gap $E_g$ as given in Equation 4.1. where $E_{IP}$ is the inflection point (first maximum of the Lorentzian) and $L_{FWHM}$ the FWHM for the first peak of the Lorentzian.

$$E_g = E_{IP} - 0.5 L_{FWHM} \tag{4.1}$$

Instead of using this approach, in the present work, band gap was determined as the onset point where the power-law subtracted signal crosses the noise level. Irrespective of the method used for determination of the onset, careful attention needs to be paid to the region where the power-law approximation is applied to determine the ZLP tail.

63
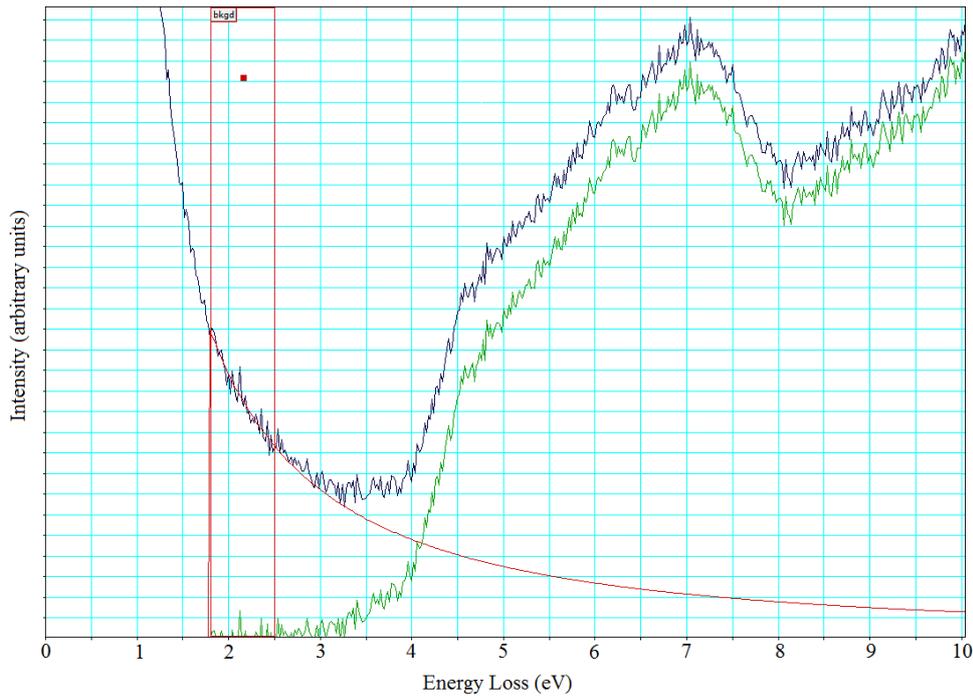
Figure 4.6: The VEEL spectrum (black) and the ZLP subtracted spectrum (green) when power-law is used to describe the tail of ZLP (red) on the basis of the ZLP tail in the energy range 1.8-2.5 eV.
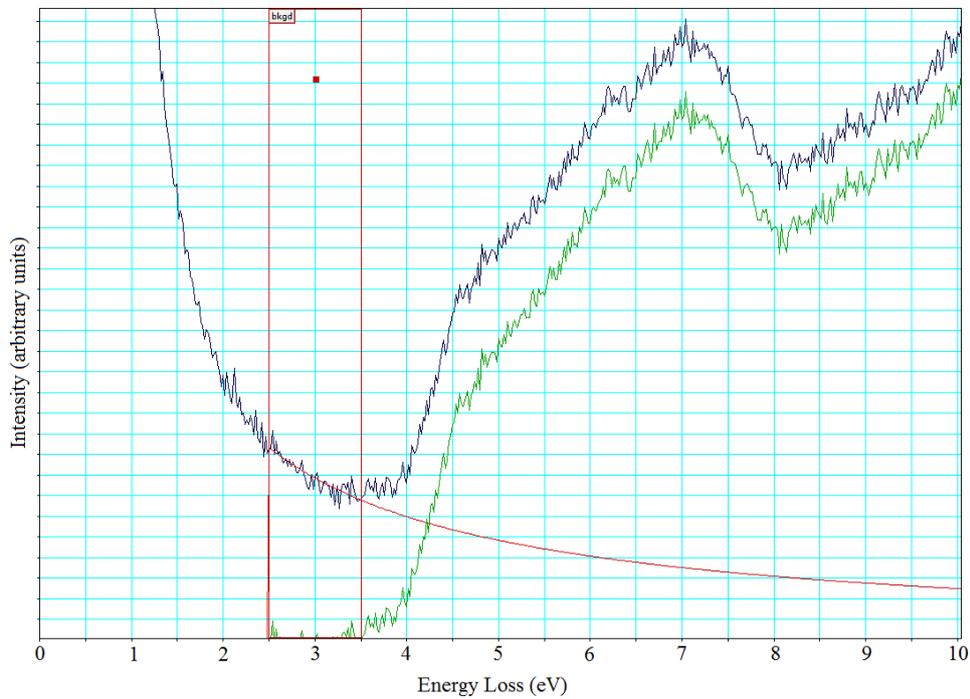


Figure 4.7: The VEEL spectrum (black) and the ZLP subtracted spectrum (green) when power-law is used to describe the tail of ZLP (red) on the basis of the ZLP tail in the energy range 2.5-3.5 eV.

Figures 4.6 and 4.7 highlight the dependence of the band gap onto the region where the power-law function was used to describe the tail of the ZLP. By describing the power-law function in the energy range 1.8-2.5 eV (Figure 4.6), the onset can be determined as 3.2 eV whereas describing it in the energy range 2.5-3.5 eV (Figure 3.7) the onset can be determined as 3.6 eV. Out of the two, the first one is correct. This is because power-law can appropriately describe a decaying signal, however the signal in the energy range 3-4 eV is rather flat. This implies the decaying tail of the ZLP is superimposed with a monotonically increasing signal leading to an overall constant intensity in the energy range 3-4 eV. The conduction band onset is better illustrated in the ZLP subtracted signal shown in Figure 4.8. Given the error in the alignment procedure to be $\pm 0.1$ eV, the band gap of $KCa_2Nb_3O_{10}$ is determined to be $3.2 \pm 0.1$ eV within the range of experimental error. If alignment procedures could be perfected and better SNR obtained, the error in the measurement could be as low as 0.04 eV (the width of two channels) however experimental limitations hinder this utopian target. However, the band gap value augurs well with the calculated band gap value of 3.1 eV and the experimentally determined value of 3.35 eV by Domen and co-workers [5].
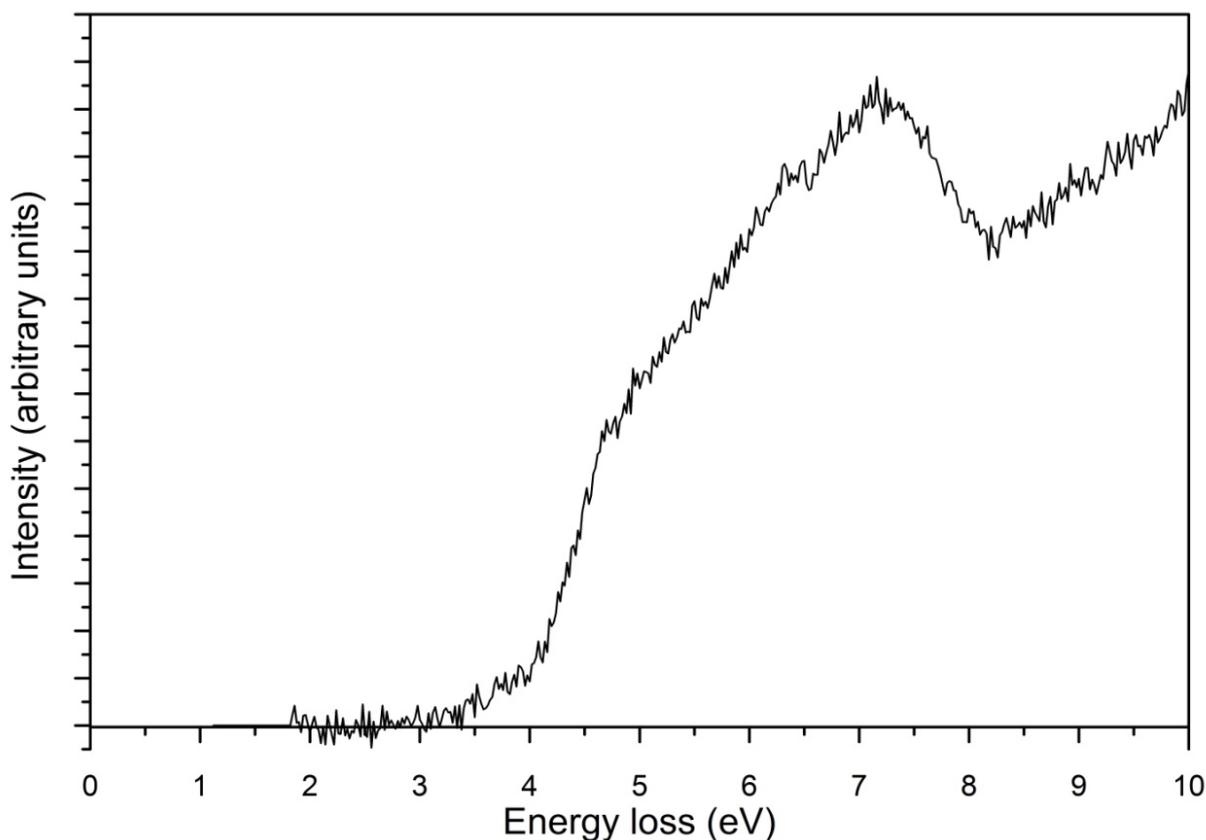


Figure 4.8: The ZLP subtracted VEEL spectrum of $KCa_2Nb_3O_{10}$ indicating the conduction band onset of 3.2 eV.

## 4.3 Loss function comparison

The ZLP subtracted loss function is related to the double differential scattering cross section. In the case of thicker samples, multiple scattering can occur, whereby an electron can excite multiple excitations before it exits the sample. In such cases the recorded EEL or VEEL spectrum contains these multiple scattering processes superimposed on the ideal spectrum which contains only single excitations, known as single scattering distribution. Mathematical formulations have been developed to remove such multiple scattering effects, for example the Fourier Log deconvolution and the Fourier Ratio deconvolution [1]. These methods have been extensively used by scientists for obtaining the single scattering distribution when VEELS has been acquired from thicker regions [8,9]. However, these multiple scattering processes contribute significantly to the signal when the thickness of the area irradiated is close to the mean free path length or greater. Given that, the area investigated for VEELS acquisition is about 0.3 times the mean free path length thick, the probability of multiple scattering events interfering with the acquired signal is negligible.

The ZLP subtracted VEEL spectrum, which is the experimentally determined loss function, and the theoretically determined loss function are plotted in Figure 4.9.
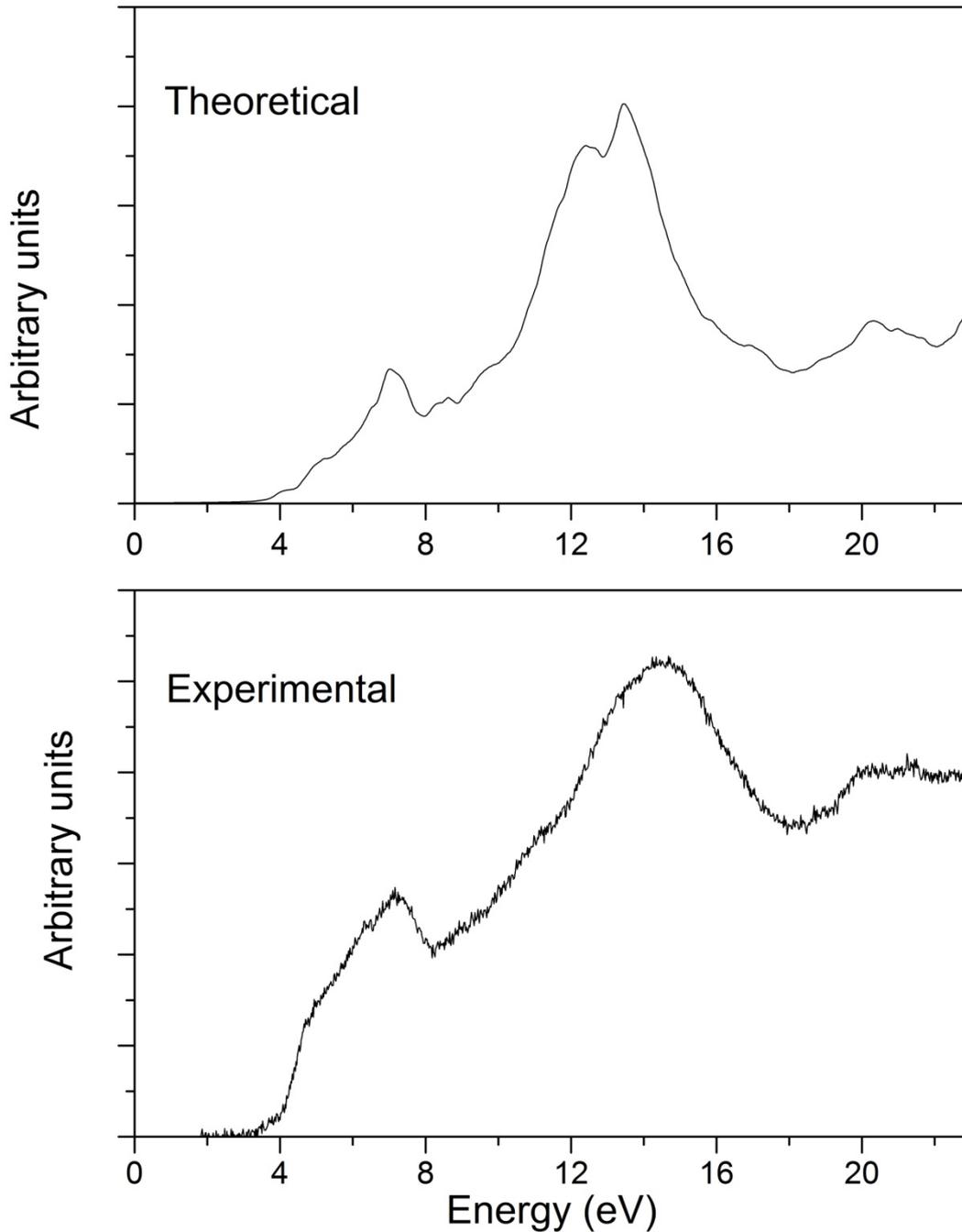
Figure 4.9: The theoretically and experimentally determined loss function of $KCa_2Nb_3O_{10}$.

The experimentally determined and the theoretically calculated loss functions show excellent agreement up to 20 eV. The resolution of the theoretically determined loss function is better as it allows for discerning sub features of larger peaks, for example, the peak in the energy range 12-16 eV appears as a single broad peak in the experimental spectrum, however in the theoretical spectrum the splitting of the peak is visible.

The excitations in the energy range $E<20$ eV are dominated by single electron transitions, as opposed to collective excitations like plasmon. A comparison with the theoretically computed

imaginary part of the dielectric function allows one to understand the nature of these single electron excitations. The peak in the region 5-7.5 eV can be attributed to the excitations of valence band electrons from Nb-4d states into the unoccupied states with Nb-$t_{2g}$-like character.

## 4.4 Plasmons

A plasmon excitation is a collective excitation mode where the delocalized electrons interact with the electromagnetic fields created by the incident electron as it passes through and move in a collective motion as a superimposition on their random thermal motion. Mathematically the conditions for plasmon excitation are when the real part of the dielectric function crosses the energy axis with a positive slope. As shown in Section 3.5 theoretical calculations suggest these conditions to be satisfied at three points $E_{p1}$ 11.3 eV, $E_{p2}$ 30.0 eV and $E_{p3}$ 37.0 eV. A comparison between the experimentally and theoretically determined loss function (illustrated in Figure 4.10) in the energy range 0-40 eV indicates differences between the loss functions in the high energy range *20* eV<*E*<*40* eV.

The biggest difference that one sees between the two loss functions is the intensity of plasmon excitations $E_{p2}$ 30.0 eV and $E_{p3}$ 37.0 eV. Theoretically determined loss function shows (Figure 4.10) these plasmon excitations to have a small energy width and high intensity, however in the experimentally acquired spectrum these two features are non-existent. This indicates a possible limit to the computational methodology for properly mimicking the higher energy excitations.

It is worth comparing the loss function of $KCa_2Nb_3O_{10}$ with $Nb_2O_5$ which also has Nb with an oxidation state of +5. Bach and co-workers have shown [10] that $Nb_2O_5$ has a broad triple plasmon in the energy range 15-27 eV. Theoretical calculations also predict the existence of three plasmons however the experimental loss function does not contain the last two as narrow high intensity peaks as the calculations suggest. Similar to the experimental spectrum of $Nb_2O_5$ published by Bach and co-workers [10] a broad flat valley like feature is observed in the experimental loss function in the energy range 20-28 eV, however it is hard to categorize these excitations.
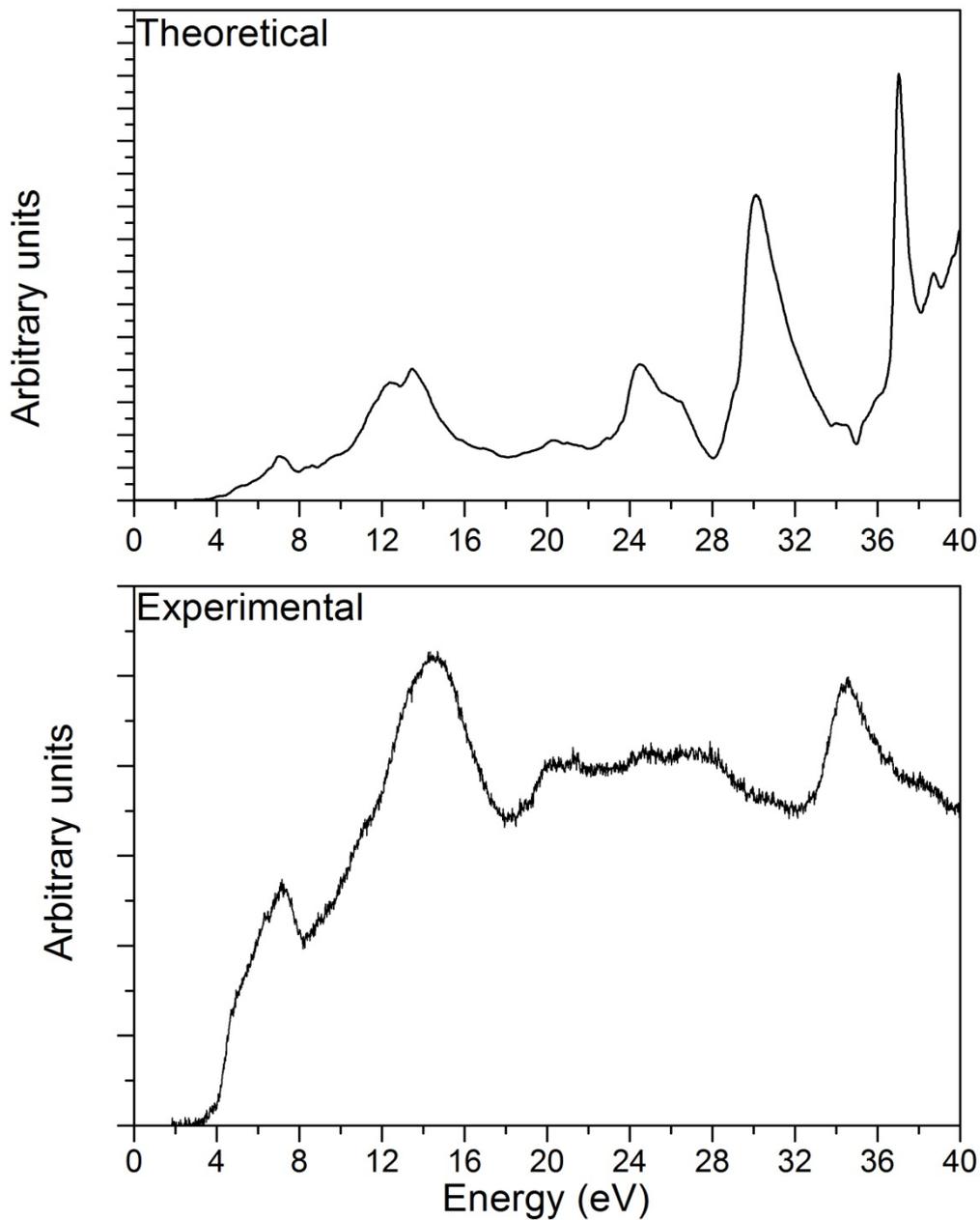
Figure 4.10: Theoretically and experimentally determined loss functions in the energy range 0-40 eV.

## 4.5 Semi-core excitations

Excitations of the semi-core electrons to the higher unoccupied levels are manifested in the experimentally acquired EEL spectrum. To this end an EEL spectrum was acquired in TEM mode using a spectrometer dispersion of 0.2 eV/channel. The EEL spectrum is shown in Figure 4.11.
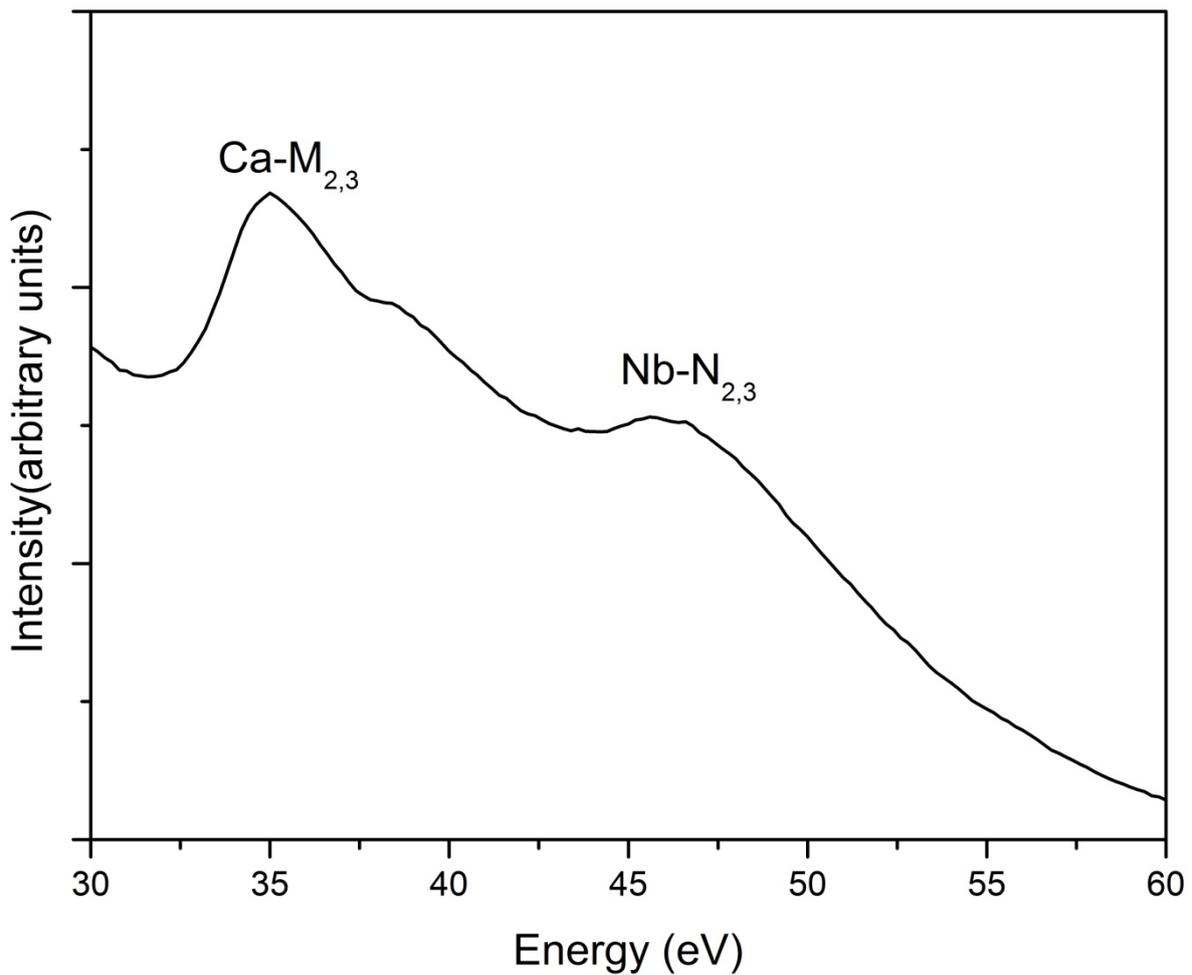
Figure 4.11: EEL spectrum of $KCa_2Nb_3O_{10}$ acquired in TEM mode showing the edges Ca-$M_{2,3}$ and Nb-$N_{2,3}$.

Two features are observed with maxima at 35eV and 45.5 eV. Comparison with literature [11,12] allows for characterizing the first peak at 35 eV to belong to the Ca-$M_{2,3}$ edge. Bach and co-workers [10] showed that Nb in an oxidation state of +5 shows a delayed maximum at the $N_{2,3}$ edge at 46 eV. The imaginary part of the computed dielectric function (Figure 3.7) suggests excitations due to Ca-3p and Nb-4p electrons to occur at 28 and 35 eV.

These facts indicate the semi-core excitations to occur at energies higher than those predicted by DFT calculations. Scientists have previously shown that DFT calculations predict the semi-core energy levels to exist at energies higher than they actually exist [13]. This has been linked to fact that self-interaction is incompletely canceled in these calculations [14]. Corrected loss function computed by mathematically shifting the position of excitations in $\varepsilon_2$ due to semi-core states to a higher energy value by 2.5eV are shown in Figure 4.12. The position and shape of the computed Nb-$N_{2,3}$ edge matches well with that of experimentally

70

determined one. A closer look at the corrected $\varepsilon_2$ computed indicates the position of excitations due to Ca-3p electrons at 32.8 eV, however the plasmon excitation in the corrected loss spectrum at 34 eV makes it hard to identify the Ca-$M_{2,3}$ edge in the computed corrected loss function.
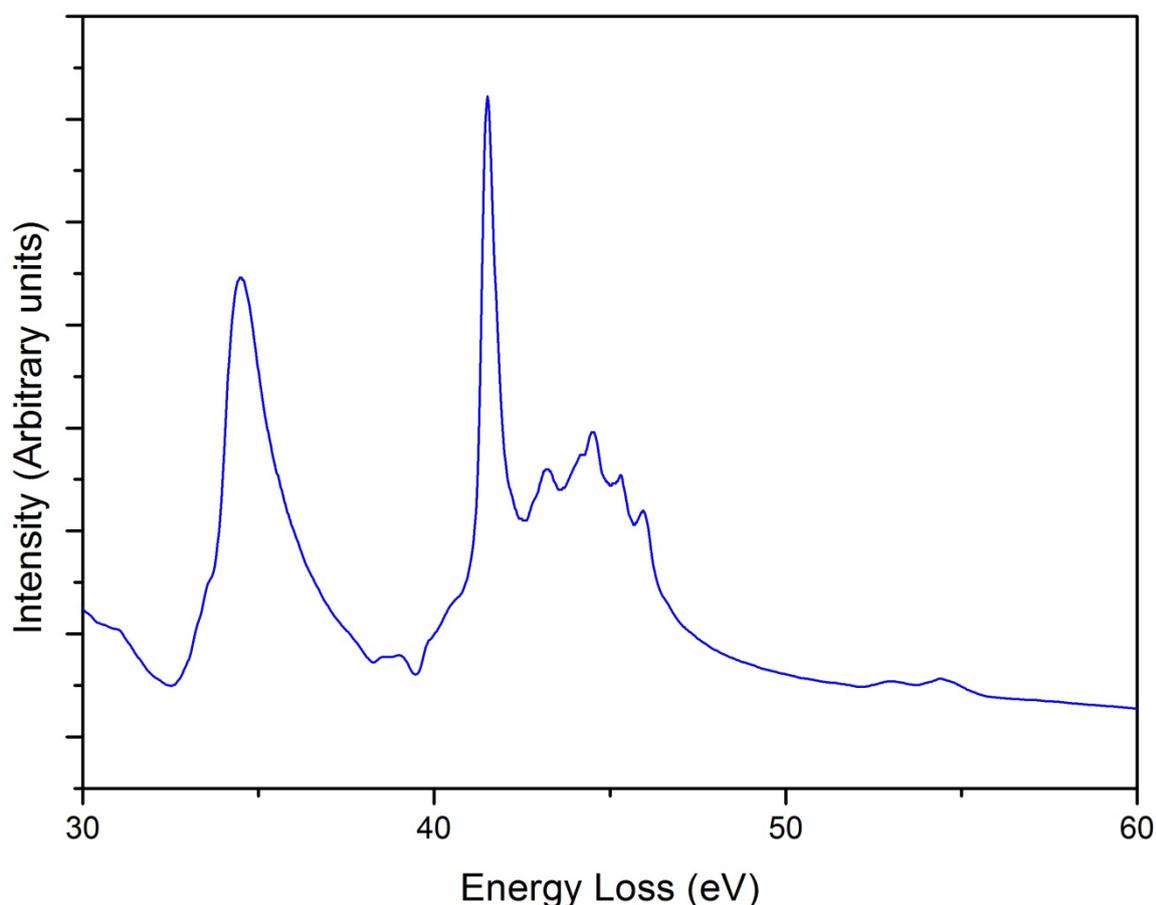


Figure 4.12: The corrected loss function of $KCa_2Nb_3O_{10}$ in the energy range 30-60 eV.

## 4.6 Core-loss Excitation

The core-loss EEL spectrum represents the excitations of electrons from deep lying core states into higher unoccupied states. As the deep lying core levels are localized i.e. they belong to specific atoms, these features can be related to the oxidations states, bonding character amongst others. The core-loss EEL spectrum of $KCa_2Nb_3O_{10}$ was acquired in diffraction mode with a collection angle of 9.5 mrads using cumulative acquisition mode with acquisition time of 0.64 s and a spectrometer dispersion of 0.2 eV/channel.

A comparison with literature allows for identification of the EELS edges at the following energies: Nb-$M_{4,5}$ onset 205 eV, maximum at 237 eV [10]; K-$L_{2,3}$ peaks at 294 and 296 eV [15]; Ca-$L_{2,3}$ peaks at 346 and 350 eV [16]; Nb-$M_{2,3}$ peaks at 362 and 377 eV [10,12]; O-K

edge, onset at 532 eV [12]. This qualitatively confirms the chemical composition of $KCa_2Nb_3O_{10}$ being K, Ca, Nb and O.
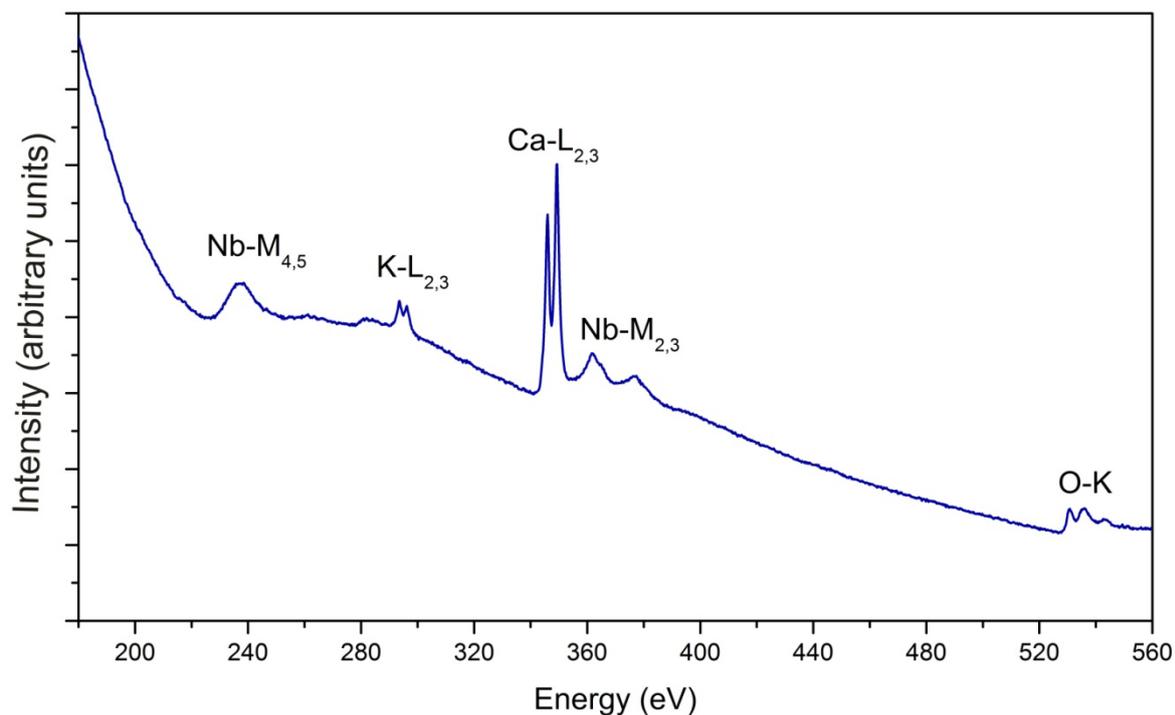


Figure 4.13: Core-loss EEL spectrum of $KCa_2Nb_3O_{10}$ acquired in TEM mode showing the $Nb-M_{4,5}$, $K-L_{2,3}$, $Ca-L_{2,3}$, $Nb-M_{2,3}$ and O-K edges.

## 4.7 Comparison with literature

VEELS measurements constituted of acquiring 50 spectra with an acquisition time of 0.14 s per acquisition. This choice was based on the fact that despite all the electromagnetic and noise insulation, the frequency of the mains power supply interferes and causes oscillations of the spectrum acquired [17]. The acquired spectra when juxtaposed showed variation in position to the extent few deci-electron volts (Illustrated in Figure 4.14) similar to the variations measured by Kimoto *et al*. [17].
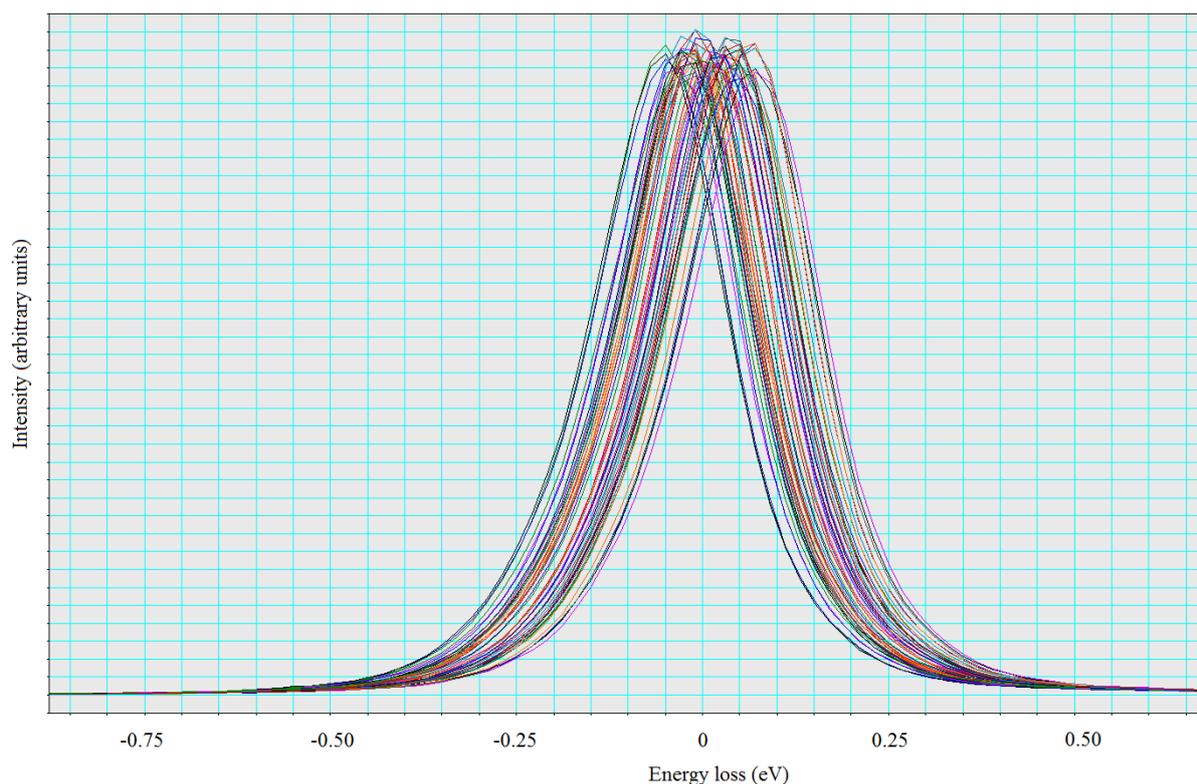
Figure 4.14: The fluctuations in the acquisition show the movement of ZLP in fifty successive acquisitions with an acquisition time of 0.14 s each.

Ströger-Pollach and Schattschneider had questioned the applicability of STEM-VEELS for correct band gap determination [18]. They had related it to the fact that their "difference-method" for mathematically removing the contribution of relativistic losses has limited applicability in the STEM mode [18]. However, the measurements shown in this work allow for successful determination of the band gap of $KCa_2Nb_3O_{10}$ in STEM mode, similar to other researchers who have been successful with this methodology [7,4,19]. This success is related to appropriate choice of thickness and collection angles such that Cerenkov radiation does not contribute significantly to the acquired spectrum [3].

Gu *et al.* had shown that when band gap measurements are performed in regions with thicknesses below about half the mean free path length in that material, Cerenkov losses contribute negligible scattering cross section [3] as is shown in Figure 4.15 (Reproduced from Ref. 3 with permission from the American Physical Society, © American Physical Society 2007). Therefore having chosen thickness of about 0.3 times the mean free path length no artifacts related to the band gap measurements were observed for $KCa_2Nb_3O_{10}$.
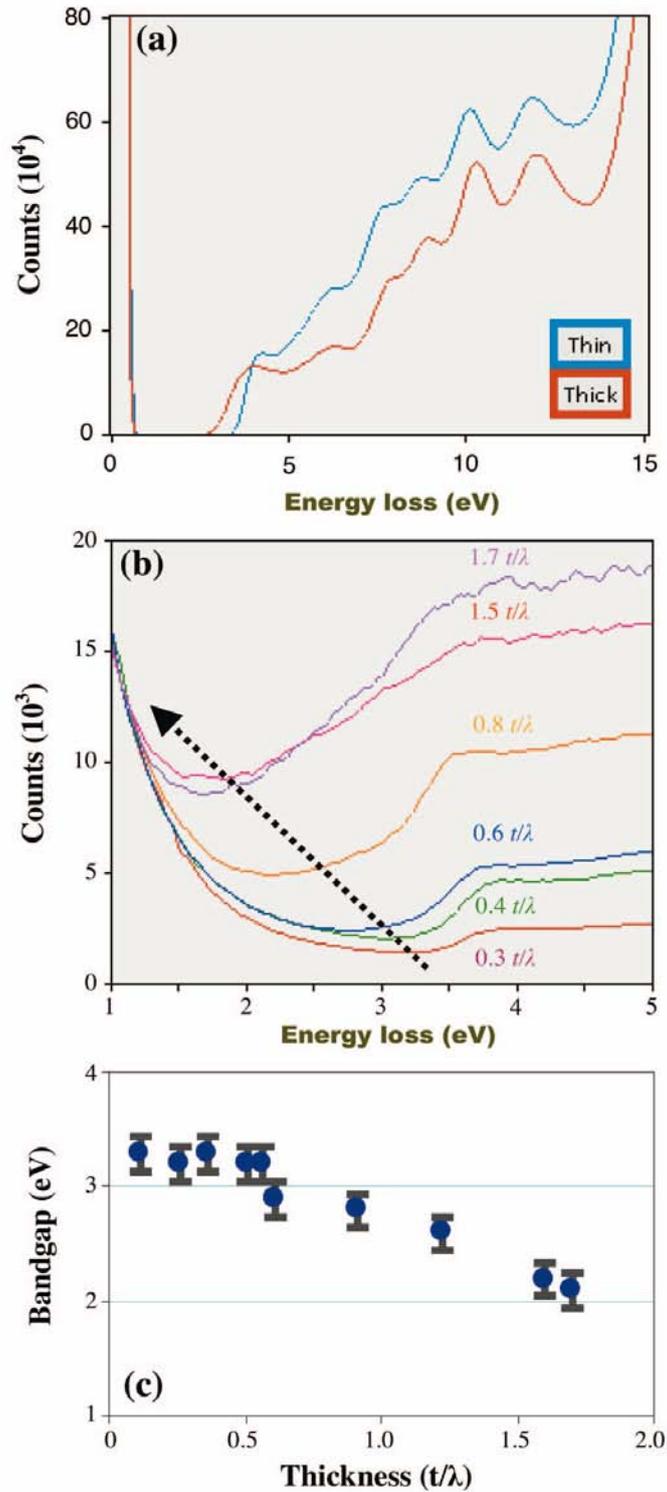
Figure 4.15: (a) VEEL spectra of *h*-GaN shows a lower onset when acquired from thicker regions, as quantitatively highlighted (t is the thickness and λ the mean free path length) in (b) which overall leads to incorrect identification of band gap (c) for thicknesses greater than 0.5 times the mean free path length. Figures (a), (b) and (c) are reproduced from Gu *et al.* Phys. Rev. B 75, 195214 with the permission of the American Physical Society, Maryland, US. Article available online at http://prb.aps.org/abstract/PRB/v75/i19/e195214.

Another parameter effecting the contribution of Cerenkov radiation is the collection angle. The angular variation of Cerenkov radiations had been first shown by von Festenberg [20,21]. He showed that Cerenkov radiation contributes significantly to the loss spectrum only at collection angles of the order 0.01 mrad. Subsequently Gu *et al.* had shown [3] the correctness of von Festenberg's [20,21] theory using better instrumentation. Gu *et al.* showed [3] that the Cerenkov radiation contribute significantly only at collection angles of about 20 µrad as is shown in Figure 4.16 (Reproduced from Ref. 3 with permission from the American Physical Society, © American Physical Society 2007). Therefore, as for the measurements on for $KCa_2Nb_3O_{10}$ a collection angle of 9.5 mrad was used, the chances of Cerenkov radiation interfering with the signal can safely be neglected.
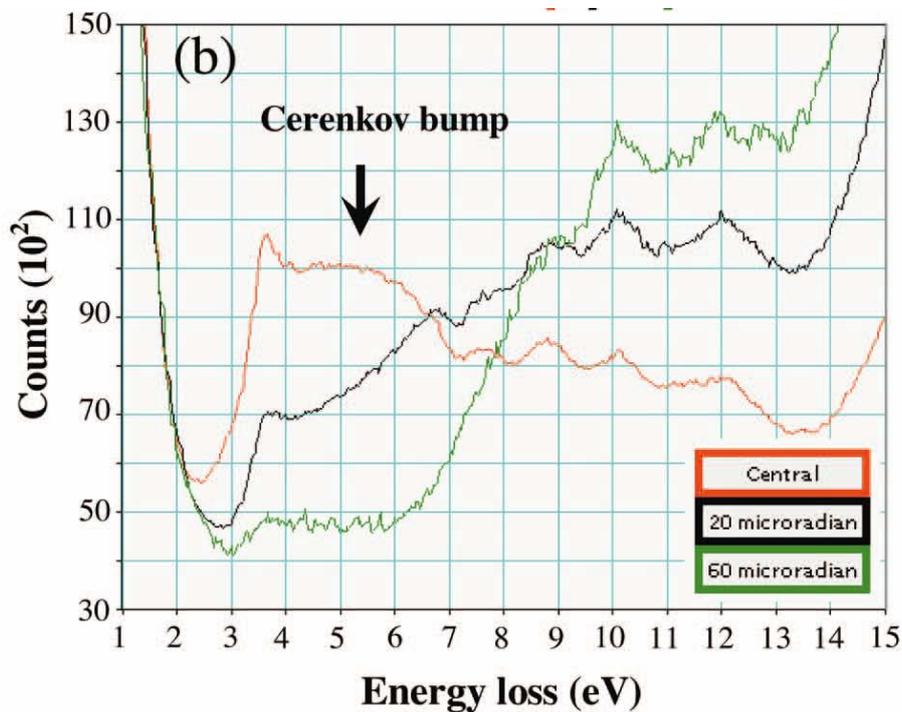


Figure 4.16: The angular variation of VEEL spectra acquired from *h*-GaN showing a bump due to Cerenkov radiation for collection angles up to 20 µrad. Figure reproduced from Gu *et al.* Phys. Rev. B 75, 195214 with the permission of the American Physical Society, Maryland, US. Article available online at http://prb.aps.org/abstract/PRB/v75/i19/e195214.

In light of these facts, it is worth emphasizing that the success in obtaining the band gap of $KCa_2Nb_3O_{10}$ from VEELS measurements reported in this work stems from the appropriate choice of collection angle and thickness.

The determination of onset of the conduction band visualized in the VEEL spectrum has rather been an open question in the scientific community. Rafferty and Brown [22] proposed

that in the loss function (VEELS), the conduction band onset for a direct band gap semiconductor should be of the form $I \sim (E\text{-}E_g)^{0.5}$ whereas for an indirect band gap semiconductor of the form $I \sim (E\text{-}E_g)^{1.5}$. Later Lazar *et al.* demonstrated [23] the applicability of this relation for the direct and indirect transitions in cubic-GaN (Figure 4.17a, Reproduced from Ref. 23 with permission from Elsevier Ltd. UK). The spectrum could be described with $I \sim (E\text{-}E_g)^{1.5}$ in the energy range 2-3.2 eV (indicating indirect transition) and with $I \sim (E\text{-}E_g)^{0.5}$ for direct band gap transition in momentum space in the enrgy range 3.2-5 eV. Park *et al.* later demonstrated [24] the possibility of using a linear-fit to the conduction band onset. The performed VEELS measurements (Section 3.2) do not indicate an onset of the form $I \sim (E\text{-}E_g)^{0.5}$ which would have an abrupt onset though DFT calculations indicate $KCa_2Nb_3O_{10}$ to be a direct band gap semiconductor. A linear fit to the onset, shown in Figure 4.17b approximately describes the nature of onset in $KCa_2Nb_3O_{10}$. A possible cause for divergence could be low density of states close to the band onset at 3.1 eV (as suggested by DFT calculations).
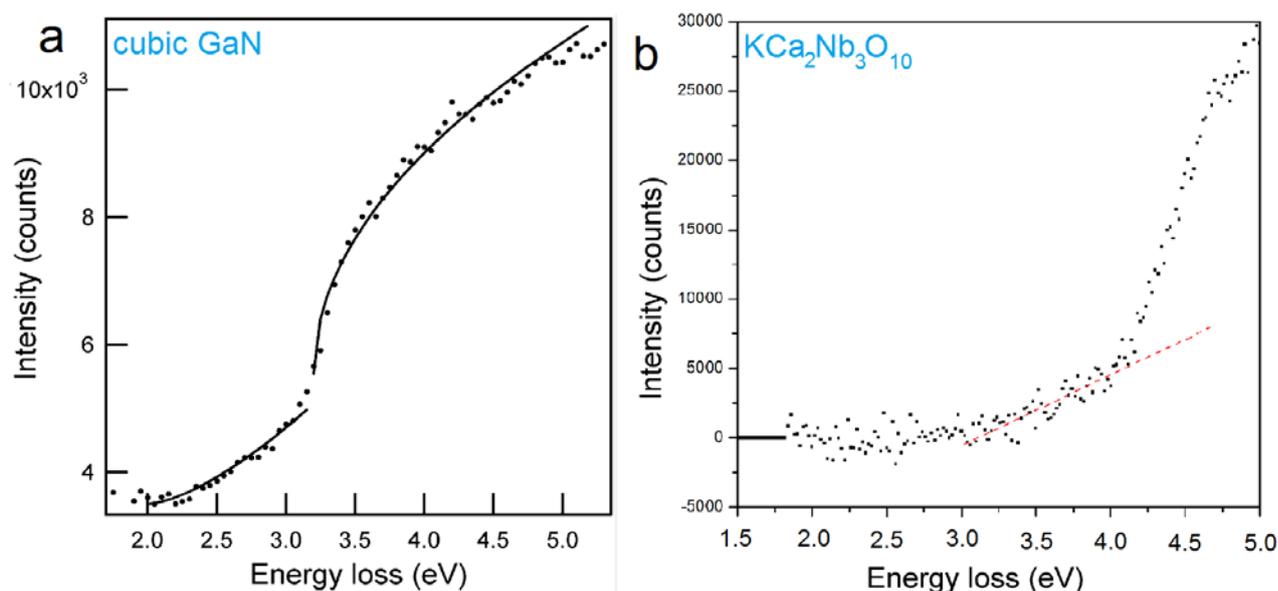


Figure 4.17: The ZLP subtracted VEELS showing the conduction band onset for (a) GaN [Reprinted from Lazar *et al.* Ultramicroscopy 96, 535 (2003) with permission from Elsevier Ltd. UK] and (b) $KCa_2Nb_3O_{10}$.

Gallegos-Orozoco and co-workers [25] used a computational methodology (APW+lo and PBE-GGA for exchange correlation effects) similar to this study on $KCa_2Nb_3O_{10}$ and achieved a general agreement between theoretical and experimental loss functions of ferroelectric and paraelectric $BaTiO_3$. However, in their study they were able to identify

plasmon excitations distinctly with the theoretical and experimental values while in this study, easy identification of plasmon is non-trivial. Morales-Rodriguez and Espinosa-Magana [26] used a TB-mBJ potential, like this work, however had more success in predicting the plasmon excitation of ZnO.

## 4.8 Summary

Experimental acquisition of VEELS requires ingenious choice of parameters like the acquisition time, spectrometer dispersion, collection angle etc. Acquiring the complete VEEL spectrum in one acquisition leads to high noise levels around the tail of ZLP, thereby increasing the margin of error in band gap determination. Acquiring two spectra, one containing the complete ZLP along with valence excitations, the other containing the tail of the ZLP with the valence loss excitations and splicing them together generates a better VEEL spectrum for band gap determination. Power-law function effectively describes the tails of the ZLP and upon subtraction allows for determination of the band gaps. The choice of energy window where the power-law function is defined is critical and choosing power-law function to describe a non-decaying signal can lead to erroneous band gap values. The conduction band onset can be effectively described by a straight line fit. STEM-VEELS allows for effectively determining the band gap of $KCa_2Nb_3O_{10}$ to be $3.2\pm0.1$ eV whereby the error is contributed primarily by the alignment procedure used. Computed and experimentally determined loss functions show good agreement in the energy range 0-20 eV. The available data does not allow for experimentally identifying the plasmon excitations. Core-loss EELS allows for conforming the chemical nature of $KCa_2Nb_3O_{10}$ as manifested by the EELS edges $Nb-M_{4,5}$, $K-L_{2,3}$, $Ca-L_{2,3}$, $Nb-M_{2,3}$ and O-K.

## 4.9 Chapter references

[1]     R. F. Egerton. *Electron Energy-Loss Spectroscopy in the Electron Microscope*. Springer Science + Business Media Inc. (2011)

[2]     V. Mauchamp, G. Hug, M. Bugnet, T. Cabioc'h, and M. Jaouen. Anisotropy of $Ti_2AlN$ dielectric response investigated by *ab initio* calculations and electron energy-loss spectroscopy. *Phys. Rev. B.*, 81, 035109 (2010)

[3]     L. Gu, V. Srot, W. Sigle, C. Koch, P. van Aken, F. Scholz, S. B. Thapa, C. Kirchner, M. Jetter, and M. Rühle. Band-gap measurements of direct and indirect semiconductors using monochromated electrons. *Phys. Rev. B.*, 75, 195214 (2007)

[4]     R. Arenal, O. Stephan, M. Kociak, D. Taverna, A. Loiseau, and C. Colliex. Electron energy loss spectroscopy measurement of the optical gaps on individual boron nitride single-walled and multiwalled nanotubes. *Phys. Rev. Lett.* 95, 127601 (2005)

[5]     K. Domen, J. Yoshimura, T. Sekine, A. Tanaka, and T. Onishi. A novel series of photocatalysts with ion-exchangeable layered structure of niobates. *Catalysis Lett.* 4, 339 (1990)

[6]     L. Zhang, S. Turner, F. Brosens, and J. Verbeeck. Model based determination of dielectric function by STEM low-loss EELS. *Phys. Rev. B.* 81, 035102 (2010)

[7]     R. Erni, and N. D. Browning. Quantification of size-dependent energy gap of individual CdSe quantum dots by valence electron energy-loss spectroscopy. *Ultramicroscopy*, 107, 267 (2007)

[8]     K. van Benthem, R. H. French, W. Sigle, C. Elsässer, and M. Rühle. Valence electron energy loss study of Fe-doped $SrTiO_3$ and a $\Sigma 13$ boundary : electronic structure and dispersion forces. *Ultramicroscopy* 86, 303 (2001)

[9]     K. van Benthem, C. Elsässer, and R. H. French. Bulk electronic structure of $SrTiO_3$: Experiment and theory. *J. Appl. Phys.* 90, 6156 (2001)

[10]    D. Bach, R. Schneider, D. Gerthsen, J. Verbeeck, and W. Sigle. EELS of niobium and niobium oxide phases- Part I: Plasmon and near edges fine structure. *Microsc. Microanal.* 15, 505 (2009)

[11]    K. S. Katti, M. Qian, D. W. Frech, and M. Sarikaya. Low-loss electron energy-loss spectroscopy and dielectric function of biological and geological polymorphs of $CaCO_3$. *Microsc. Microanal.* 5, 358 (1999)

[12]    C. C. Ahn, A. L. Krivanek, R. P. Burgner, M. M. Disko, and P. R. Swann. *EELS Atlas,* HR-EM Facility, Arizona State University, Tempe, Arizona, US (1983)

[13]    M. Arai, S. Kohiki, H. Yokishawa, S. Fukushima, Y. Waseda, and M. Oku. Photoelectron energy-loss functions of $SrTiO_3$, $BaTiO_3$ and $TiO_2$: Theory and experiment. *Phys. Rev. B* 65, 085101 (2002)

[14] T. Miyake, P. Zhang, M. L. Cohen, and S. G. Louie. Quasiparticle energy of semicore *d* electrons in ZnS: Combined LDA+U and GW approach. *Phys. Rev. B* 74, 245213 (2006)

[15] S. Hedrich, H. Lünsdorf, R. Kleeberg, G. Heide, J. Seifert, and M. Schlömann. Schwertmannite formation adjacent to bacterial cells in a mine water treatment plant and in pure cultures of *ferrovum myxofacien. Env. Sci. Tech.* 45, 7685 (2011)

[16] K. A. Mkhoyan, J. Silcox, A. Ellison, D. Ast, and R. Dieckmann. Full recovery of electron damage in glass at ambient temperatures. *Phys. Rev. Lett.* 96, 205506 (2006)

[17] K. Kimoto, G. Kothleitner, W. Grogger, Y. Matsui, and F. Hofer. Advantages of monochromator for bandgap measurements using electron energy-loss spectroscopy. *Micron* 36, 185 (2005).

[18] M. Stöger-Pollach and P. Schattschneider. The influence of relativistic energy losses on band gap determination using valence EELS. *Ultramicroscopy* 107, 1178 (2007)

[19] T. Kuykendall, P. Ulrich, S. Aaloni, and P. Yang. Complete composition tunability of InGaN nanowires using a combinatorical approach. *Nat. Mat.* 6, 951 (2007)

[20] C. von Festenberg. Retardierungseffekte in Energieverlustspektrum von GaP. *Z. Phys.* 214, 464 (1968)

[21] C. von Festenberg. Energieverlustmessungen an III-V-Verbindungen. *Z. Phys.* 227, 453 (1969)

[22] B. Rafferty and L. M. Brown. Direct and indirect transitions in the region of the band gap using electron-energy loss spectroscopy. *Phys. Rev. B.* 58, 10326 (1998)

[23] S. Lazar, G. A. Botton, M.-Y. Wu, F. D. Tichelaar, and H. W. Zandbergen. Materials science applications of HREELS in near edge structure analysis and low-energy loss spectroscopy. *Ultramicroscopy* 96, 535 (2003)

[24] J. Park, S. Heo, J. Chung, H. Kim, H. Lee, K. Kim, and G. Park. Bandgap measurements on thin dielectric films using monochromated STEM-EELS. *Ultramicroscopy* 109, 1183 (2009)

[25]   V. Gallegos-Orozco, R. Martinez-Sanchez, and F. Espinosa-Magana. *In situ* characterization of the ferroelectric transitions in $BaTiO_3$ by EELS and comparison with *ab intio* methods. *Phys. Rev. B.* 77, 045128 (2008)

[26]   H. J. Morales-Rodriguez and F. Espinosa-Magana. Experimental and theoretical determination of the low-loss electron energy loss spectroscopy of nanostructured ZnO. *Micron* 43, 177 (2012)

# 5    Structure and properties of calcium niobate perovskite nanosheets

Since the discovery of graphene [1] by Novoselov and co-workers, considerable attention has been paid by the scientific community to the synthesis, characterization and properties of such two-dimensional (2D) structures. In addition to the significant success in physical and chemical synthesis of graphene, scientists have been able to replicate the success in synthesizing other families of 2D-structures. 2D-nanostructures based on oxides [2], boron nitride [3], metal dichalcongenides [4] and metal disulphides [5] have been synthesized. One family of 2D-nanosheets that has attracted considerable attention is the exfoliated calcium niobate perovskite based nanosheets [6]. These nanosheets have been synthesized by delamination of the Dion-Jacobson perovskite $KCa_2Nb_3O_{10}$ [7] and has been purported to be an ideal candidate for nanoelectronics as a dielectric material [8]. These exfoliated nanosheets have a hybrid structure, given by the chemical formula of $[TBA_xH_{1-x}]^+[Ca_2Nb_3O_{10}]^-$ whereby a central inorganic anionic layer of $[Ca_2Nb_3O_{10}]^-$ is surrounded by the organic ligand tetra-*n*-butylammonium ions ($TBA^+$) and hydrogen ions.

This chapter entails the results on the $[TBA_xH_{1-x}]^+[Ca_2Nb_3O_{10}]^-$ hybrid-nanosheets using electron microscopy, atomic force microscopy and electron energy loss spectroscopy that help in understanding the very basic properties of these hybrid-nanosheets like the structure, crystallinity, band gap etc. Also described in detail is the methodology developed for acquisition and processing of VEELS data from nanostructures. The synthesis of these nanosheets was carried out by Pirmin Ganter and Christian Ziegler under the supervision of Prof. Bettina Lotsch. The details of synthesis have been published previously in the Bachelor's thesis of Pirmin Ganter [9]. The AFM measurements shown here were performed by Christian Ziegler. Findings presented in this chapter have in part been compiled into a paper entitled, "Extracting band gaps from hybrid two-dimensional nanostructures in the nanometer domain" and shall be sent to *Nano Letters*. All measurements (other than the AFM measurement) elaborated here were performed with Yaron Kauffmann, Department of Materials Science and Engineering, Technion - Israel Institute of Technology.

# 5.1 Synthesis of nanosheets

The bulk $KCa_2Nb_3O_{10}$ synthesis was carried out in a way similar to that proposed by Jacobson and co-workers [7]. Stoichiometric mixture of commercially available $K_2CO_3$, $CaCO_3$ and $Nb_2O_5$ with 10% molar excess of $K_2CO_3$ was ground. After thoroughly mixing, the mixture was fired to a temperature of 1200°C and kept at this temperature for 60 hours. For synthesizing the nanosheets, an approach similar to that of Ebina and co-workers [10] was followed. 1 g of $KCa_2Nb_3O_{10}$ was treated with 5 M $HNO_3$ (40 cm$^3$) for four days whereby the acid was daily renewed culminating in the conversion into the protonic oxide $HCa_2Nb_3O_{10} \cdot 1.5H_2O$ which was recovered by filtration. For exfoliation, 0.2 g of $HCa_2Nb_3O_{10} \cdot 1.5H_2O$ was dispersed in 50cm$^3$ tetra-*n*-butylammonium hydroxide 30-hydrate aqueous solution at a molar ratio 1:1. The solution was shaken for four weeks and non-dispersed solid removed with centrifugation at 3000 rmp. Inductively coupled plasma – atomic emission spectroscopy was performed to obtain the chemical composition $[TBA_xH_{1-x}]^+[Ca_2Nb_3O_{10}]^-$ with *x≈0.8*.

# 5.2 STEM as a complimentary characterization tool to AFM for nanosheets

AFM has been used widely for characterizing 2D structures [1,2,4,6], obtaining their heights and characterizing regions of multiple stacks on the basis of their thickness. A similar procedure was followed for characterizing the $[TBA_xH_{1-x}]^+[Ca_2Nb_3O_{10}]^-$ hybrid nanosheets. A diluted suspension of nanosheets was allowed to dry on a silicon substrate and studied using an Asylum MFP-3D Stand Alone AFM (Asylum Research, Santa Barbara, California, US) equipped with a Si micro-cantilever (300 Hz resonant frequency and 26.1 N/m spring constant). An AFM image acquired from the diluted $[TBA_xH_{1-x}]^+[Ca_2Nb_3O_{10}]^-$ hybrid nanosheets dispersed on Si-substrate is shown in Figure 5.1a. The nanosheets have a size ranging from a few hundred nanometers up till a few microns. At certain regions the sheets stack up. The height profile (Figure 5.1b) acquired along the arrow shown in the AFM image (Figure 5.1a) suggests the height of a single sheet to be 3.4 nm and in a stack, the height jump for each subsequent sheets to be ~ 2.9 nm.

a



b
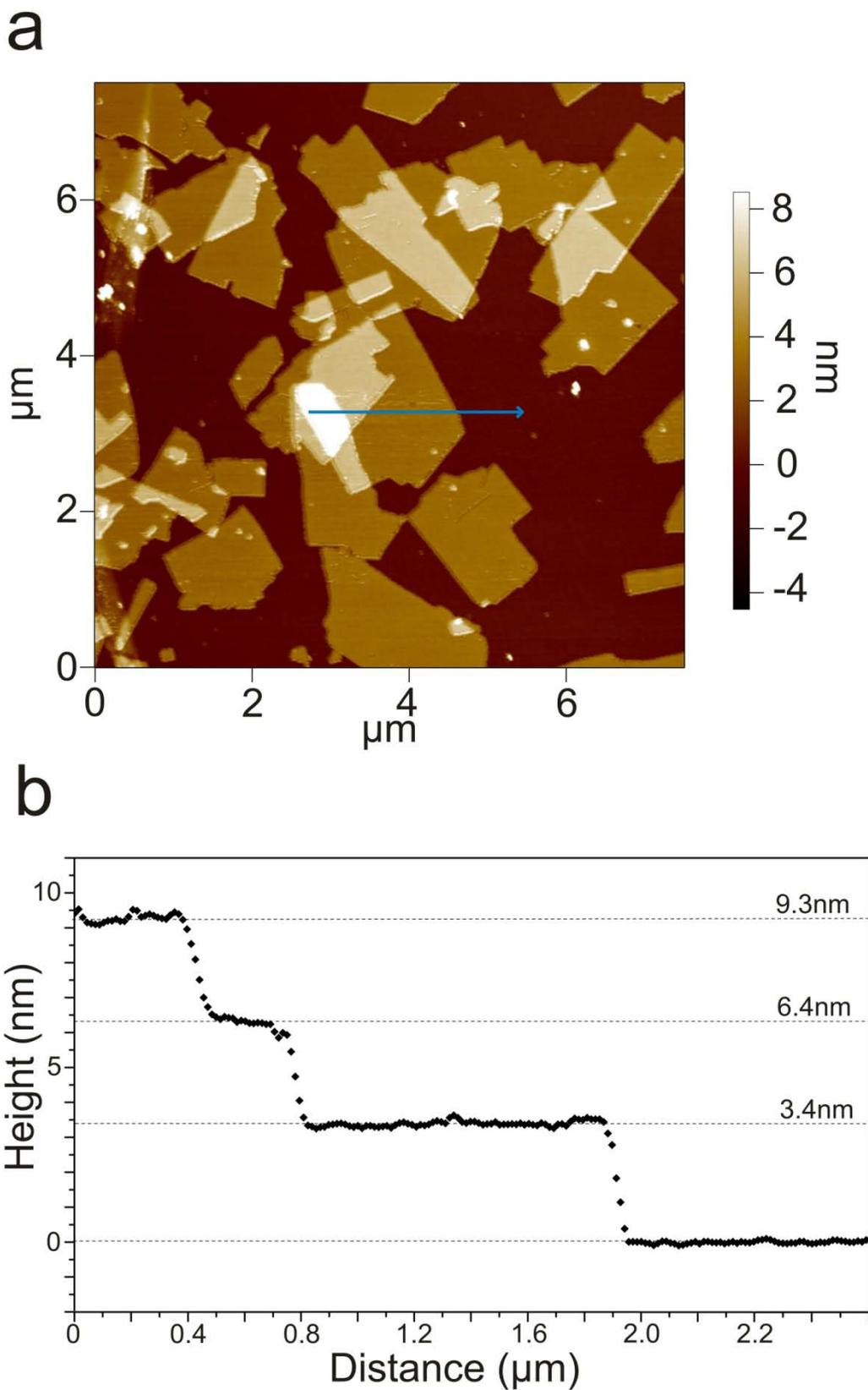


Figure 5.1: AFM image (a) of $[TBA_xH_{1-x}]^+[Ca_2Nb_3O_{10}]^-$ nanosheets and the height profile (b) measured along the arrow shown in (a). Measurements performed by Christian Ziegler, Department of Chemistry, Ludwig-Maximilians University.

Previously Sabio and co-workers utilized high angular annular dark field (HAADF) STEM to characterize metal and metal nanoparticle loaded $[TBA_xH_{1-x}]^+[Ca_2Nb_3O_{10}]^-$ nanosheets [11]. The nanosheets, when deposited on a surface and left to dry form stacks with limited interaction between the sheets.

For electron microscopy investigations, the nanosheets suspension was diluted, drop coated onto a lacey-C coated copper grid and dried. Imaging the $[TBA_xH_{1-x}]^+[Ca_2Nb_3O_{10}]^-$ nanosheets depicted a picture similar to that generated by AFM measurements. The HAADF-STEM image acquired (Figure 4.2a) showed the existence of sheets in the size range a few hundred nm up to a few microns. In the HAADF-STEM mode, the intensities observed can be related to the atomic number and the thickness [12]. The dark regions are categorized as vacuum. This hypothesis was tested by acquiring EELS from this region and it showed no signal above the noise level thereby indicating absence of any matter in these regions. Intensity profile (Figure 5.2b) acquired along the arrow shown in Figure 5.2a showed quantum jumps along the arrow as it traversed from vacuum to thicker regions. The quantum jumps further supported the evidence for existence of nanosheets stacked in some region one above another. On the basis of intensity, the regions can be classified as vacuum, individual single sheet, double sheet and triple sheet as shown in Figure 5.2a. In the double and triple sheets regions, two and three sheets stack one above the other.

The intensity profile (Figure 5.2b) shows a first quantum jump of about 7700 counts and the subsequent two jumps of ~ 6000 counts each. This conforms to the height profile measured by AFM (Figure 5.1b) whereby the first jump in height (3.4 nm) is greater than the subsequent jumps (~2.9 nm). These two measurements indicate that the ligand layer in between two $[Ca_2Nb_3O_{10}]^-$ layers rearranges itself into a more close packed assembly. Despite the success of HAADF-STEM in determining the relative thickness of regions, absolute thickness measurement like in an AFM is however not possible. Quantifying the intensity in HAADF-STEM image to absolute thickness is a tedious process, which become even more complicated for a hybrid material like $[TBA_xH_{1-x}]^+[Ca_2Nb_3O_{10}]^-$ nanosheets. Therefore, quantification of absolute thickness from HAADF-STEM measurements is not attempted in this work.

To conclude, the applicability of HAADF-STEM for efficiently identifying regions of single sheet or multiple sheets in a stack is demonstrated as a complimentary tool to AFM. This is of importance as it allows for, in a TEM, identification of regions containing freely suspended

individual sheets. Accordingly their structure can be studied. Performing spectroscopy experiments allow for understanding the electronic and chemical nature of these sheets.
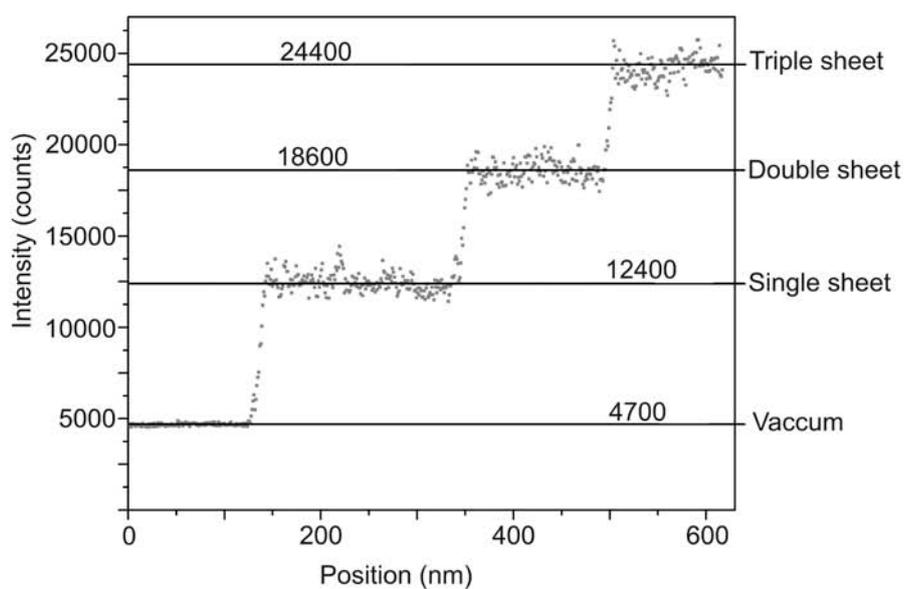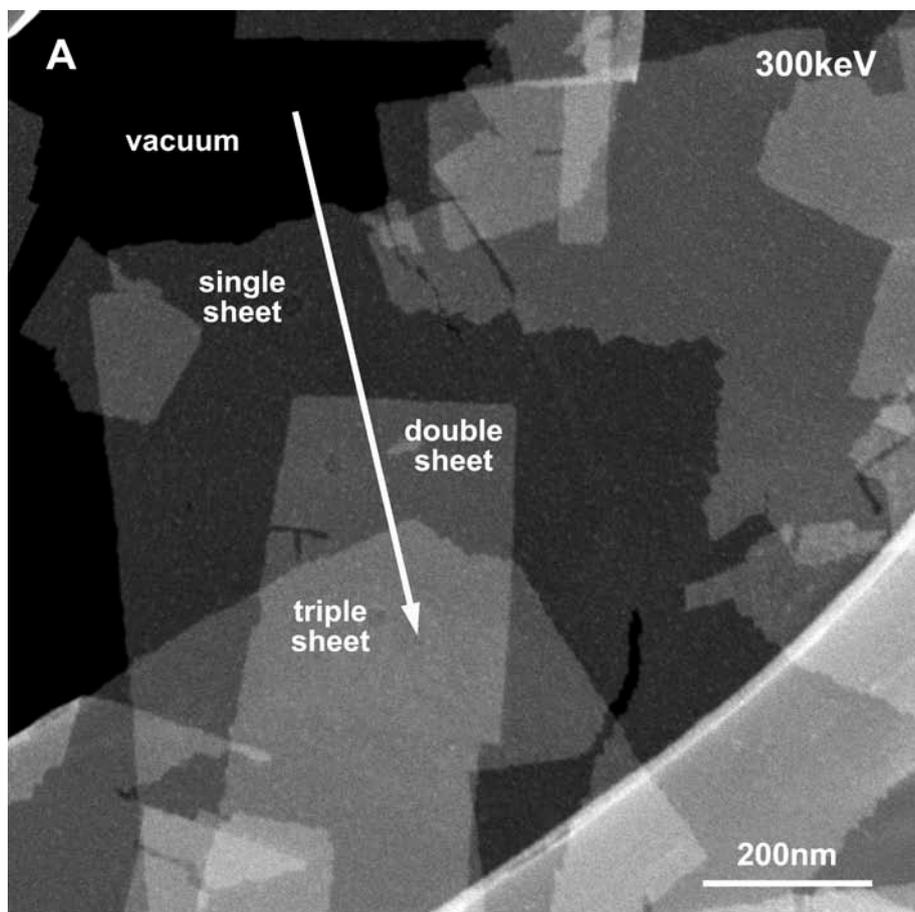


Figure 5.2: HAADF-STEM image (a) of $[TBA_xH_{1-x}]^+[Ca_2Nb_3O_{10}]^-$ nanosheets and the intensity profile (b) along the arrow shown in (a).

85

## 5.3 HR-TEM imaging of $[TBA_xH_{1-x}]^+[Ca_2Nb_3O_{10}]^-$ nanosheets

Despite the wealth of information that AFM and HAADF-STEM provide, one still has limited idea about the crystallinity of the nanosheets. Under ideal cases performing HAADF-STEM at high resolution can allow for determining the crystalline nature of the nanosheets however, the prolonged exposure under a convergent beam with a small probe can lead to loss of crystallinity. It is worth pointing out that imaging the sheets at high resolution in HAADF-STEM mode is not impossible, as has been demonstrated by Sabio and co-workers [11], however it is arduous. HR-TEM on the contrary provides for an easier way to study the crystalline nature of nanosheets. This is because the HR-TEM utilizes a parallel beam to illuminate the sample, thereby decreasing the beam current experienced by the sample.

HR-TEM images were acquired using an FEI-TITAN 80-300 scanning transmission electron microscope equipped with an aberration (Cs) corrector. HR-TEM image acquired from a single sheet is displayed in Figure 5.3 in the [100] zone axis. It reveals high crystallinity, as exemplified by the FFT shown in inset. In particular, it is worth noting that the nanosheet is single crystalline in nature. The interplanar distance observed in the HR-TEM image (Figure 4.3) ~ 3.9Å matches well with the in-plane (parallel to *bc* plane) crystallographic Nb-Nb distances of 3.93 and 3.86 Å. The crystallinity observed can be attributed to the $[Ca_2Nb_3O_{10}]^-$ layer in the nanosheet. The $[TBA_xH_{1-x}]^+$ layers on the contrary would consists of ligands not bound to specific positions.

HR-TEM image acquired from a double sheet region and its FFT shown in inset (Figure 5.4) displays a Moiré pattern, indicating the two crystals, slightly rotated with respect to each other. Several Moiré patterns were observed in the experiments performed such that no preferential direction or orientation exists in which the sheets stack upon one another, thereby indicating limited interaction between the sheets.
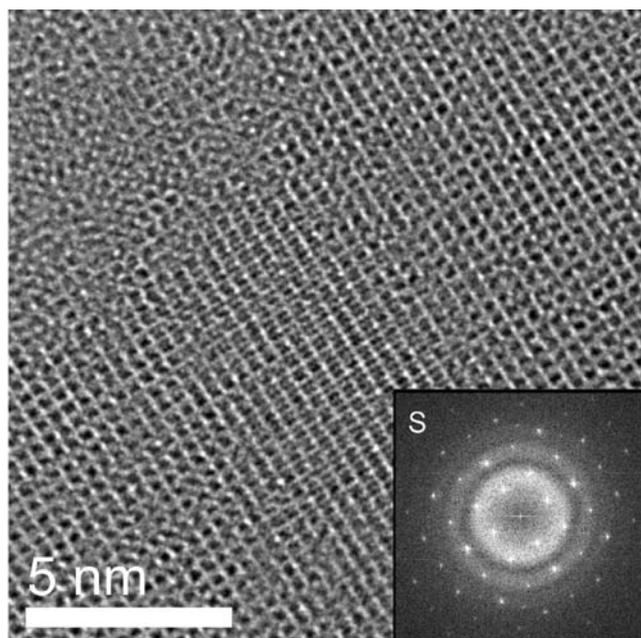
Figure 5.3: HR-TEM image acquired from a single sheet region and its FFT shown in inset.
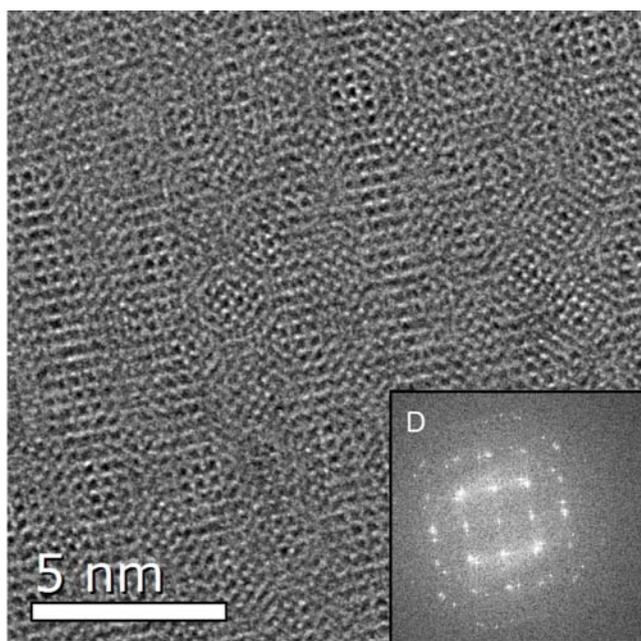


Figure 5.4: HR-TEM image acquired from a double sheet region and its FFT shown in inset.

## 5.4 Acquisition of VEELS from $[TBA_xH_{1-x}]^+[Ca_2Nb_3O_{10}]^-$ nanosheets

Acquisition of VEELS from hybrid nanosheets requires special care. Nanostructures disintegrate under irradiation of high energy electrons. Hence, it is necessary to understand the decay dynamics of the nanosheets before performing comprehensive sets of measurements. To study the decay mechanism, fifty spectra were acquired (in the energy loss region 2-42 eV) from a single sheet region when exposed to a stationary spot in STEM mode

of size ~1 nm. The spectra were acquired at a rate of one spectrum per second. The first, fifth, tenth, fifteenth, twentieth, thirtieth, fortieth and the fiftieth spectra are shown in Figure 5.5.
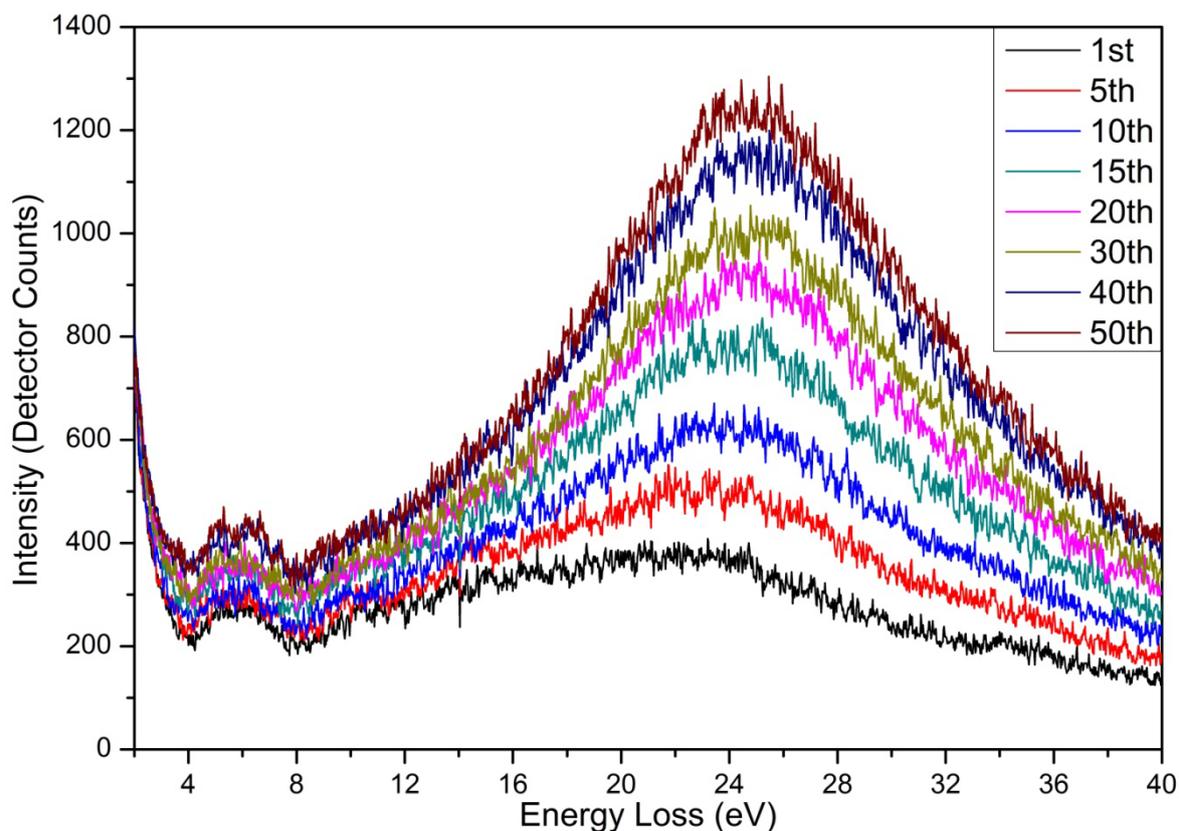


Figure 5.5: VEEL spectra acquired one, five, ten, fifteen, twenty, thirty, forty and fifty seconds after irradiation.

The disintegration of the nanosheet is manifested by the constant temporal accretion of the intensity in the low-loss region. The increase in intensity can be attributed to accumulation of carbonaceous contaminants on the sample area exposed, which is a common problem with convergent beam electron beams [13]. In addition, the plasmon position shifts to higher energy value as the sheet gets damaged and contaminated. Imaging of irradiated areas indicated the loss of crystallinity. In the spectra acquired, one can see that the change in the spectra acquired in the first five seconds is inconspicuous, especially in the low energy range ($E<8$ eV) which is preeminent for band gap extraction.

The areas were imaged in HAADF-STEM mode to further understand the decay mechanism at low magnification, so that the imaging did not cause any damage to the nanosheet. The area imaged after irradiation is shown in Figure 5.6. The spots 1, 2, 3, 4, 5 and 6 were irradiated under the electron beam for five, ten, twenty, thirty, forty and fifty seconds respectively. Clearly there is negligible damage at and around spot 1. Damage or contamination is hard to

discern at spot 2 too. At spots 3 and 4 a clear hole is visible around the point of irradiation on the sheet. In the case of spots 5 and 6 damage is visible, however a clear hole is hard to discern at the magnification the image was acquired at. Degradation manifested by a faint halo around these spots is visible. A possible explanation could be the accumulation of carbonaceous species on the areas irradiated for a longer period [13].
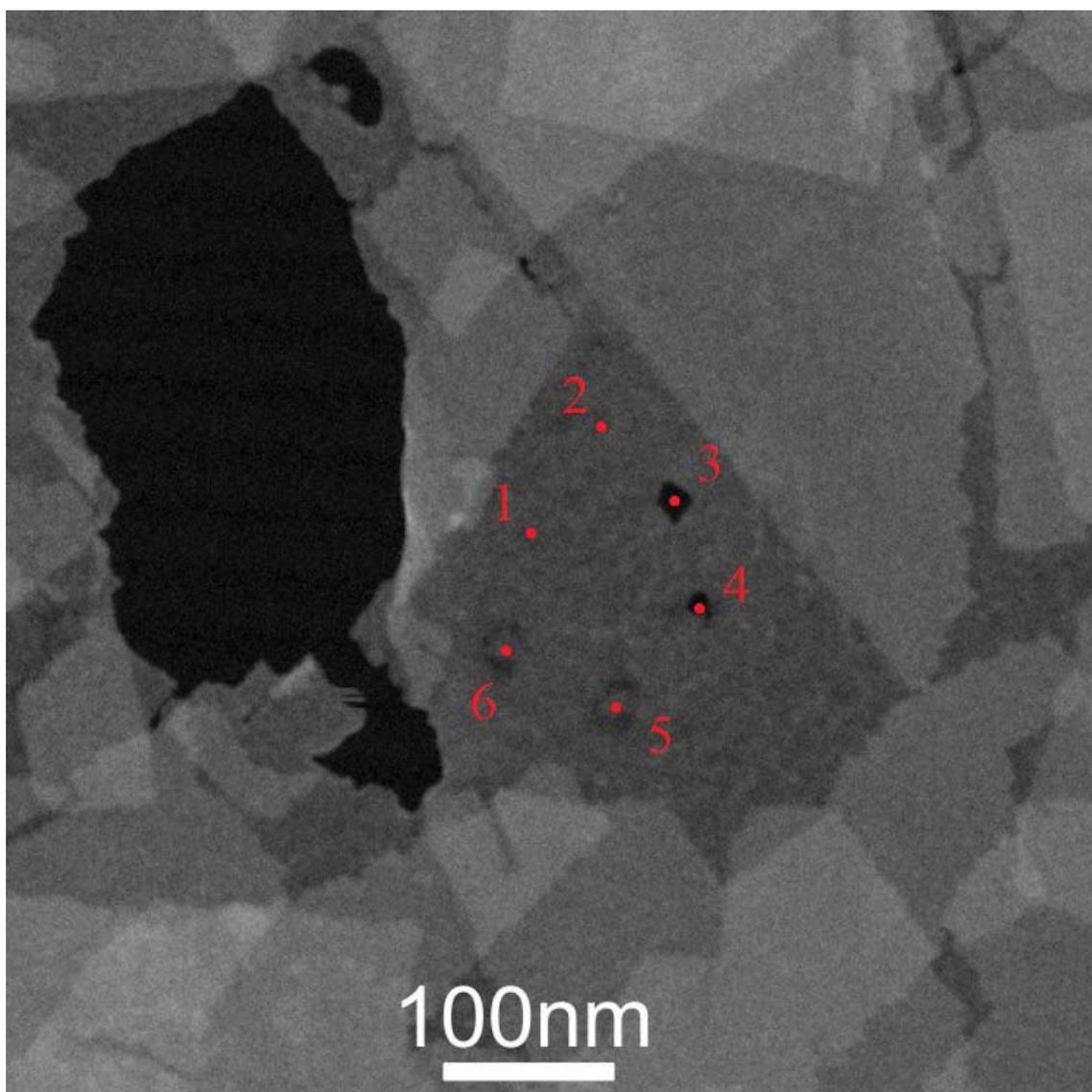


Figure 5.6: HAADF-STEM image acquired from a single sheet region where points 1, 2, 3, 4, 5 and 6 were irradiated for five, ten, twenty, thirty, forty and fifty seconds respectively.

In light of these measurements it is safe to assume that the sample undergoes negligible beam damage in the first five seconds of irradiation. Hence for all subsequent analyses spectra were acquired within first five seconds of irradiation at the rate of one acquisition per second with acquisition time per acquire varying from 0.01 s to 0.64 s. The five acquired spectra were added to generate a single spectrum.

VEEL spectrum spanning the energy-loss range -5 to 35 eV acquired from a single sheet region is shown in Figure 5.7 using an acquisition time of 0.01 s per acquisition and one acquisition per second. The predominant feature visible is the ZLP at a $E=0$ eV. The scattering cross-section due to the valence electron excitations is hardly discernible in the spectrum. Upon a closer look by looking at intensities three orders of magnitude less than that of the ZLP the valence loss excitations can be visualized (inset Figure 5.7) albeit the high level of noise makes extraction of band gaps implausible. This high level of noise emanates from the fact that for a very thin sample (nanostructure) the scattering-cross section is very low, thereby the difference in intensity between the ZLP and the valence loss excitations is huge (three orders of magnitude in this case) giving out a high level of noise which is related to the dynamic range of detector. Longer read-out times per spectrum are hindered by the dynamical range of detector (64,000 counts) without saturating the ZLP. Therefore, for obtaining better SNR a two step approach is necessary where another spectrum is acquired containing the tail of the ZLP and the valence loss excitations.
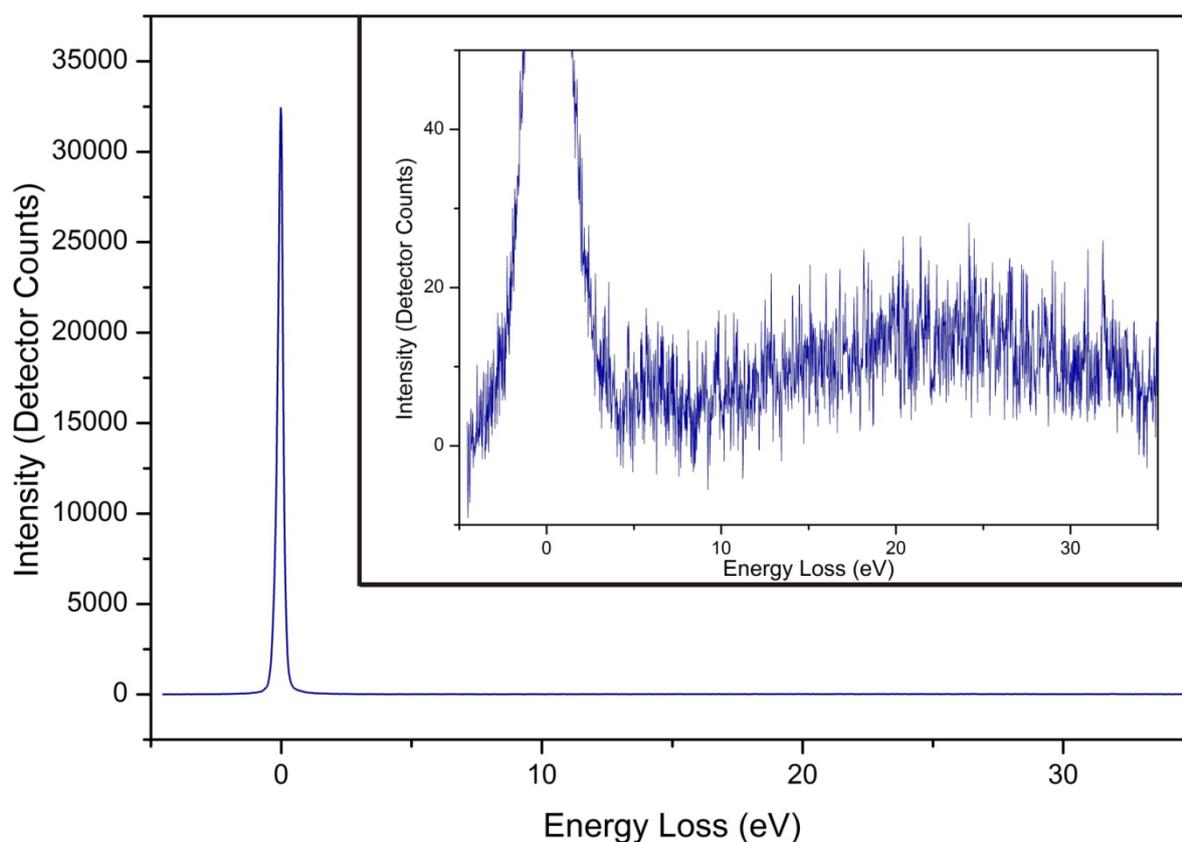


Figure 5.7: VEEL spectrum acquired from a single sheet showing a dominant ZLP and valence loss excitations (inset) having intensity three orders of magnitude less than that of the ZLP.

From the acquired loss spectrum with high noise, the position of the plasmon excitation was determined, by performing the measurement fifteen times. This resulted in determination of position of plasmon excitation within an error of ±0.2 eV. Then, another five spectra were acquired from the single sheet region within five second of irradiation with an acquisition time of 0.64 s per acquire. One such spectrum is shown in Figure 5.8. The five spectra were summed to get a single spectrum and calibrated according to the position of plasmon determined previously.

This methodology of acquiring multiple spectra and summing them up was used because of the fact that the frequency of AC mains interferes with the electromagnetic fields generated, leading to disturbances (for details see section 4.7). Aligning the acquired spectra and summing them up overcomes this obstacle to some extent depending on the acquisition times used.
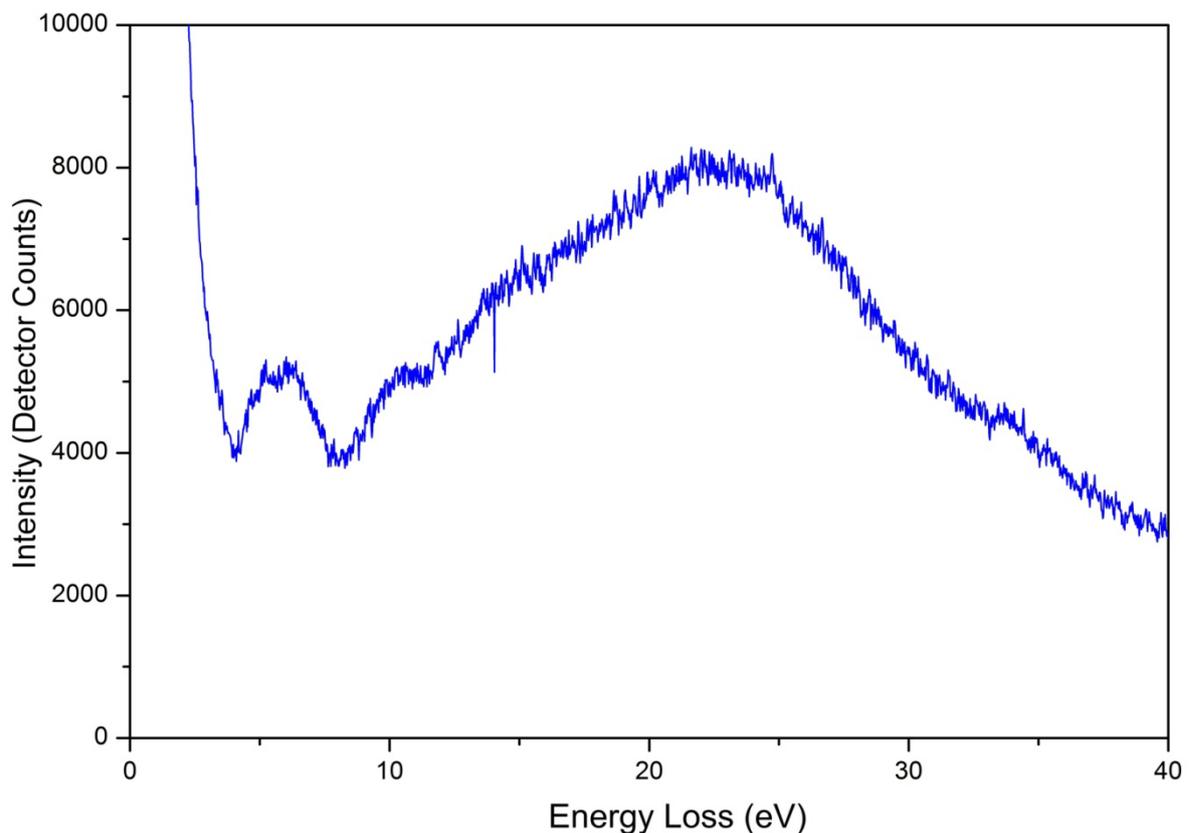


Figure 5.8: The VEEL spectrum acquired from a single sheet showing the valence excitations with a better SNR.

This procedure was reiterated for double sheet and triple sheet. These acquired spectra were used for band gap determination.

## 5.5 Band gap of individual free standing nanosheet

To obtain the band gap of the nanosheets, the contribution of the ZLP from the valence loss excitations needs to be deducted. As has been previously used by other scientists [14-16], a Power-law function can be used to describe the tail of the ZLP and can be subtracted to get the VEELS void of elastic scattering events. Hence, power-law based function was used to describe and subtract the tail of the ZLP to get the valence loss excitations. The VEEL spectrum acquired from the single, double and triple sheets is shown in Figure 5.9a along with the ZLP subtracted VEEL spectrum of $KCa_2Nb_3O_{10}$ (Figure 5.9b).
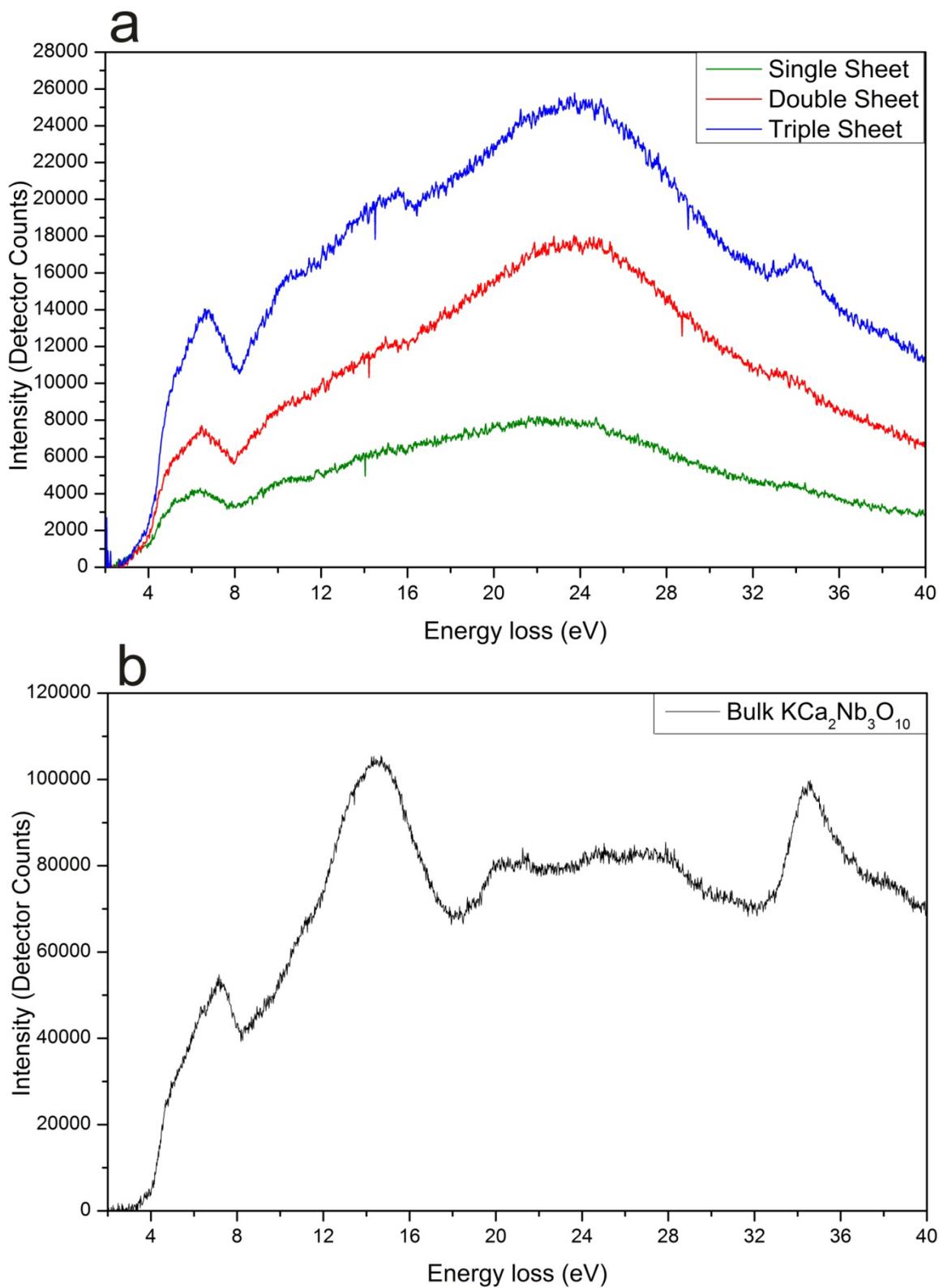
Figure 5.9: The ZLP subtracted VEEL spectrum obtained from a single, double and triple sheet (a) and that from bulk $KCa_2Nb_3O_{10}$ (b).

The ZLP subtracted VEEL spectrum of single, double and triple sheet regions show a common onset above the noise level at 2.9 eV. Taking into account the uncertainty in the alignment procedure of ±0.2 eV, the band gap of $[TBA_xH_{1-x}]^+[Ca_2Nb_3O_{10}]^-$ nanosheets can be determined to be 2.9±0.2 eV. Importantly, the measurements demonstrate that the conduction band onset is independent of the number of sheets probed for this family of calcium niobate nanosheets. The band gap of bulk $KCa_2Nb_3O_{10}$ determined by VEELS measurements (3.2±0.1 eV) and DFT calculations (3.1 eV) when observed in light of the band gap of nanosheets 2.9±0.2 eV suggested that the band gap remains invariant within the range of experimental error when $KCa_2Nb_3O_{10}$ is exfoliated into $[TBA_xH_{1-x}]^+[Ca_2Nb_3O_{10}]^-$ nanosheets.

Despite the use of a highly localized probe (~1nm) for acquiring the VEELS from nanosheets, the spatial resolution obtained for these measurements is not as good. This originates partly because of the fact that the valence electrons are delocalized and as such are able to respond to an electromagnetic field at certain distances. There are two ways of understanding this delocalization process by quantifying the extent of delocalization contributing to the valence electron transitions. The first, proposed by Krivanek and co-workers [17] described the radius of maximum delocalization $\Delta x_{max}$ for excitations at energy loss $E$ as given in Equation 5.1

$$\Delta x_{max} \sim \left(\frac{\hbar}{E}\right)\sqrt{\frac{2E_0}{m_e}} \qquad (5.1)$$

where $\hbar$ is the Planck's constant divided by $2\pi$, $E_0$ the energy of the primary electrons and $m_e$ the rest mass of the electron. Using this criteria the maximum extent of delocalization $\Delta x_{max}$ for the band gap transition of 2.9 eV can be calculated to be about 74 nm.

Egerton [18] came up with a different way of describing the extent of delocalization. He reasoned [18] that the majority of excitations occur closer to the point of irradiation, hence an description of the maximum extent of delocalization carries limited practical significance. He proposed that a better way of describing the delocalization of excitations is in terms of parameter $d_{50}$ such that 50% of the excitations occur within a diameter of $d_{50}$ with the centre of the circle being the point of irradiation. The $d_{50}$ can be defined as given in Equation 5.2

$$d_{50} \sim 0.8\,\lambda_e \left[\frac{E_0}{E}\right]^{3/4} \qquad (5.2)$$

where $E_0$ is the energy of the primary electrons, $E$ the energy at which the excitation occurs and $\lambda_e$ the wavelength of the electrons. Utilizing this expression $d_{50}$ is determined to be about 9 nm.

Determination of band gaps from VEELS is complicated and contains pitfalls [19] which necessitate thorough analysis of procedures. One major problem is the excitation of Cerenkov radiations [14,19], which can overlap with the conduction band onset thereby obscuring the identification of conduction band onset. Typically Cerenkov radiations contribute significantly to scattering cross section when either the sample probed is thick (more than 0.6 times the mean free path length of electrons in that material) or when a collection angle of a few micro radians is used [14]. The measurements performed on sheets were on sheets a few nm in thickness whereas the mean free path length for $KCa_2Nb_3O_{10}$ is approximately 140 nm [20]. In addition a collection angle of 9.5 mrads was used. On account of such choice of parameters, one can safely conclude that the Cerenkov radiations did not interfere with the band gap measurements.

Surface plasmon is a collective excitation mode of the valence electrons of a material at the surface [21]. It has also been reported to be a hindrance to determination of band gaps [22] in a TEM especially for nanostructures where the relative scattering cross-section for surface plasmons is considerably higher [22,23]. An adroit way of determining [24] the contribution of surface plasmons to a loss spectrum is the aloof beam excitation [25-27] whereby a converged electron beam is positioned very close (~1nm) to the edge of the material. Under these conditions the excitation of surface plasmons is enhanced and hence making it easier to identify them. When aloof beam excitation was employed for $[TBA_xH_{1-x}]^+[Ca_2Nb_3O_{10}]^-$ nanosheets, negligible signal above the noise level was observed (Figure 5.10).
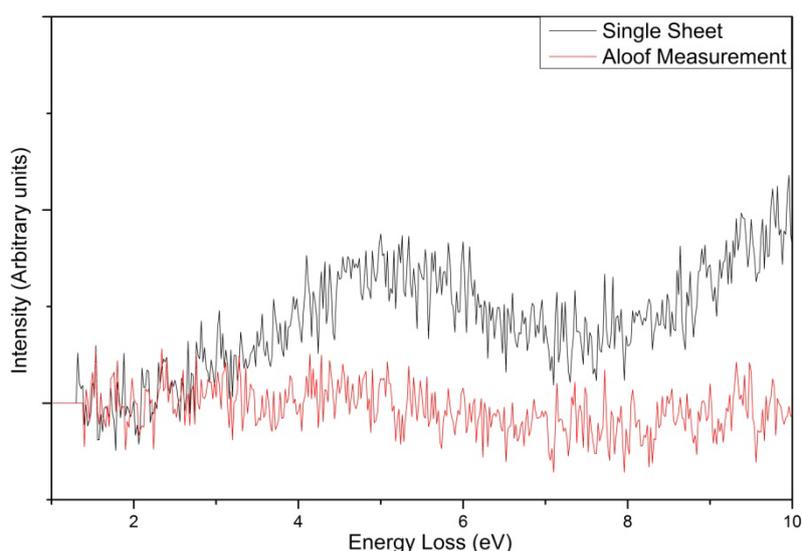


Figure 5.10: The VEEL spectrum for a single sheet (black) and for a single sheet in aloof beam condition (red).

A possible reason for the negligible signal in aloof beam condition is the vibrations caused in the loosely bound ligands $[TBA]^+$ to the dynamic electromagnetic field due to the convergent electron beam. Determining the exact cause for it is deemed peripheral to the context of the present study and as such is not further investigated.

## 5.6 Valence Excitations in $[TBA_xH_{1-x}]^+[Ca_2Nb_3O_{10}]^-$ nanosheets

The VEEL spectrum of $KCa_2Nb_3O_{10}$ and $[TBA_xH_{1-x}]^+[Ca_2Nb_3O_{10}]^-$ nanosheets shown in Figure 5.9 illustrates the similarities between the electronic structure of the two material families. The single excitations in both cases resemble significantly especially in the energy range *E<8* eV thereby implying similarities in the valence and conduction bands of these two materials. In the case of nanosheets (Figure 5.9a) the scattering cross-section for the valence excitations increases monotonically as one moves from single sheet to double and triple sheets. The Ca-$M_{2,3}$ edge at 34 eV [28] becomes more prominent in the VEEL spectrum from triple sheet while in the VEEL spectrum of $KCa_2Nb_3O_{10}$ it is palpable.

The predominant difference between the two structures is the broad plasmon excitation in the case of nanosheets in the energy range 16-30eV whereas in the case of $KCa_2Nb_3O_{10}$ a valley is observed in the above mentioned energy range. It is possible that $KCa_2Nb_3O_{10}$ has a broad multiple plasmon in this energy range like $Nb_2O_5$ [29]. Given that in this hybrid two component system of $[TBA_xH_{1-x}]^+[Ca_2Nb_3O_{10}]^-$ nanosheets the electronic structure of the $[Ca_2Nb_3O_{10}]^-$ is similar to that of $KCa_2Nb_3O_{10}$, the difference in plasmon behavior can be affiliated to the ligand layers $[TBA_xH_{1-x}]^+$. A rationale supporting this argument is the fact that organic species, for instance phenolic resins show a similar broad plasmon in the energy range 21-24 eV [30].

## 5.7 Core-loss EELS of nanosheets

Core-loss EELS measurements were performed on a single sheet in STEM mode to get a qualitative idea about the composition of the nanosheets. An acquisition time of 10 s was used for acquiring the EEL spectrum. The acquired VEEL spectrum is shown in Figure 5.11. A comparison with literature allows for identification of the edges at the following energies: 240 eV Nb-$M_{4,5}$ edge [29]; 284 eV C-K edge [28,30]; 346 eV Ca-$L_{2,3}$ edge [31]; 363 eV Nb-$M_{2,3}$ edge [29]; 532 eV O-K edge [28].
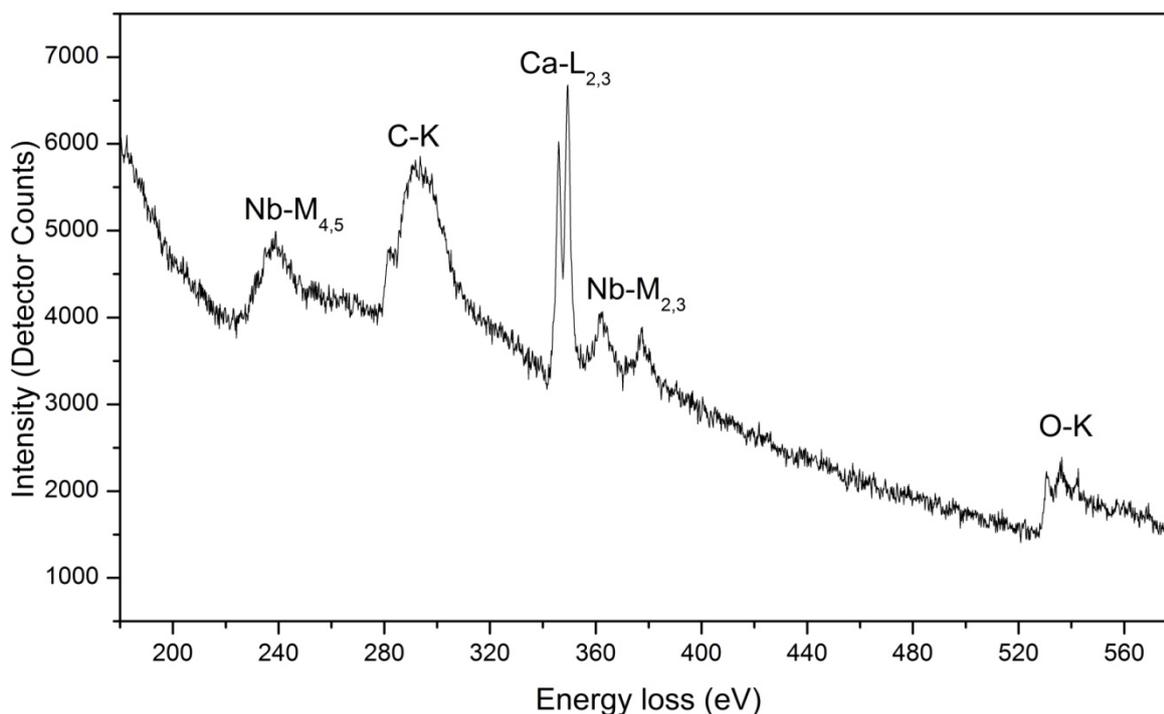
Figure 5.11: The core-loss EEL spectrum of a $[TBA_xH_{1-x}]^+[Ca_2Nb_3O_{10}]^-$ single sheet region.

The core-loss EEL spectrum indicates the presence of Nb, Ca, O and C in the nanosheets which matches with theoretical composition. No perceptible signal is observed due to the K-$L_{2,3}$ edge predicating the removal of K during the exfoliation process. $[TBA]^+$ has a chemical composition of $[C_{16}H_{36}N]^+$ implying a very low atomic percentage of N in the overall nanosheets. This can be related to the fact that no perceptible signal of N is seen around 401 eV for N-K edge [28].

## 5.8 Comparison with literature

Schaak and Mallouk synthesized $[TBA_xH_{1-x}]^+[Ca_2Nb_3O_{10}]^-$ nanosheets and determined the $[TBA]^+$ concentration to be ~ 0.15-0.2 [6]. Li and co-workers [32] measured the height of a single calcium niobate perovskite nanosheet to be 1.85 nm performing AFM measurements under vacuum. Okamoto and co-workers [33] synthesized Rh-doped calcium niobate perovskite nanosheets and measured using AFM the height of 3% Rh-doped calcium niobate nanosheets (3% of calcium atoms being replaced with Rh atoms) to be 2.8-3.0 nm. They attributed the high thickness of the nanosheets to absorption of water and amine [33]. The height of the individual sheet (3.4 nm) measured is greater than that by other groups. In light

of the above mentioned works [6,32,33] it can be assumed that the high thickness of the nanosheets measured using AFM is due to higher $[TBA]^+$ content, absorption of water, and the experimental conditions (AFM measurements being carried out under ambient pressures).

HR-TEM investigations indicate the $[TBA_xH_{1-x}]^+[Ca_2Nb_3O_{10}]^-$ nanosheets to be highly crystalline. This is similar to the observance of high crystallinity in monoloyers of BN, $MoS_2$, $WS_2$ by Coleman and co-workers [3]. The difference between the two material families being that BN, $MoS_2$ and $WS_2$ have charge neutral monolayers after exfoliation while $[TBA_xH_{1-x}]^+[Ca_2Nb_3O_{10}]^-$ nanosheets have cationic and anionic parts.

VEELS measurements indicate that within the range of experimental error, the band gap of $KCa_2Nb_3O_{10}$ does not significantly change as it is exfoliated to $[TBA_xH_{1-x}]^+[Ca_2Nb_3O_{10}]^-$ nanosheets. This is in congruence with the measurements of Arenal and co-workers [34] who with the help of VEELS demonstrated that the band gap of BN nantubes was independent of the nanotube diameter and invariant from that of *h*-BN phase. Both these measurements (this study and that of Arenal *et al.* [34]) do not conform to the quantum confinement effect which is known to work for systems like hematite and silicon [35,36] thereby showing the lack of universal applicability of the quantum confinement effect.

A few authors have attempted to measure the band gap of $[TBA_xH_{1-x}]^+[Ca_2Nb_3O_{10}]^-$ nanosheets. Compton and co-workers [37] dried the nanosheet suspension and performed diffuse reflectance measurements determining the band gap of nanosheets to be 3.53 eV with the help of photocatalysis measurements. Akatsuka and co-workers [38] measured the band gap of calcium niobate nanosheets deposited on ITO substrates to be 3.44 eV doing photocurrent measurements.

It was found that on drying $[TBA_xH_{1-x}]^+[Ca_2Nb_3O_{10}]^-$ sheets, they accumulated into huge micron sized chunks as indicated by the scanning electron microscopy (SEM) image (Figure 5.12), thereby implying that the measurements of Compton and co-workers [37] relate to the electronic structure of those chunks and not that of individual free standing nanowires. A possible explanation for the divergence of the band gap values measured using VEELS and those reported in literature [37,38] could be the fact that only a few electronic levels exist close to the conduction band onset, as is suggested by the DFT calculations on $KCa_2Nb_3O_{10}$, thereby making unerring band gap measurements for these nanostructures taxing.
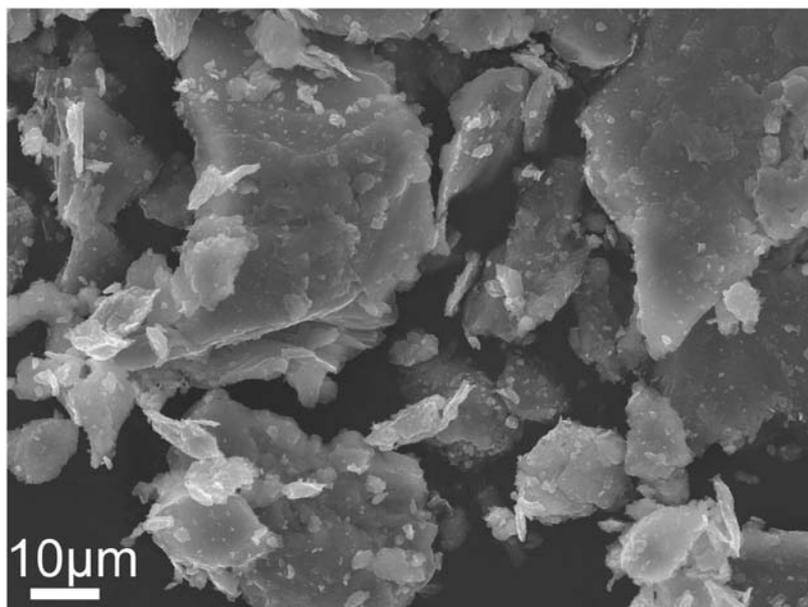
Figure 5.12: Scanning electron microscope image in secondary electron mode of dried nanosheets.

## 5.9 Summary

In summation, it has been demonstrated that HAADF-STEM could be used for characterizing stacks of multiple sheets in a fashion similar to AFM however its applicability in determining the absolute thickness is rather limited. Nanosheets of $[TBA_xH_{1-x}]^+[Ca_2Nb_3O_{10}]^-$ are highly crystalline and when left to dry stack one above the other without any specific planar orientation. VEELS can be used to determine the band gaps of hybrid nanosheets however acquisition and analysis is arduous, requiring a two-fold approach for VEELS acquisition. The band gap of individual free standing $[TBA_xH_{1-x}]^+[Ca_2Nb_3O_{10}]^-$ hybrid nanosheets is found to be $2.9\pm0.2$ eV which is within the experimental error to be considered invariant from that of bulk $KCa_2Nb_3O_{10}$. The VEEL spectrum of these nanosheets is dominated by the single electron transitions which are similar to those observed for bulk $KCa_2Nb_3O_{10}$. Core-loss EELS substantiates the removal of K atoms during the exfoliation process.

## 5.10 Chapter References

[1]     K. S. Novoselov, A. K. Geim, S. V. Morozov, D. Jiang, Y. Zhang, S. V. Dubonos, I. V. Grigorieva, and A. A. Frisov. Electric field effect in atomically thin carbon films. *Science* 306, 666 (2004)

[2]     R. Ma and T. Sasaki, Nanosheets of oxides and hydroxides: Ultimate 2D charge-bearing functional crystallites. *Adv. Mater.* 22, 5082 (2010)

[3]     J. N. Coleman, M. Lotaya, A. O'Neill, S. D. Bergin, P. J. King, U. Khan, K. Young, A. Gaucher, S. De, R. J. Smith, I. V. Shvets, S. K. Arora, G. Stanton, H-Y. Kim, K. Lee, G. T. Kim, G. S. Duesberg, T. Hallam, J. J. Boland, J. J. Wang, J. F. Donegan, J. C. Grunlan, G. Moriarty, A. Shmeliob, R. J. Nicholls, J. M. Perkins, E. M. Grieveson, K. Theuwissen, D. W. McComb, P. D. Nellhist, and V. Nicolosi. Two-dimensional nanosheets produced by liquid exfoliation of layered materials. *Science* 331, 568 (2011)

[4]     K. S. Novoselov, D. Jiang, F. Schedin, T. J. Booth, V. V. Khotkevich, S. V. Morozov, and A. Geim. Two-dimensional atomic crystals. *PNAS* 102, 10451 (2005)

[5]     R. J. Smith, P. J. King, M. Lotaya, C. Wirtz, U. Khan, S. De, A. O'Neill, G. S. Duesberg, J. C. Grunlan, G. Moriaty, J. Chen, J. Wang, A. I. Minett, V. Nicolosi, and J. N. Coleman. Large-scale exfoliation of inorganic layered compounds in aqueous surfactant solutions. *Adv. Mater.* 23, 3944 (2011)

[6]     R. E. Schaak and Thomas E. Mallouk. Self-assembly of tiled perovskite monolayer and multilayer thin films. *Chem. Mater.* 12, 2513 (2000)

[7]     A. J. Jacobson, J. W. Johnson, and J. T. Lewandowski. Interlayer chemistry between thick transition-metal oxide layers: Synthesis and intercalation reaction of $K[Ca_2Na_{n-3}Nb_nO_{3n+1}](3 \leq n \leq 7)$ *Inorg. Chem.* 24, 3727 (1985)

[8]     M. Osada and T. Sasaki. Two-dimensional dielectric nanosheets: novel nanoelectronics from nanocrystal building blocks. *Adv. Mater.* 24, 210 (2012)

[9]     P. Ganter. Synthesis and characterization of $[Ca_2Nb_3O_{10}]^-$ nanosheets and their assembly with layered double hydroxides. *Bachelor's Thesis, Department of Chemistry, Ludwig-Maximilians University Munich* (2011)

[10]    Y. Ebina, T. Sasaki, and M. Watanabe. Study on exfoliation of layered perovskite-type niobates. *Solid State Ionics* 151, 177 (2002)

[11]    E. M. Sabio, M. Chi, N. D. Browning, and F. E. Osterloh. Charge separation in a niobate nanosheet photocatalyst studied with photochemical labeling. *Langmuir.* 26, 7254 (2010)

[12] D. B. Williams, C. B. Carter. *Transmission electron microscopy, a textbook for materials science.* Springer Science + Business Media LLC (2009)

[13] W. A. Knox. Contamination formed around a very narrow electron beam. *Ultramicroscopy* 1, 175 (1976)

[14] L. Gu, V. Srot, W. Sigle, C. Koch, P. van Aken, F. Scholz, S. B. Thapa, C. Kirchner, M. Jetter, and M. Rühle. Band-gap measurements of direct and indirect semiconductors using monochromated electrons. *Phys. Rev. B.*, 75, 195214 (2007)

[15] R. Erni, and N. D. Browning. Quantification of size-dependent energy gap of individual CdSe quantum dots by valence electron energy-loss spectroscopy. *Ultramicroscopy*, 107, 267 (2007)

[16] R. Erni, S. Lazar, and N. D. Browning. Prospects for analyzing the electronic properties in nanoscale systems by VEELS. *Ultramicroscopy* 108, 270 (2008)

[17] O. L. Krivanek, M. M. Disko, J. Tafto, and J. C. H. Spence. Electron energy loss spectroscopy as a probe of the local atomic environment. *Ultramicroscopy* 9, 249 (1982)

[18] R. F. Egerton. New techniques in electron energy-loss spectroscopy and energy-filtered imaging. *Micron*. 34, 127 (2003)

[19] M. Stöger-Pollach. Optical properties and bandgaps from low loss EELS: Pitfalls and solutions. *Micron* 39, 1092 (2008)

[20] T. Malis, S. C. Cheng, and R. F. Egerton. EELS log-ratio technique for specimen-thickness measurement in the TEM. *J. Elec. Microsc. Tech.* 8, 193 (1988)

[21] F. J. Garcia de Abajo. Optical excitations in electron microscopy. *Rev. Mod. Phys.* 82, 209 (2010)

[22] R. F. Egerton. *Electron Energy-Loss Spectroscopy in the Electron Microscope.* Springer Science + Business Media Inc. (2011)

[23] J. Nelayah, M. Kociak, O. Stephan, F. J. Garcia de Abajo, M. Tence, L. Henrard, D. Taverna, I. Pastoriza-Santos, L. M. Liz-Marzan, and C. Colliex. Mapping single plasmons on a single metallic nanoparticle. *Nat. Phys.* 3, 348 (2007)

[24] M. R. S. Huang, R. Erni, H. Lin, R. Wang, C. Liu. Characterization of wurtzite ZnO using valence electron energy loss spectroscopy. *Phys. Rev. B.* 84, 155203 (2011)

[25] M. G. Walls and A. Howie. Dielectric theory of localized valence electron energy loss spectroscopy. *Ultramicroscopy* 28, 40 (1989)

[26] P. M. Echenique, A. Howie, and R. H. Ritchie. Comment on "Near-field electron energy loss spectroscopy of nanoparticles". *Phys. Rev. Lett.* 83, 658 (1999)

[27] M. A. Itskovksy, H. Cohen, and T. Maniv. Radiative interaction of a focused relativistic electron beam in energy-loss spectroscopy of nanoscopic platelets. *Phys. Rev. Lett.* 78, 045419 (2008)

[28] C. C. Ahn, A. L. Krivanek, R. P. Burgner, M. M. Disko, and P. R. Swann. *EELS Atlas,* HR-EM Facility, Arizona State University, Tempe, Arizona, US (1983)

[29] D. Bach, R. Schneider, D. Gerthsen, J. Verbeeck, and W. Sigle. EELS of niobium and niobium oxide phases- Part I: Plasmon and near edges fine structure. *Microsc. Microanal.* 15, 505 (2009)

[30] Z. Zhang, R. Brydson, Z. Aslam, S. Reddy, A. Brown, A. Westwood, and B. Rand. Investigating the structure of non-graphitising carbon using electron energy loss spectroscopy in the transmission electron microscope. *Carbon* 49, 5049 (2011)

[31] K. A. Mkhoyan, J. Silcox, A. Ellison, D. Ast, and R. Dieckmann. Full recovery of electron damage in glass at ambient temperatures. *Phys. Rev. Lett.* 96, 205506 (2006)

[32] B. Li, M. Osada, T. C. Ozawa, Y. Ebina, K. Akatsuka, R. Ma, H. Funakubo, and T. Sasaki. Engineered interfaces of artificial perovskite superlattices via nanosheet deposition process. *ACS Nano* 4, 6673 (2010)

[33] Y. Okamoto, S. Ida, J. Hyodo, H. Hagiwara, and T. Ishihara. Synthesis and photocatalytic activity of Rhodium-doped calcium niobate nanosheets for hydrogen production from water/methanol system without cocatalyst loading. *JACS.* 133, 18034 (2011)

[34] R. Arenal, O. Stephan, M. Kociak, D. Taverna, A. Loiseau, and C. Colliex. Electron energy loss spectroscopy measurement of the optical gaps on individual boron nitride single-walled and multiwalled nanotubes. *Phys. Rev. Lett.* 95, 127601 (2005)

[35]  V. Lehmann and A. Gösele . Porous silicon formation: A quantum wire effect. *Appl. Phys. Lett.* 58, 856 (1991)

[36]  L. Vayssieres, C. Sathe, S. M. Butorin, D. K. Shuh, J. Nordgren, and J. Guo. One-dimensional quantum confinement effect in $\alpha$-$Fe_2O_3$ ultrafine nanorod arrays. *Adv. Mater.* 17, 2320 (2005)

[37]  O. C. Compton, E. C. Carroll, J. Y. Kim, D. S. Larsen and F. Osterloh. Calcium niobate semiconductor nanosheets as catalysts for photochemical hydrogen evolution from water. *J. Phys. Chem. C* 111, 14589 (2007)

[38]  K. Akatsuka, G. Takanashi, Y. Ebina, M. Haga, and T. Sasaki. Electronic band structure of exfoliated titatium – and/or niobium based oxide nanosheets probed by electrochemical and photoelectrochemical measurements. *J. Phys. Chem. C* 116, 12426 (2012)

# 6    Conclusions and outlook

To summarize, this work has detailed the electronic structure of $KCa_2Nb_3O_{10}$ obtained via DFT calculations. Calculations show that upon geometry optimization of $KCa_2Nb_3O_{10}$ structure, small displacements of Ca atoms (up to 0.3 Å) lead to overall force minimization. The $NbO_6$ octahedra get slightly distorted. Overall, the calculations show that the structure predicted by Tokumitsu *et al.* [1] modifies only slightly upon force minimization.

The electronic structure of $KCa_2Nb_3O_{10}$ shows many interesting features. $KCa_2Nb_3O_{10}$ is a direct band gap semiconductor with a band gap of 3.1 eV. The conduction band has only a few available states close to the band onset between 3.1 and 4.3 eV whereas the number of available states increases in the energy range 4.3 to 6.0 eV. The conduction band is composed primarily of states contributed by Nb atoms whereas the valence band is composed of O contributed states. Partial DOS behavior indicates that the conduction band onset at 3.1 eV is primarily contributed by Nb atoms in the median (200) plane.

VEELS measurements on $KCa_2Nb_3O_{10}$ reveal a band gap value of 3.2 ± 0.1 eV. The loss functions determined experimentally and theoretically match well in the energy range below 20 eV without the use of scissors-shift. At higher energies the semi-core excitations come into picture, which are not properly modeled by the computational methodology used. Better convergence was however reached between the experimental and theoretical results relating to the semi-core excitations when a mathematical scissors shift was applied to the excitations of semi-core electrons to higher energy values.

The band gap value obtained from DFT calculations (3.1 eV) and the VEELS measurements (3.2 ± 0.1 eV) match well with the value reported by Domen *et al.* [2]. This shows the success of both these techniques. This is of importance given that conventional DFT based methods have been known to underestimate band gaps. Moreover the VEELS measurements show that band gap value can be properly determined even for a dielectric material when appropriate experimental conditions are used.

Investigations on $[TBA_xH_{1-x}]^+[Ca_2Nb_3O_{10}]^-$ nanosheets show that it is possible to identify regions of single, double or multiple sheets by comparing the intensities in STEM-HAADF mode. This further allows for easy identification of freely suspended sheet regions studying which helps understand the properties of the nanosheets without any external medium in vacuum. The STEM-HAADF intensity profiles, analogous to AFM profiles, show that the ligand layer gets compressed in the region between two $[Ca_2Nb_3O_{10}]^-$ layers.

HR-TEM measurements show the crystalline nature of $[TBA_xH_{1-x}]^+[Ca_2Nb_3O_{10}]^-$ nanosheets similar to that observed by Ebina and co-workers [3]. The crystallinity however is due to order in the $[Ca_2Nb_3O_{10}]^-$ layers. The order in ligand layers comprising of $TBA^+$ and protons is hard to determine; however the measurements reveal crystalline behavior only due to the $[Ca_2Nb_3O_{10}]^-$ layers thereby implying that the ligand layers possess no observable crystallinity.

The acquisition of VEELS from nanosheets is complex. On one hand the signal from nanosheets is very low due to their small sizes while on the other hand trying to get a higher signal by higher exposure leads to damage. The degradation behavior of the nanosheets under irradiation shows that limited perceivable damage occurs within the first five second. Moreover due to difference in intensities of ZLP and valence loss features about three orders of magnitude necessitates a two-step acquisition process to obtain good SNR.

VEELS measurements from single, double and triple sheet region show an identical conduction band onset of 2.9 eV within an error of measurement $\pm 0.2$ eV governed primarily by the alignment procedure. A comparison with the VEEL spectrum of $KCa_2Nb_3O_{10}$ indicates the similarity between the two sorts of materials especially for valence loss excitations up to 8 eV. The measurements suggest that the band gap of $[TBA_xH_{1-x}]^+[Ca_2Nb_3O_{10}]^-$ nanosheets to be equal to that of $KCa_2Nb_3O_{10}$ within the range of experimental error. The band gap value measured in this work is lesser than the band gap value measured by Compton *et al.* [4] and Akatsuka *et al.* [5]. A possible reason for divergence could be low availability of states in the conduction band close to the onset, as has been suggested by the DFT calculations on $KCa_2Nb_3O_{10}$ performed in this work. In addition comparison of core-loss EELS from nanosheets and bulk $KCa_2Nb_3O_{10}$ suggests that exfoliation leads to replacement of K atoms with organic ligands.

In process of explaining the electronic structure of this dielectric material family, a number of new interesting questions have emerged. First of all, it would be interesting to perform

theoretical calculations on $[TBA_xH_{1-x}]^+[Ca_2Nb_3O_{10}]^-$ nanosheets using the TB-mBJ potentials. This TB-mBJ methodology has proven to be successful for crystals; however its adequacy for nanostructures, which invariably contain surfaces, has not yet been tested and form an interesting problem for further research.

Rafferty and Brown [6] had suggested that in a VEEL spectrum the onset of conduction band should obey $I \sim (E-E_g)^{0.5}$ for direct band gap semiconductor and $I \sim (E-E_g)^{1.5}$ for indirect band gap semiconductor. This behavior was experimentally confirmed by Lazar *et al.* for cubic-GaN [7]. However subsequently, Park *et al.* determined [8] the band gap of $SiO_2$ using a linear fit to the onset as opposed to the prediction of Rafferty and Brown [6]. This work indicates that a linear-fit is more correct to obtain the band onset in a VEEL spectrum of $KCa_2Nb_3O_{10}$. This shows that the behavior of onset proposed by Rafferty and Brown [6] do hold, but only under certain conditions. Therefore it is expected that subsequently theoreticians could build upon the model of Rafferty and Brown [6] with a greater applicability.

Generally in an EELS experiment, the plasmon is the most intense feature after the ZLP. The plasmon has been theoretically known to be the position where the real part of the dielectric function is zero and has a positive slope with respect to energy. The calculations on $KCa_2Nb_3O_{10}$ have suggested that this condition is satisfied at three energy values, however the experimental spectrum does not show an intense feature at any of these energies. This divergence shows a lack of succinct understanding of plasmons at present. A probable cause for this is that the free electron model is extensively used for explaining the plasmon behavior. Free electron model could, in principle, be reasonably applicable to valence and conduction band electrons which are sufficiently delocalized, however it definitely would not give a reasonable picture of semi-core electrons which account for two of the three plasmon excitations theoretically suggested. It is hoped that this work shall bring the limit of present knowledge concerning plasmon excitations to the attention of scientific community and that some theoreticians hopefully shall try to model plasmon excitations in a better manner.

## 6.1 Chapter references

[1]     T. Tokumitsu, K. Toda, T. Aoyagi, D. Sakuraba, K. Uematsu, and M. Sato. Powder neutron diffraction study of layered perovskite $KCa_2Nb_3O_{10}$. *J. Cer. Soc. Jap.*114, 795 (2006)

[2] K. Domen, J. Yoshimura, T. Sekine, A. Tanaka, and T. Onishi. A novel series of photocatalysts with ion-exchangeable layered structure of niobates. *Catalysis Lett.* 4, 339 (1990)

[3] Y. Ebina, T. Sasaki, and M. Watanabe. Study on exfoliation of layered perovskite-type niobates. *Solid State Ionics* 151, 177 (2002)

[4] O. C. Compton, E. C. Carroll, J. Y. Kim, D. S. Larsen and F. Osterloh. Calcium niobate semiconductor nanosheets as catalysts for photochemical hydrogen evolution from water. *J. Phys. Chem. C* 111, 14589 (2007)

[5] K. Akatsuka, G. Takanashi, Y. Ebina, M. Haga, and T. Sasaki. Electronic band structure of exfoliated titatium – and/or niobium based oxide nanosheets probed by electrochemical and photoelectrochemical measurements. *J. Phys. Chem. C* 116, 12426 (2012)

[6] B. Rafferty and L. M. Brown. Direct and indirect transitions in the region of the band gap using electron-energy loss spectroscopy. *Phys. Rev. B.* 58, 10326 (1998)

[7] S. Lazar, G. A. Botton, M.-Y. Wu, F. D. Tichelaar, and H. W. Zandbergen. Materials science applications of HREELS in near edge structure analysis and low-energy loss spectroscopy. *Ultramicroscopy* 96, 535 (2003)

[8] J. Park, S. Heo, J. Chung, H. Kim, H. Lee, K. Kim, and G. Park. Bandgap measurements on thin dielectric films using monochromated STEM-EELS. *Ultramicroscopy* 109, 1183 (2009)

# List of publications

## Articles published

1. A. Vetter, K. S. Virdi, S. Espenlaub,W. Rodl, E. Wagner, P. S. Holm, F. Kreppel, C. Scheu, C. Spitzweg, M. Ogris. Chemical Modification of the Adenovirus Capsid for Enhanced Viral Uptake into Target Cells. *Human Gene Therapy* 21, 1193 (2010)
2. S. C. Junggeburth, K. Schwinghammer, K. S. Virdi, C. Scheu, B. V. Lotsch. Towards Mesostructured Zinc Imidazolate Frameworks. *Chemistry: A European Journal* 18, 2143 (2012)
3. A. Abdellah, K. S. Virdi, R. Meier, M. Döblinger, P. Müller-Buschbaum, C. Scheu, P. Lugli, G. Scarpa. Successive Spray Deposition of P3HT/PCBM Organic Photoactive Layers: Material Composition and Device Characteristics. *Adv. Func. Mat.* 22, 4078 (2012)

## Articles under review

1. K. S. Virdi, Y. Kauffmann, C. Ziegler, P. Ganter, B. V. Lotsch, W. D. Kaplan, P. Blaha and C. Scheu. Electronic structure of $KCa_2Nb_3O_{10}$ as envisaged by density functional theory and valence electron energy loss spectroscopy. Under review at the *Phys. Rev. B.*
2. A. Vetter, K. S. Virdi, S. Espenlaub, W. Rödl, E. Wagner, P. S. Holm, C. Scheu, F. Kreppel, C. Spitzweg, and M. Ogris. Adenoviral vectors coated with PAMAM dendrimer conjugates allow CAR independent virus uptake and targeting to the EGF Receptor. Under review at the *Mol. Pharmaceutics*.

## Articles under preparation

1. K. S. Virdi, Y. Kauffmann, C. Ziegler, P. Ganter, P. Blaha, B. V. Lotsch, W. D. Kaplan, and C. Scheu. Extracting band gaps from hybrid two-dimensional nanostructures in the nanometer domain.

2. E. McDermott, E. Wirnhier, W. Schnick, K. S. Virdi, C. Scheu, Y. Kauffmann, W. D. Kaplan, E. Z. Kurmaev, and A. Moewes. Band gap tuning in poly (triaine imide) non-metallic photocatalyst.

3. K. S. Virdi, Y. Kauffmann, A. Abdellah, M. Reymann, P. Lugli, W. D. Kaplan, G. Scarpa and C. Scheu. TEM and EELS based insights into the annealing effects on organic semiconductors PCBM and P3HT.

# List of conferences and meetings attended

1. 17$^{th}$ WIEN2k workshop and International Conference on Advanced Materials Modelling. July 5-10, 2010, Nantes, France

2. Annual Summer School of the International Doctoral Program NanoBioTechnology, Elite Network of Bavaria. July 24-27, 2010, Aiterbach am Chiemsee, Germany.
   Oral presentation given.

3. 62$^{nd}$ Annual Meeting of the Scandinavian Microscopy Society. June 8-10, 2011, Oulu, Finland.
   Oral presentation given.

4. Annual Summer School of the International Doctoral Program NanoBioTechnology, Elite Network of Bavaria, August 2-4, 2011, Aiterbach am Chiemsee, Germany.
   Oral presentation given.

5. High Temperature Capillarity Conference. March 18-22, 2012, Eilat, Israel.
   Poster presentation given.

6. European Materials Research Society Spring Meeting 2012. May 14-18, 2012, Strasbourg, France.
   Oral presentation given.